Surface Water and Ocean Topography Project

Algorithm Theoretical Basis Document
Long Name: Level 2 KaRIn Low Rate Sea Surface Height Science Algorithm
Short Name: L2_LR_SSH

Initial Release

Prepared by:

Electronic signature on file	07/25/2023	Email approval on file	08-01-2023
Bryan Stiles JPL Algorithm Engineer	Date	Pierre Dubois CNES Algorithm Engineer	Date

Approved by:

Electronic signature on file	07/31/2023	Email approval on file	08-01-2023
Curtis Chen JPL Algorithm System Engineer	Date	Alejandro Bohe CNES Algorithm System Engineer	Date

Concurred by:

Email approval on file	07/26/2023	Email approval on file	08-01-2023
Lee Fu JPL Project Scientist	Date	Rosemary Morrow CNES Oceans Science Lead	Date

Paper copies of this document may not be current and should not be relied on for official purposes. The current version is in the JPL Product Data Management System (EPDM: https://epdm.jpl.nasa.gov) and the CNES Product Data Management System

July 24, 2023
JPL D-105502

National Aeronautics and Space Administration
Jet Propulsion Laboratory
California Institute of Technology

Contributing Authors

Name	Affiliation
Bryan Stiles	Jet Propulsion Laboratory
Pierre Dubois	Collecte Localisation Satellites

Science Team Reviewers

Name	Affiliation
G. Dibarboure	Centre National d'Etudes Spatiales
J. T. Farrar	Woods Hole Oceanographic Institution
N. Ayoub	Laboratoire d'Etudes en Geophysique et Oceanographie Spatiales
E. Cosme	Institut des Geosciences de l'Environnement
S. Gille	Scripps Institution of Oceanography, U. C. San Diego
E. Zaron	Oregon State University

Electronic Signature in EPDM

User-Group/Role	...	Decision	Comments	Date
Chen, Curtis W (curtis)-JPL Consumer/Project Consumer	...	Approve		31-Jul-2023 08:19
Stiles, Bryan W (bstiles)-JPL Consumer/Project Consumer	...	Approve		25-Jul-2023 13:12

Change Log

VERSION	DATE	SECTIONS CHANGED	REASON FOR CHANGE
Initial Release	2023-07-24	ALL	Initial Release Approved for public release (URS317369/CL#23-329)

Table of Contents

1 Introduction 10
1.1 Purpose 10
1.2 Scope 10
1.3 Document Organization 10
1.4 Document Conventions 11
2 Overview 13
2.1 Background and Context 13
2.2 Functional Flow 13
3 Algorithm Descriptions 16
3.1 MakeFixedGrid 16
3.1.1 Purpose 16
3.1.2 Input Data 16
3.1.3 Output Data 16
3.1.4 Mathematical Statement 16
3.1.5 Accuracy 18
3.2 ApplyPhaseScreen 18
3.2.1 Purpose 18
3.2.2 Input Data 18
3.2.3 Output Data 18
3.2.4 Mathematical Statement 19
3.2.5 Accuracy 19
3.3 PhaseToHeights 19
3.3.1 Purpose 19
3.3.2 Input Data 19
3.3.3 Output Data 20
3.3.4 Mathematical Statement 20
3.3.5 Accuracy 24
3.4 InterpolateToCentralBeamGrid 24
3.4.1 Purpose 24
3.4.2 Input Data 24
3.4.3 Output Data 25
3.4.4 Mathematical Statement 25
3.4.4.1 Interpolate means 26
3.4.4.2 Interpolate standard deviations 26
3.4.5 Accuracy 27
3.5 CombineBeams 27
3.5.1 Purpose 27
3.5.2 Input Data 28
3.5.3 Output Data 28
3.5.4 Mathematical Statement 29
3.5.5 Accuracy 30
3.6 InterpolateToFixedGrid 45
3.6.1 Purpose 45
3.6.2 Input Data 45

3.6.3 Output Data 46
3.6.4 Mathematical Statement 46
3.6.4.1 Interpolate center beam times 46
3.6.4.2 Interpolate means 46
3.6.4.3 Interpolate standard deviations 47
3.6.5 Accuracy 47
3.7 Generate250-mQualityFlag 47
3.7.1 Purpose 47
3.7.2 Input Data 47
3.7.3 Output Data 48
3.7.4 Mathematical Statement 48
3.8 AverageDownTo2km 48
3.8.1 Purpose 48
3.8.2 Input Data 48
3.8.3 Output Data 49
3.8.4 Mathematical Statement 49
3.8.4.1 Average down time 49
3.8.4.2 Average down 50
3.8.5 Accuracy 52
3.9 ComputeSignificantWaveHeights 55
3.9.1 Purpose 55
3.9.2 Input Data 55
3.9.3 Output Data 55
3.9.4 Mathematical Statement 55
3.9.5 Accuracy 57
3.9.5.1 Algorithm versus geophysical truth 57
3.9.5.2 Algorithm accuracy 58
3.10 ComputeWindSpeed 59
3.10.1 Purpose 59
3.10.2 Input Data 59
3.10.3 Output Data 59
3.10.4 Mathematical Statement 59
3.10.5 Accuracy 60
3.10.5.1 Algorithm versus geophysical truth 60
3.10.5.2 Algorithm accuracy 63
3.11 ComputeSeaStateBiasCorrection 63
3.11.1 Purpose 63
3.11.2 Input Data 63
3.11.3 Output Data 63
3.11.4 Mathematical Statement 64
3.11.5 Accuracy 64
3.11.5.1 Algorithm versus geophysical truth 64
3.11.5.2 Algorithm accuracy 65
3.12 ComputeGeophysicalCorrections 65
3.12.1 Purpose 65
3.12.2 Input Data 66
3.12.3 Output Data 66
3.12.4 Mathematical Statement 67
3.12.5 Accuracy 67

3.13 ComputeSeaSurfaceHeightAnomaly....67
3.13.1 Purpose....67
3.13.2 Input Data....67
3.13.3 Output Data....67
3.13.4 Mathematical Statement....68
3.13.5 Accuracy....68
3.14 ComputeAndApplyRadiometerCorrections....68
3.14.1 Purpose....68
3.14.2 Input Data....68
3.14.3 Output Data....69
3.14.4 Mathematical Statement....69
3.14.5 Accuracy....69
3.15 ComputeCrossCalibrationCorrection....70
3.15.1 Purpose....70
3.15.2 Input Data....70
3.15.3 Output Data....70
3.15.4 Mathematical Statement....70
3.15.5 Accuracy....70
4 References....71
Appendix A. **Acronyms....73**
Appendix B. **Grids....74**
B.1. Grid Types....74
B.2. Interpolation Grids....75
Appendix C. **Interpolations....78**
C.1. linear interpolation....78
C.1.1. Parametrization....78
C.1.2. Interpolate at i, j....78
C.2. Sinc_lineD interpolation....78
C.2.1. Parametrization....79
C.2.2. Construct tables....79
C.2.3. Interpolate at i, j....80
Appendix D. **SWH estimates standard deviation....82**
Appendix E. **Wind Estimates input model....83**
Appendix F. **SSB Correction table....87**

Table of Figures

FIGURE 1: THE KARIN METERING STRUCTURE FRAME (KMSF). VTAN IS THE TANGENTIAL VELOCITY OF THE SATELLITE, THAT IS TO SAY ITS VELOCITY IN THE PLANE PERPENDICULAR TO THE NADIR VECTOR Z. 11
FIGURE 2: INTERFACE DIAGRAM. THE FUNCTIONS (BLACK-EDGED BOXES) HIGH LEVEL DESCRIPTION CAN BE FOUND IN TABLE 1. THE DATA PRODUCT (GREEN-EDGED CYLINDERS) DESCRIPTION CAN BE FOUND IN [1]. FOR THE SAKE OF CLARITY, THE COMPLETE SSB CORRECTION ESTIMATION, WHICH APPLIES TO THE UNSMOOTHED AND THE 2KM SSHS, IS DEPORTED TO THE GREY BOX AND QUOTED TWICE IN THE MAIN FLOW. 14
FIGURE 3: THE TARGET LOCATION IN AN INSAR IMAGE IS DEFINED BY THE INTERSECTION OF THE ISO RANGE SPHERE, ISO DOPPLER CONE, AND ISO PHASE CONE (FROM [6]) 21
FIGURE 4: COMPARISON BETWEEN SIMULATED AND EXPECTED PERFECT ALGORITHM SSH ERROR FOR CENTER OF NINE BEAMS FOR A 2000 KM SIMULATION WITHOUT THERMAL NOISE OR WAVES. THE X-AXIS IS DISTANCE ALONG THE GROUND FROM THE S/C NADIR TRACK. THE BLUE LINE IS SIMULATED ERROR. THE RED DASHED LINE IS EXPECTED PERFECT ALGORITHM ERROR. 32
FIGURE 5: COMPARISON BETWEEN SIMULATED AND EXPECTED PERFECT ALGORITHM SSH ERROR FOR ALL NINE BEAMS FOR A 2000 KM SIMULATION WITHOUT THERMAL NOISE OR WAVES. SEE FIGURE 4 FOR AXIS LABELS AND UNITS. THE BLUE LINES ARE SIMULATED ERROR. THE RED DASHED LINES ARE EXPECTED PERFECT ALGORITHM ERROR. 33
FIGURE 6: COMPARISON BETWEEN BEAM COMBINED (UNSMOOTHED) SIMULATED AND EXPECTED PERFECT ALGORITHM SSH ERROR FOR A 2000 KM SIMULATION WITHOUT THERMAL NOISE OR WAVES. 34
FIGURE 7: EXAMPLE 2 KM BY 2 KM REGION FROM THE RE_10 WAVE FIELD 37
FIGURE 8: MEAN-SEA-SURFACE-ONLY UNSMOOTHED ERROR SPECTRA (LEFT PANEL: NO THERMAL NOISE, RIGHT PANEL: WITH THERMAL NOISE). 38
FIGURE 9: MEAN-SEA-SURFACE-ONLY UNSMOOTHED ERROR SPECTRA, WITH SPECTRA AVERAGED IN THE FREQUENCY DOMAIN USING AN 8 POINT RUNNING AVERAGE (LEFT PANEL: NO THERMAL NOISE, RIGHT PANEL: WITH THERMAL NOISE). 39
FIGURE 10: UNSMOOTHED ERROR SPECTRA FROM THE 200 KM LONG SIMULATIONS WITH 2 M SWH (LEFT PANEL: NO THERMAL NOISE, RIGHT PANEL: WITH THERMAL NOISE). 40
FIGURE 11: UNSMOOTHED ERROR SPECTRA FROM THE 2000 KM LONG RE_11 SIMULATION WITH 2 M SWH (LEFT PANEL: NO THERMAL NOISE, RIGHT PANEL: WITH THERMAL NOISE). 40
FIGURE 12: UNSMOOTHED ERROR SPECTRA FROM THE 200 KM LONG RE_02 SIMULATION WITH 4 M SWH (LEFT PANEL: NO THERMAL NOISE, RIGHT PANEL: WITH THERMAL NOISE). 41
FIGURE 13: UNSMOOTHED ERROR SPECTRA FROM THE 200 KM LONG RE_02 SIMULATION WITH 6 M SWH (LEFT PANEL: NO THERMAL NOISE, RIGHT PANEL: WITH THERMAL NOISE). 41
FIGURE 14: UNSMOOTHED SSH BIAS VS. CROSS TRACK FROM THE 200 KM LONG CASES WITH 2 M SWH, AVERAGED OVER ALONG TRACK, WITH AN 8-POINT (2 KM) RUNNING AVERAGE IN CROSS TRACK (LEFT PANEL: NO THERMAL NOISE, RIGHT PANEL: WITH THERMAL NOISE). 42
FIGURE 15: UNSMOOTHED SSH BIAS VS. CROSS TRACK FROM THE 2000 KM LONG RE_11 CASE WITH 2 M SWH, AVERAGED OVER ALONG TRACK, WITH AN 8-POINT (2 KM) RUNNING AVERAGE IN CROSS TRACK (LEFT PANEL: NO THERMAL NOISE, RIGHT PANEL: WITH THERMAL NOISE). 42
FIGURE 16: UNSMOOTHED SSH STANDARD DEVIATION VS. CROSS TRACK FROM THE 200 KM LONG CASES WITH 2 M SWH, WHERE THE STANDARD DEVIATION IS COMPUTED OVER ALONG TRACK, AND AN 8-POINT (2-KM) RUNNING AVERAGE IS APPLIED IN CROSS TRACK (LEFT PANEL: NO THERMAL NOISE, RIGHT PANEL: WITH THERMAL NOISE). 43
FIGURE 17: UNSMOOTHED SIGMA-0 PERCENT BIAS VS. CROSS TRACK FROM THE 200 KM LONG CASES WITH 2 M SWH, AVERAGED OVER THE ALONG-TRACK DIRECTION, WITH AN 8-POINT (2 KM) RUNNING AVERAGE IN CROSS TRACK (LEFT PANEL: NO THERMAL NOISE, RIGHT PANEL: WITH THERMAL NOISE). 44
FIGURE 18: UNSMOOTHED SIGMA-0 PERCENT STANDARD DEVIATION VS. CROSS TRACK FROM THE 200 KM LONG CASES WITH 2 M SWH, WHERE THE STANDARD DEVIATION IS COMPUTED OVER THE ALONG-TRACK DIRECTION, AND AN 8-POINT (2 KM) RUNNING AVERAGE IS APPLIED IN CROSS TRACK (LEFT PANEL: NO THERMAL NOISE, RIGHT PANEL: WITH THERMAL NOISE). 44
FIGURE 19: BASIC ERROR SPECTRA FROM 200 KM LONG SIMULATIONS WITH 2 M SWH (LEFT PANEL: NO THERMAL NOISE, RIGHT PANEL: WITH THERMAL NOISE). 52
FIGURE 20: BASIC ERROR SPECTRA FROM THE 2000 KM LONG RE_11 SIMULATION WITH 2 M SWH (LEFT PANEL: NO THERMAL NOISE, RIGHT PANEL: WITH THERMAL NOISE). 53
FIGURE 21: BASIC SSH STANDARD DEVIATION VS. CROSS TRACK FROM 200-KM LONG CASES WITH 2 M SWH, WHERE THE STANDARD DEVIATION IS COMPUTED OVER THE ALONG-TRACK DIRECTION (LEFT PANEL: NO THERMAL NOISE, RIGHT PANEL: WITH THERMAL

noise). 53
Figure 22: Basic SSH standard deviation vs. cross track from the 2000 km long RE_11 simulation with 2 m SWH, where the standard deviation is computed over the along-track direction (left panel: no thermal noise, right panel: with thermal noise). 54
Figure 23: WindWave sigma-0 percent standard deviation vs. cross track from the 200 km long cases with 2 m SWH, where the standard deviation is computed over the along-track direction (left panel: no thermal noise, right panel: with thermal noise). 54
Figure 24: Probability density function for volumetric correlation (SWH=2m) 56
Figure 25: From [13]. Drake passage. (a) Current from MITgcm. (b) SWHfrom WW3 using current. (c) SWH from WW3: no current. 58
Figure 26: From [13]. The black and red solid lines (cm2/(cycles/km)) and the dashed blue line (cm2/ s2/(cycles/km)) are respectively the spectra of Figure 25-(c), Figure 25-(b) and Figure 25-(a). The SWH spectrum with currents follows the current spectrum (in k-2.5). Note that at periods $< (g.\ 2\pi.\ [ky \times 10\text{-}3])\text{-}1/2 = 6.$ s, the short waves exceed the long waves 58
Figure 27: Examples of ERS SAR images showing pronounced signatures of features which are not related to wind phenomena: (a) oceanic internal waves, oil spill, and natural surface films at the Strait of Gibraltar, Mediterranean Sea; (b) underwater bottom topography in Chinese coastal waters; (c) natural surface films and oil spills in Chinese coastal waters; (d) rain cells, fronts, and oceanic internal waves in the South China Sea. Swath width is 100 km; scene lengths are 100 km (a,b) and 300 km (c,d). 63
Figure 28: Global mean PSD of the SWH from Jason-2 estimated with MLE3 and MLE4 retrackers (from [18]). The blue lines illustrate the small-scales noise floor: speckle noise, MLE3 retracker estimation noise, and MLE4 retracker estimation noise. On average SWH observability (SNR=1) is limited to scales larger than 40 to 80 km. 65
Figure 29: Plot of simulated height error vs. cross-track position for different correction approaches : this ATBD implements Option 2Δ 70
Figure 30. Illustration of sampling grids 75
Figure 31: Ka and Ku backscatter given by GPM mission with respect to the incidence angle. 83
Figure 32: Ku backscatter. Mean values of binned σ0 *measured by Tropical Rainfall Measuring Mission precipitation Radar as functions of (a) significant wave height* SWH *and (b) wave steepness (Δ) for different incidence angles. The subfigures show the average b over the same (a)* SWH *or (b)* Δ*. Extracted from [R3].* 83
Figure 33: Box plot of σ0 *measured by Tropical Rainfall Measuring Mission precipitation Radar in each 15° azimuthal interval. Widths and gray levels of boxes show the distribution of data. Mean and median are shown as red circles and green squares, respectively. Extracted from [R3].* 84
Figure 34: Ka backscatter measurements given by GPM instrument as a function of significant wave height (from WW3) for incidence angles of 0.75, 3.77 and 6.78°. Graphs provided as a courtesy of Alexis Mouche, from IFREMER. 85
Figure 35: Examples of CMOD functions giving NCRS values in dB. (a) NRCS vs. wind speed in m/s at an incidence angle of 30° and for wind blowing towards the instruments with an angle of 45° with respect to the radial direction. (b) NRCS vs. azimuth wind direction at an incidence angle of 30° and for wind speed of 7 m/s 86
Figure 36: In black: SSB corrections table obtained by the non-parametric solution. In red: the local kernels used for corrections estimation. 87
Figure 37 Jason-3 3D SSB model (SWH, U, Tm) 88

Table of Tables

Table 1. High-level description of the functions used to generate the L2_LR_SSH product. 15
Table 2: Simulated Attitude, Antenna Pointing, Altitude, Lever Arms, and Cross Track deviations 35

List of TBC Items

Page	Section

List of TBD Items

Page	Section
28	3.4.5 Validation of volumetric correlation
44	3.5.5 Validation of 250-m geolocation
57	3.9.5.2 Validation of SWH
62	3.10.5.2 Validation of Wind Speed
64	3.11.5.2 Validation of SSB correction
66	3.12.5 Validation of Geophysical (Tidal) corrections

1 Introduction

1.1 Purpose

The purpose of this Algorithm Theoretical Basis Document (ATBD) is to describe the physical and mathematical basis for the science data processing algorithms that are used to generate the SWOT Level 2 LR SSH (Ka-band Radar Interferometer (KaRIn)) low rate (LR) calibrated sea surface height science data product. These algorithms are applied in the L2_LR_SSH science algorithm software (SAS). The L2_LR_SSH SAS performs Level 2 processing of the L1B interferogram data from the SWOT KaRIn (KaBand Radar Interferometer) system. This document describes the Level 2 processing steps and their corresponding algorithm theoretical basis. The Level 2 processing includes, in order; reconstruction of the heights for each of the beams from L1 processing, resampling of beam parameters of interest (SSH, NRCS, …) on a common grid , combining each of the beams resampled parameters , projection of combined parameters on a fixed grid, averaging and down sampling of the projected parameters to 2km. After the estimation of appropriate proxies (wind, SWH), the SSB is estimated as well as the tidal and the other geophysical corrections from models; these corrections are applied to the SSH to obtain the precal SSH anomaly, that is to say the SSHa before the cross-over calibration application. The processor then adds the cross calibration correction terms to the L2_LR_SSH products.

These algorithms and the associated SAS are used regardless of the latency version of the L2_LR_SSH products; only the inputs change with regard to their availability for the specified latency version.

1.2 Scope

The scope of this document is to:

1. Identify the list of primary functions that compose the processing steps within the SAS_L2_LR_SSH SAS and their flow. These functions are broken down by the primary functional steps involved in the processing.
2. Describe the purpose of each of the functions.
3. Describe the input data to each function.
4. Describe the output data from each function.
5. Describe the mathematical basis of the algorithm in each function.
6. Describe the expected accuracy and/or limitations of the algorithm in each function.
7. Provide the relevant references for the algorithms described in this document.

1.3 Document Organization

Section 1 provides the purpose and scope, of this document.

Section 2 provides the background and context of the algorithms described in this document, and the functional flow of the primary functions (e.g., block diagram).

Section 3 provides the algorithm description for each of the functions shown in the block diagram, including input data, output data, mathematical basis, and expected accuracy.

Section 4 provides references for the algorithms described in this document.

Appendix A provides a listing of the acronyms used in this document.

1.4 Document Conventions

The “latitude” term stands for “geodetic latitude”.

For all vectors $\mathbf{x}$, the norm is $x = |\mathbf{x}|$ and the corresponding unit vector is $\hat{\mathbf{x}} = \mathbf{x}/x$.

A “sample” designates a discrete point measurement; it is located in the image with the pair “line” (index j) and a “pixel” (index i). j is an increasing index in the pulse/long/along-track time and i is an increasing index in the range gates/short/across-track time.

The “plus_y” and “minus_y” quotation in variable names refer to specific configurations in the KaRIn Metering Structure Frame (KMSF).

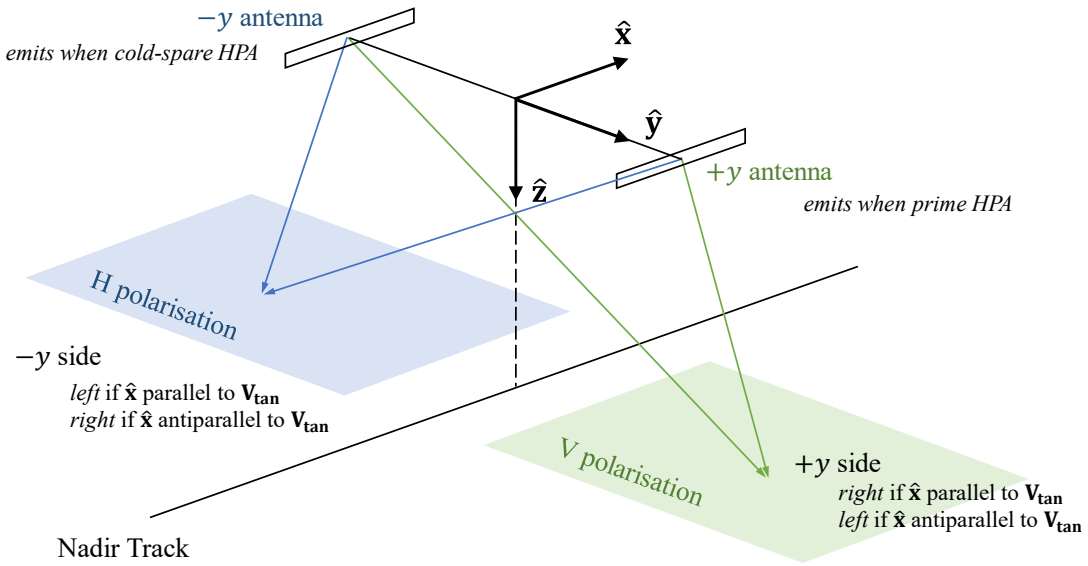

Figure 1: the KaRIn Metering Structure Frame (KMSF). $\mathbf{V}_{tan}$ is the tangential velocity of the satellite, that is to say its velocity in the plane perpendicular to the nadir vector $\hat{\mathbf{z}}$.

As mentioned in [1] and illustrated in Figure 1: “The KaRIn Metering Structure Frame (KMSF) is defined with the origin near the middle of the interferometric baseline, with the two antennas along the +y and –y axes. The +z axis of this frame is controlled to point approximately toward nadir, so the +x axis is approximately parallel or antiparallel to the Earth-relative spacecraft velocity vector. However, the spacecraft periodically performs 180˚ yaw flips (for thermal management reasons, several times per year) such that sometimes the +x axis is in the direction of the velocity vector (i.e., satellite flying forward), and sometimes the –x axis is in the direction of the velocity vector (i.e., satellite flying backward). Which of the +y and –y antennas is to the left or right of the spacecraft along-track direction therefore depends on the yaw state of the spacecraft. As elsewhere in this document, “left” and “right” are defined as if standing on the Earth surface and facing the direction of the spacecraft velocity vector.”. Unrelated to the yaw flip maneuver, the emitting antenna can either be the +y antenna if the prime High Power Amplifier (HPA) is used, or the -y antenna if the cold spare HPA is used.

The 3-dimensional positions variables in the L1B_LR_INTF data product are represented in the international terrestrial reference frame (ITRF). In this Earth-centered, Earth-fixed (ECEF) frame, the $+z$ axis of the ECEF frame goes through the north pole, and the $+x$ axis goes through both the equator (zero latitude) and the prime meridian (zero longitude).

The grids used throughout this document are defined and explained in Appendix B.1.

2 Overview

2.1 Background and Context

The Surface Water and Ocean Topography (SWOT) mission is a partnership between two communities, physical oceanography and hydrology, to share high vertical accuracy topography data produced by the payload, whose principal instrument is the Ka-band Radar Interferometer (KaRIn). The details of SWOT mission objectives and requirements can be found in the SWOT Science Requirements Document [2].

This document describes the Level 2 processing steps that are used to generate the L2_LR_SSH data product from input data, which include the L1B_LR_INTF product, and other auxiliary and ancillary data. The purpose of L2_LR_SSH product is to provide sea surface height, wind speed, significant wave height measurements, and associated tidal and geophysical correction terms along with additional cross calibration correction terms. The L2_LR_SSH products are available everywhere but are most useful over ocean or large lakes. A description of the L2_LR_SSH science data product (L2_LR_SSH Product Data Description) is provided in [1].

2.2 Functional Flow

Figure 2 shows the interface diagram of the L2_LR_SSH processor. Table 1 provides a high-level description of each of the processing functions that are used to generate the L2_LR_SSH product.

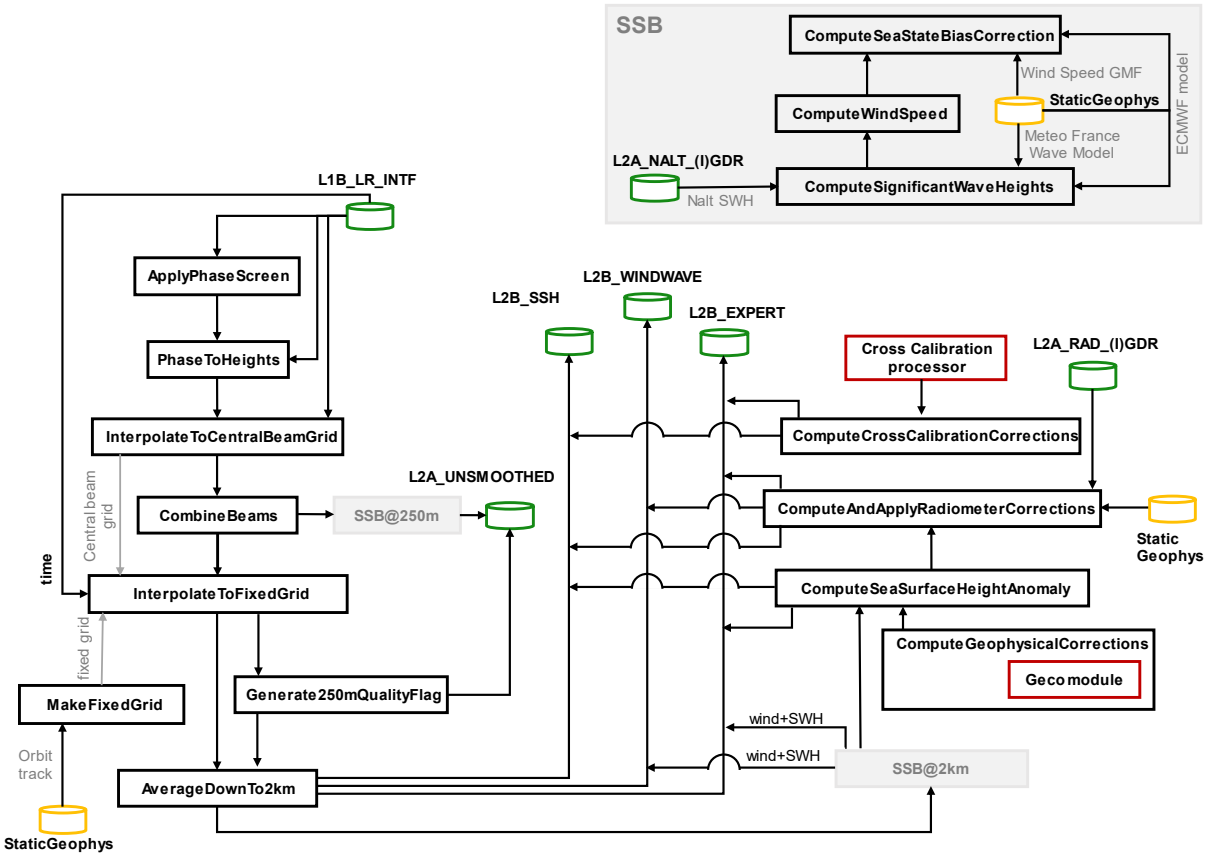

Figure 2: Interface Diagram.
The functions (black-edged boxes) high level description can be found in Table 1.
The data product (green-edged cylinders) description can be found in [1].
For the sake of clarity, the complete SSB correction estimation, which applies to the unsmoothed and the 2km SSHs, is deported to the grey box and quoted twice in the main flow.

Table 1. High-level description of the functions used to generate the L2_LR_SSH product.

Function Name	Description
MakeFixedGrid	Generate the L2B fixed grid from reference orbit track.
ApplyPhaseScreen	Apply the phase screen.
PhaseToHeights	Compute SSH from interferometric phase for all 9 beams
InterpolateToCentralBeamGrid	Interpolate beams to 250-m central reference grid
CombineBeams	Combine beams on central reference grid
InterpolateToFixedGrid	Interpolate data from Native grid to Fixed grid at 250 m posting
Generate250mQualityFlag	Generate quality flag for unsmoothed 250 m data
AverageDownTo2km	Average down fixed-grid quantities to 2 km and decimate to 2km posting. Generate the 2 km quality flags.
ComputeSignificantWaveHeights	Compute significant wave heights (SWH) from volumetric correlation
ComputeWindSpeed	Retrieve wind speeds from sigma0 values, instrument geometry, and ECMWF model wind directions
ComputeSeaStateBiasCorrection	Compute and apply sea state bias correction from wind speed and SWH.
ComputeGeophysicalCorrections	Compute tidal, model media delays attenuations and other geophysical corrections from models.
ComputeSeaSurfaceHeightAnomaly	Apply corrections to SSH and compute SSH anomaly
ComputeAndApplyRadiometerCorrections	Compute additional version of SSH and SSH anomaly where media delays correction from weather model applied during L1B processing are replaced with radiometer media delays
ApplyCrossCalibrationCorrection	Convert XOver info into the proper format and representation.

3 Algorithm Descriptions

3.1 MakeFixedGrid

3.1.1 Purpose

At a given pass, generates the L2B fixed grid from reference orbit track longitudes and latitudes.

3.1.2 Input Data

Description	Source
Reference orbit track for the first ascending and descending passes (resp. pass1 & pass2), at 125m posting: longitude, latitude and heading (orbit track angle with respect to north) $(\mathrm{lon}_{\mathrm{ref}}, \mathrm{lat}_{\mathrm{ref}}, \mathrm{head}_{\mathrm{ref}})$	RefOrbitTrack [3]
Pass number	

3.1.3 Output Data

Description
Longitudes and latitudes (for the WGS84 ellipsoid) of the 250m fixed grid for a given pass.
Index of the nadir point that is closest to the equator.

3.1.4 Mathematical Statement

The fixed reference orbit track is at 125 m spacing.
We subsample by deleting every second point, starting at the initial index to obtain the 250 m fixed grid.

If the pass number is odd / ascending track

$$\mathrm{orbit}_{\mathrm{number}} = (\mathrm{pass}_{\mathrm{number}} - 1)/2$$
$$(\mathrm{lon}_{\mathrm{nadir}}, \mathrm{lat}_{\mathrm{nadir}}, \mathrm{head}_{\mathrm{nadir}}) = (\mathrm{lon}_{\mathrm{ref}}, \mathrm{lat}_{\mathrm{ref}}, \mathrm{head}_{\mathrm{ref}})(\mathrm{pass1})@250m$$

If the pass number is even/ descending track

$$\mathrm{orbit}_{\mathrm{number}} = \mathrm{floor}((\mathrm{pass}_{\mathrm{number}} - 1)/2)$$
$$(\mathrm{lon}_{\mathrm{nadir}}, \mathrm{lat}_{\mathrm{nadir}}, \mathrm{head}_{\mathrm{nadir}}) = (\mathrm{lon}_{\mathrm{ref}}, \mathrm{lat}_{\mathrm{ref}}, \mathrm{head}_{\mathrm{ref}})(\mathrm{pass2})@250m$$

We shift the first ascending/descending pass longitudes to adapt to the current pass number,

$$\mathrm{lon}_{\mathrm{nadir}} = (\mathrm{orbit\_number} - 1) \times \mathrm{DELTA\_LON\_PER\_ORBIT} + \mathrm{lon}_{\mathrm{nadir}}$$

with DELTA_LON_PER_ORBIT = -25.890410959 deg (section 13.1, [4])

We wrap nadir longitude into $[0, 360)$
We convert $(\mathrm{lon}_{\mathrm{nadir}}, \mathrm{lat}_{\mathrm{nadir}}, 0)$ into ECEF nadir positions, $\mathrm{xyz}_{\mathrm{nadir}}$.
We convert nadir longitude into radians.

For each of the nadir points in track

We create the East-North-Up ($\hat{\mathbf{e}}, \hat{\mathbf{n}}, \hat{\mathbf{u}}$) system unit vectors in ECEF.

$$\hat{\mathbf{e}} = \begin{bmatrix} -\sin(\text{lon}_{\text{nadir}}) \\ +\cos(\text{lon}_{\text{nadir}}) \\ 0 \end{bmatrix}$$

$$\hat{\mathbf{n}} = \begin{bmatrix} -\cos(\text{lon}_{\text{nadir}})\sin(\text{lat}_{\text{nadir}}) \\ -\sin(\text{lon}_{\text{nadir}})\sin(\text{lat}_{\text{nadir}}) \\ +\cos(\text{lat}_{\text{nadir}}) \end{bmatrix}$$

$$\hat{\mathbf{u}} = \begin{bmatrix} +\cos(\text{lon}_{\text{nadir}})\cos(\text{lat}_{\text{nadir}}) \\ +\sin(\text{lon}_{\text{nadir}})\cos(\text{lat}_{\text{nadir}}) \\ +\sin(\text{lat}_{\text{nadir}}) \end{bmatrix}$$

We create $\hat{\mathbf{xt}}$**,** the cross-track unit vector

$$\hat{\mathbf{xt}} = \cos\left(\text{head}_{\text{nadir}} + \frac{\pi}{2}\right) \cdot \hat{\mathbf{n}} + \sin\left(\text{head}_{\text{nadir}} + \frac{\pi}{2}\right) \cdot \hat{\mathbf{e}}$$

We compute the great circle angles, for cross-track distances from -70km to 70km at FIXED_GRID_SPACING, on a sphere of radius GREAT_CIRCLE_RADIUS.

while $(\text{dist} = -70000 + i \times \text{FIXED\_GRID\_SPACING}) < 70000$

$$\alpha[i] = \frac{\text{dist}}{\text{GREAT\_CIRCLE\_RADIUS}}, \qquad i = i + 1$$

with GREAT_CIRCLE_RADIUS = 6378137.0 m, FIXED_GRID_SPACING = 250m

For all the great circle angles, we compute ECEF locations using

$$\text{xyz}_{\text{locs}}[i] = \text{xyz}_{\text{nadir}} + \text{GREAT\_CIRCLE\_RADIUS} \times (\sin(\alpha[i])\,\hat{\mathbf{xt}} + (\cos(\alpha[i]) - 1)\hat{\mathbf{u}})$$

We convert the ECEF locations (xyz_{locs}) to geodetic longitude, latitude, heights (h) using the reference ellipsoid WGS84. The fixed grid locations are finally obtained by using the computed longitude and latitude and setting the heights to zero, $h = 0$.

We compute the middle index of the pass, i.e. the index of the nadir point the closest to the equator.

$$\text{mid\_idx} = \text{argmin}(|\text{lat}_{\text{nadir}}|)$$

3.1.5 Accuracy

The accuracy, reported for the final fixed grid at 2 km spacing (obtain by decimating the 250m spaced fixed grid), is discussed in section 13.1 of [4].

3.2 ApplyPhaseScreen

3.2.1 Purpose

Apply a phase screen that is empirically computed during instrument calibration on orbit. It is impossible in practice to match exactly the far field phase of both antennas. Differences in the phase far-field pattern, which may be caused by interaction with the baseline and spacecraft structures, will result in phase differences between the channels that varies as a function of look angle, or, equivalently, absolute phase. Unlike the other parameters, the phase screen is not a single value, but a continuous function that must be estimated across the entire swath. The phase screen is implemented as a polynominal correction to interferometric phase as a function of absolute phase. Two different phase screens are utilized one each for the V and H polarization half-swaths. The phase screen is meant to correct for static phase (height) errors that vary across the swath. Dynamic phase (height) errors are handled separately by the cross-over calibration processor.

3.2.2 Input Data

Description	Source
$N_B(=9)$ complex, bias-corrected, flattened interferograms at 250m posting, 500m resolution	L1B_LR_INTF::[right/left]::interferogram
Positions of KMSF origin (ECEF frame) at 250m sampling	L1B_LR_INTF::[tvp_right/tvp_left]::(x,y,z)
Velocities of KMSF origin(ECEF frame) at 250m sampling	L1B_LR_INTF::[tvp_right/tvp_left]::(vx,vy,vz)
Right Antenna Positions (ECEF frame) at 250m sampling	L1B_LR_INTF:: [tvp_right/tvp_left]::(plus_y_antenna_x, plus_y_antenna_y, plus_y_antenna_z)
Left Antenna Positions (ECEF frame) at 250m sampling	L1B_LR_INTF:: [tvp_right/tvp_left]::(minus_y_antenna_x, minus_y_antenna_y, minus_y_antenna_z)
Curvature-corrected reference locations (ECEF frame)	L1B_LR_INTF::[right/left]::reference_location
Phase Screen (polynomial coefficients)	StaticKaRinCal::

3.2.3 Output Data

Description
$N_B(=9)$ complex, bias-corrected, flattened interferogram at 250m posting, 500m resolution with phase screen applied

3.2.4 Mathematical Statement

Step 1: Reference phase is computed from the reference location of each pixel and spacecraft (s/c) geometry. Absolute phase is computed as the sum of the interferometric phase and the reference phase. Note that absolute phase can and will have values outside [-π,π] radians.

$$\phi_{ref} = \frac{2\pi}{\lambda}(\mathbf{B} \cdot \hat{\boldsymbol{\ell}})$$

Where λ is the wave length, **B** is the baseline vector between the two antenna phase centers (plus y-axis antenna – minus y-axis antenna), and $\hat{\boldsymbol{\ell}}$ is the unit vector in the look direction.

Step 2: Polynomial phase screen correction as a function of the absolute phase is computed and applied to each pixel in the interferogram.

3.2.5 Accuracy

N/A

3.3 PhaseToHeights

3.3.1 Purpose

Given the differential interferometric phase and the reference location of each 250-m pixel for each of the 9 beams, compute measured 3-D positions of each pixel. The reference locations are the absolute locations obtained as the center of gravity of the Point Target Response (PTR) placed on the reference surface, as performed in the L1B *SimulatePhaseBias* ([5]); a null differential interferometric phase sets the measured pixel on the reference location.

3.3.2 Input Data

Description	Source
$N_B(=9)$ complex, bias-corrected, flattened interferograms at 250m posting, 500m resolution	interferogram with phase screen applied (Section 3.2)
Positions of KMSF origin (ECEF frame) at 250m sampling	L1B_LR_INTF::[tvp_right/tvp_left]::(x,y,z)
Velocities of KMSF origin(ECEF frame) at 250m sampling	L1B_LR_INTF::[tvp_right/tvp_left]::(vx,vy,vz)
Right Antenna Positions (ECEF frame) at 250m sampling	L1B_LR_INTF:: [tvp_right/tvp_left]::(plus_y_antenna_x, plus_y_antenna_y, plus_y_antenna_z)
Left Antenna Positions (ECEF frame) at 250m sampling	L1B_LR_INTF:: [tvp_right/tvp_left]::(minus_y_antenna_x, minus_y_antenna_y, minus_y_antenna_z)
Curvature-corrected reference locations (ECEF frame)	L1B_LR_INTF::[right/left]::reference_location

3.3.3 Output Data

Description
3-D geolocations of each pixel.
Height sensitivity to phase at reference location of each pixel.
Look angles at reference location of each pixel.
Incidence angles at reference location of each pixel.

3.3.4 Mathematical Statement

We introduce the notations

- $\mathbf{S}$ the KMSF origin position, in ECEF frame
- $\mathbf{S}_T$ the transmitting and receiving antenna position (+y for prime HPA, -y for spare HPA), in ECEF frame
- $\mathbf{S}_R$ the receiving-only antenna position (-y for prime HPA, +y for spare HPA), in ECEF frame
- $\mathbf{b} = \mathbf{S}_R - \mathbf{S}_T$ is the baseline vector
- $\mathbf{V}$ the KMSF origin velocity, in ECEF frame
- $\mathbf{p}_{\mathbf{ref}}$ the surface reference location in ECEF frame
- $\mathbf{p}$ the surface measured geolocation in ECEF frame

We define the look vectors:

- $\boldsymbol{\ell}_T = \mathbf{p} - \mathbf{S}_T$, the look vector from the transmitting antenna to the measurement location.
- $\boldsymbol{\ell}_R = \mathbf{p} - \mathbf{S}_R$, the look vector from the receiving-only antenna to the measurement location.
- $\boldsymbol{\ell} = \mathbf{p} - \mathbf{S}$, the look vector from the satellite coordinate origin position to the measurement location.
- $\boldsymbol{\ell}_{ref} = \mathbf{p}_{\mathrm{ref}} - \mathbf{S}$, the look vector from the satellite coordinate origin position to the reference location

The target measured point, in ECEF frame is given by

$$\mathbf{p} = \mathbf{S} + \ell\, \hat{\boldsymbol{\ell}}$$

The full three-dimensional height reconstruction is based on the observation that the target location is the intersection locus of three surfaces [6]:

- the iso slant-range sphere
- the iso Doppler cone
- the iso interferometric phase cone

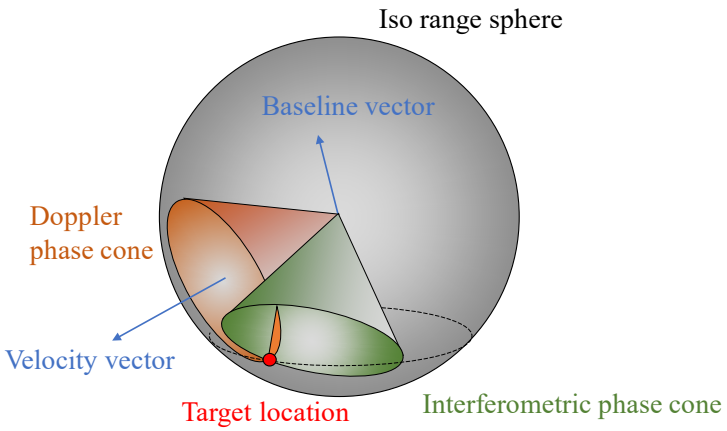

Figure 3: The target location in an InSAR image is defined by the intersection of the iso range sphere, iso doppler cone, and iso phase cone (from [6])

The cone angles are defined relative to the generating axes determined by the velocity vector for the Doppler cone and the baseline vector for the phase cone. The intersection locus is the solution of the system equations.

The Doppler cone is given by

$$f_D = \frac{2}{\lambda}\hat{\boldsymbol{\ell}} \cdot \mathbf{V}$$

The interferometric phase is defined by the phase difference between the image formed on the receiving-only antenna and the image formed on the transmitting antenna.

$$\varphi = \frac{2\pi}{\lambda}(\ell_R - \ell_T)$$

We set the baseline vector $\mathbf{b} = \boldsymbol{\ell}_R - \boldsymbol{\ell}_T$ with

$$\boldsymbol{\ell}_R = \boldsymbol{\ell} + (\mathbf{S} - \mathbf{S}_R) \stackrel{\text{def}}{=} \boldsymbol{\ell} + \mathbf{b}_R$$
$$\boldsymbol{\ell}_T = \boldsymbol{\ell} + (\mathbf{S} - \mathbf{S}_T) \stackrel{\text{def}}{=} \boldsymbol{\ell} + \mathbf{b}_T$$

$$\ell_R - \ell_T = |\boldsymbol{\ell}_R| - |\boldsymbol{\ell}_T| = \ell\left(\left(1 + \frac{b_R^2}{\ell^2} + 2\frac{\boldsymbol{\ell}\cdot\mathbf{b}_R}{\ell^2}\right)^{\mathbf{1/2}} - \left(1 + \frac{b_T^2}{\ell^2} + 2\frac{\boldsymbol{\ell}\cdot\mathbf{b}_T}{\ell^2}\right)^{\mathbf{1/2}}\right)$$

Using a first order expansion with $b_T \ll \ell$, $b_R \ll \ell$ (it is known as the plane wave approximation)

$$\ell_R - \ell_T \simeq \frac{b_R^2 - b_T^2}{2\ell} + \frac{\boldsymbol{\ell}\cdot(\mathbf{b}_R - \mathbf{b}_T)}{\ell}$$

We recall that the baseline vector is $\mathbf{b} = \mathbf{S}_R - \mathbf{S}_T = \boldsymbol{\ell}_R - \boldsymbol{\ell}_T = \mathbf{b}_R - \mathbf{b}_T$

$$|\boldsymbol{\ell}_R| - |\boldsymbol{\ell}_T| \simeq \left(\boldsymbol{\ell} + \frac{(\mathbf{b}_R + \mathbf{b}_T)}{2}\right)\cdot\frac{\mathbf{b}}{\ell}$$
$$\simeq \frac{(\boldsymbol{\ell}_R + \boldsymbol{\ell}_T)}{2}\cdot\frac{\mathbf{b}}{\ell}$$

Using a first order expansion with $\ell \gg |\mathbf{b}_T + \mathbf{b}_R|/2$

$$|\boldsymbol{\ell}_R| - |\boldsymbol{\ell}_T| \simeq \frac{\boldsymbol{\ell} \cdot \mathbf{b}}{\ell}$$

The phase surface cone is then

$$\varphi \simeq \frac{2\pi}{\lambda}\left(\hat{\boldsymbol{\ell}} \cdot \mathbf{b}\right)$$

It is worth noticing that the actual phase surface is a hyperboloid; however, the plane wave approximation causes the hyperboloid to degenerate to a cone.

The accessible information is not the absolute interferometric phase, but the flattened interferometric phase relative to the reference locations established in the *SimulatePhaseBias* and *CorrectPhaseBias* algorithms in [4]. The flattened interferometric phase can be expressed by

$$\phi = \varphi - \frac{2\pi}{\lambda}\left(\hat{\boldsymbol{\ell}}_{ref} \cdot \mathbf{b}\right)$$

We derive an orthogonal basis $\{\hat{\mathbf{V}}, \hat{\boldsymbol{\beta}}, \hat{\mathbf{d}}\}$

- $\hat{\mathbf{V}}$ is the normalized velocity vector
- $\hat{\boldsymbol{\beta}} = \mathbf{b}_\perp / b_\perp$, with $\mathbf{b}_\perp = \mathbf{b} - \left(\mathbf{b} \cdot \hat{\mathbf{V}}\right)\hat{\mathbf{V}}$ the baseline vector part perpendicular to the velocity vector and $b_\perp = |\mathbf{b}_\perp|$
- $\hat{\mathbf{d}} = \hat{\mathbf{V}} \times \hat{\boldsymbol{\beta}}$, the down vector, completes the basis (note $\hat{\mathbf{d}} = \hat{\mathbf{V}} \times \left[\mathbf{b} - \left(\mathbf{b} \cdot \hat{\mathbf{V}}\right)\hat{\mathbf{V}}\right]/b_\perp = \hat{\mathbf{V}} \times \mathbf{b}/b_\perp$ **)**

We write $\hat{\boldsymbol{\ell}}$ in the $\{\hat{\mathbf{V}}, \hat{\boldsymbol{\beta}}, \hat{\mathbf{d}}\}$ orthogonal basis

$$\hat{\boldsymbol{\ell}} = \hat{\ell}_V \hat{\mathbf{V}} + \hat{\ell}_\beta \hat{\boldsymbol{\beta}} + \hat{\ell}_d \hat{\mathbf{d}}$$

The $\hat{\boldsymbol{\ell}}$ vector coordinates are

$$\hat{\ell}_V = \hat{\boldsymbol{\ell}} \cdot \hat{\mathbf{V}} = \frac{\lambda f_D}{2V}$$

$$\hat{\ell}_\beta = \hat{\boldsymbol{\ell}} \cdot \hat{\boldsymbol{\beta}} = \frac{\hat{\boldsymbol{\ell}}}{b_\perp} \cdot \left(\mathbf{b} - \left(\mathbf{b} \cdot \hat{\mathbf{V}}\right)\hat{\mathbf{V}}\right) = \frac{\hat{\boldsymbol{\ell}} \cdot \mathbf{b}}{b_\perp} - \left(\mathbf{b} \cdot \hat{\mathbf{V}}\right)\frac{\hat{\boldsymbol{\ell}} \cdot \hat{\mathbf{V}}}{b_\perp} = \frac{\lambda}{2\pi\, b_\perp}\varphi - \frac{\mathbf{b} \cdot \hat{\mathbf{V}}}{b_\perp}\hat{\ell}_V$$

$$\left|\hat{\ell}_d\right| = \sqrt{1 - \hat{\ell}_V^2 - \hat{\ell}_\beta^2}$$

We constrain the Doppler at measurement locations to be the same as the Doppler at reference locations.

$$f_D = \frac{2}{\lambda}\hat{\boldsymbol{\ell}} \cdot \mathbf{V} = \frac{2}{\lambda}\hat{\boldsymbol{\ell}}_{ref} \cdot \mathbf{V}$$

Finally, the $\hat{\boldsymbol{\ell}}$ vector coordinates are

$$\hat{\ell}_V = \frac{2}{\lambda}\hat{\boldsymbol{\ell}}_{ref} \cdot \mathbf{V}$$

$$\hat{\ell}_\beta = \frac{\lambda}{2\pi\, b_\perp}\left[\phi + \frac{2\pi}{\lambda}\left(\hat{\boldsymbol{\ell}}_{ref} \cdot \mathbf{b}\right)\right]$$

$$\hat{\ell}_d = \sqrt{1 - \hat{\ell}_\beta^2}$$

Obviously, the target is in the down direction, hence the positive value of $\hat{\ell}_d$ in resolving the sign ambiguity of the square root.

Finally, the reconstructed height is given by

$$\mathbf{p} = \mathbf{S} + \ell \left[\hat{\ell}_V \, \hat{\mathbf{V}} + \hat{\ell}_\beta \, \hat{\boldsymbol{\beta}} + \hat{\ell}_d \, \hat{\mathbf{d}}\right]$$

The ECEF position can be equivalently expressed in Cartesian coordinates or in longitude, latitude, and altitude relative to a given reference ellipsoid.

$$\mathbf{p} = (x, y, z) \equiv (lon, lat, h)$$

Height sensitivity to the phase at $\mathbf{p_{ref}}$

We also compute the height sensitivity to phase at $\mathbf{p_{ref}}$, following the same procedure but using a constrained, small, differential interferometric phase value.

$$\phi' = 0.01\text{rad}$$

We obtain

$$\mathbf{p}' = \mathbf{S} + \ell' \cdot \hat{\boldsymbol{\ell}}'$$

After the (longitude, latitude, altitude) conversion

$$\mathbf{p}' = (x', y', z') \equiv (lon', lat', h')$$
$$\mathbf{p_{ref}} = (x_{\text{ref}}, y_{\text{ref}}, y_{\text{ref}}) \equiv (lon_{\text{ref}}, lat_{\text{ref}}, h_{\text{ref}})$$

the height sensitivity to the phase is obtained with

$$\frac{\partial h}{\partial \phi} = \frac{h' - h_{\text{ref}}}{\phi'}$$

A similar calculation is used to compute the sensitivity of the two horizontal components of the location to phase. These quantities are then used to compute the latitude and longitude sensitivities reported in the Unsmoothed (250-m) product file.

Look angle

Given the KSMF origin position we get the sub satellite longitude and latitude

$$\mathbf{S} = (x_0, y_0, z_0) \equiv (lon_0, lat_0, h_0)$$

The nadir position in ECEF is deduced using the subsatellite coordinates

$$\mathbf{S_0} = (lon_0, lat_0, 0) \equiv (x_N, y_N, z_N)$$

The nadir vector is

$$\hat{\mathbf{N}} = \frac{\mathbf{S_0} - \mathbf{S}}{|\mathbf{S_0} - \mathbf{S}|}$$

The look angle uses the $\boldsymbol{\ell}_{ref}$ projection on the nadir vector:

$$\gamma = \text{acos}\left(\hat{\mathbf{N}} \cdot \frac{\boldsymbol{\ell}_{ref}}{\ell_{ref}}\right)$$

Incidence angle
The incidence angle uses the $\boldsymbol{\ell}_{ref}$ projection on the local normal vector:

$$\theta = \text{acos}\left(-\widehat{\mathbf{n}} \cdot \frac{\boldsymbol{\ell}_{ref}}{\ell_{ref}}\right)$$

3.3.5 Accuracy

See Section 3.5.5 for a description of the validation method and metrics for the Unsmoothed (250-m grid) SSH measurements.

3.4 InterpolateToCentralBeamGrid

3.4.1 Purpose

Interpolate beams to 250-m central beam native grid

3.4.2 Input Data

Description	Source
$N_B(=9)$ Curvature corrected reference locations (ECEF frame)	L1B_LR_INTF::[right/left]::reference_location
$N_B(=9)$ 3-D measured geolocations for each sample (ECEF frame)	*PhaseToHeights* (this document, 3.3)
$N_B(=9)$ phase uncertainties ($\text{phase}_{\text{std}}$)	L1B_LR_INTF::[right/left]::phase_uncert
$N_B(=9)$ Height sensitivity (dhdphi)	*PhaseToHeights* (this document, 3.3)
$N_B(=9)$ NRCS	L1B_LR_INTF::[right/left]::sig0
$N_B(=9)$ NRCS uncertainty	L1B_LR_INTF::[right/left]::sig0_uncert
$N_B(=9)$ Volumetric correlation	L1B_LR_INTF::[right/left]::volumetric correlation
$N_B(=9)$ Volumetric correlation uncertainty	L1B_LR_INTF::[right/left]::volumetric correlation_uncert
$N_B(=9)$ Incidence angles	*PhaseToHeights* (this document, 3.3)
$N_B(=9)$ Beam quality flags	L1B_LR_INTF::[right/left]::interferogram_qual

3.4.3 Output Data

Description
Central Beam Native Grid
$N_B(=9)$ measured latitudes
$N_B(=9)$ cosines of measured longitudes
$N_B(=9)$ sines of measured longitudes
$N_B(=9)$ SSH at 250m posting, 500m resolution
$N_B(=9)$ SSH uncertainty at 250m posting, 500m resolution
$N_B(=9)$ NRCS at 250m posting, 500m resolution
$N_B(=9)$ NRCS uncertainty at 250m posting, 500m resolution
$N_B(=9)$ Volumetric correlation at 250m posting, 500m resolution
$N_B(=9)$ Volumetric correlation uncertainty at 250m posting, 500m resolution
$N_B(=9)$ Height Sensitivity at 250m posting, 500m resolution
$N_B(=9)$ incidence angles at 250m posting, 500m resolution
$N_B(=9)$ Beam quality flags at 250m posting, 500m resolution

3.4.4 Mathematical Statement

The interpolation is performed from the source grid to the target grid. Because geolocation values themselves are interpolated here, the resulting interpolated geolocation data will not necessarily be on the target grid. The grid formed by the interpolated geolocations is referred to as the data grid.

The source grid for each beam is defined by the set of reference locations for that beam. The target grid is the source grid of the central beam (#5), the so-called "central beam native grid". Note that the data grid is defined by the beam-combined measured locations, including information from all 9 beams after interpolation to the central-beam (#5) reference grid. (see *BeamCombine* 3.5)

For all cross-track pixels (i) and along-track lines (j), and for all beams (k)

Convert from ECEF coordinates to (longitude, latitude, altitude) coordinates

$$(lon_{\mathrm{ref}}[k], lat_{\mathrm{ref}}[k], alt_{\mathrm{ref}}[k]) \equiv \mathbf{refloc}[i,j,k]$$

Construct the grids

$$\mathrm{grid}_{\mathrm{from}}[i,j,k] = \left(lon_{\mathrm{ref}}[k], lat_{ref}[k]\right)$$
$$\mathrm{grid}_{\mathrm{to}}[i,j] = \left(lon_{\mathrm{ref}}[5], lat_{ref}[5]\right)$$

Interpolate means

We interpolate
- latitude
- sine of longitude
- cosine of longitude[1]
- SSH
- incidence angles
- NRCS
- volumetric correlation
- height sensitivity
- interferogram quality flag

following the common procedure, described below.

Let (X, Y) be a pair of (data to interpolate, interpolated data). X and Y have respective shapes $\left(N_X^{pix}, N_X^{lin}\right)$ and $\left(N_Y^{pix}, N_Y^{lin}\right)$.

The integer coordinates in the Y grid, $\left(\{i_Y \in \left[0, N_Y^{pix} - 1\right]\}, \{j_Y \in \left[0, N_Y^{lin} - 1\right]\}\right)$, have corresponding real coordinates $(\{i\}, \{j\})$ in X given by the functions $\text{pixel}_{\text{from}}, \text{line}_{\text{from}}$ constructed using B.2.

$$i = \text{pixel}_{\text{from}}[i_Y, j_Y]$$
$$j = \text{line}_{\text{from}}[i_Y, j_Y]$$

For the special case of central beam: no interpolation is needed

$$Y[i_Y, j_Y, 5] = X[i_Y, j_Y, 5]$$

In all other cases, perform a 2 dimensional sinc interpolation of X at (i, j). The procedure can be found in C.2.3 (, including the special case for the interpolation of the flags). Sinc interpolation is selected because it corresponds to ideal filtering (equal gain at all frequency components). Here, the length-limited characteristic of the interpolator will produce a little deviation from an ideal flat response at very short wavelengths (close to 500 m), which is negligible in the overall final data quality according to our analyses.

3.4.4.1 Interpolate standard deviations

We interpolate the standard deviations of
- SSH (constructed on the native grid with $\text{SSH}_{\text{std}} = \text{phase}_{\text{std}} \times |\text{dhdphi}|$)
- NRCS
- volumetric correlation

following the same procedure, described below.

[1] Note that the sine and cosine of longitude are interpolated instead of the longitude itself to avoid wrapping problems.

Let (X, Y) be a pair of (data to interpolate, interpolated data). X and Y have respective shapes (N_X^{pix}, N_X^{lin}) and (N_Y^{pix}, N_Y^{lin}).

The integer coordinates in the Y grid, $(\{i_Y \in [0, N_Y^{pix} - 1]\}, \{j_Y \in [0, N_Y^{lin} - 1]\})$, have corresponding real coordinates $(\{i\}, \{j\})$ in X given by the functions $\text{pixel}_{\text{from}}, \text{line}_{\text{from}}$ constructed using B.2.

$$i = \text{pixel}_{\text{from}}[i_Y, j_Y]$$
$$j = \text{line}_{\text{from}}[i_Y, j_Y]$$

For the special case of central beam: no interpolation is needed

$$Y[i_Y, j_Y, 5] = X[i_Y, j_Y, 5]$$

In all other cases, perform a 2 dimensional sinc interpolation of $1/X^2$ at (i, j). [2] Then we compute the square root of the inverse interpolated data to obtain Y.

3.4.5 Accuracy

See Section 3.5.5 for a description of the validation method and metrics for the Unsmoothed (250-m grid) SSH, geolocation, and sigma-0 measurements. Volumetric correlation validation is TBD.

3.5 CombineBeams

3.5.1 Purpose

Interpolate beams to central reference 250-m grid and combine them, for SSH (mean and std), NRCS (mean and std), Volumetric Correlation (mean and std) and Height Sensitivity (mean).

[2] The choice of the procedure is motivated by the use of the inverse of the variances as the weights used in the *CombineBeams* algorithm; in doing so, we interpolate the weights.

3.5.2 Input Data

Description	Source
$N_B(=9)$ measured latitudes	*InterpolateToCentralBeamGrid* (this document, 3.4)
$N_B(=9)$ cosines of measured longitudes	*InterpolateToCentralBeamGrid* (this document, 3.4)
$N_B(=9)$ sines of measured longitudes	*InterpolateToCentralBeamGrid* (this document, 3.4)
$N_B(=9)$ SSH at 250m posting, 500m resolution	*InterpolateToCentralBeamGrid* (this document, 3.4)
$N_B(=9)$ SSH uncertainty at 250m posting, 500m resolution	*InterpolateToCentralBeamGrid* (this document, 3.4)
$N_B(=9)$ NRCS at 250m posting, 500m resolution	*InterpolateToCentralBeamGrid* (this document, 3.4)
$N_B(=9)$ NRCS uncertainty at 250m posting, 500m resolution	*InterpolateToCentralBeamGrid* (this document, 3.4)
$N_B(=9)$ Volumetric correlation at 250m posting, 500m resolution	*InterpolateToCentralBeamGrid* (this document, 3.4)
$N_B(=9)$ Volumetric correlation uncertainty at 250m posting, 500m resolution	*InterpolateToCentralBeamGrid* (this document, 3.4)
$N_B(=9)$ Height Sensitivity at 250m posting, 500m resolution	InterpolateToCentralBeamGrid (this document, 3.4)
$N_B(=9)$ incidence angles at 250m posting, 500m resolution	InterpolateToCentralBeamGrid (this document, 3.4)
$N_B(=9)$ Beam quality flags at 250m posting, 500m resolution	InterpolateToCentralBeamGrid (this document, 3.4)

3.5.3 Output Data

Description	Output data product (if exists)
Latitudes for combined data	
Latitudes uncertainties for combined data	
Longitudes for combined data	
Longitudes uncertainties for combined data	
Combined SSH at 250m posting, 500m resolution	L2A_UNSMOOTHED::[right/left]::ssh_karin_2
Combined SSH uncertainty at 250m posting, 500m resolution	L2A_UNSMOOTHED::[right/left]::ssh_karin_uncert
Combined NRCS at 250m posting, 500m resolution	L2A_UNSMOOTHED::[right/left]::sig0_karin_2
Combined NRCS uncertainty at 250m posting, 500m resolution	L2A_UNSMOOTHED::[right/left]::sig0_karin_uncert
Combined Volumetric correlation at 250m posting, 500m resolution	
Combined Volumetric correlation uncertainty at 250m posting, 500m resolution	
Combined Height Sensitivity at 250m posting, 500m resolution	
Combined Incidence angles at 250m posting, 500m resolution	
Combined beams quality flag at 250m posting, 500m resolution	

3.5.4 Mathematical Statement

We combine the
- latitude
- sine of longitude
- cosine of longitude
- SSH
- incidence angles
- NRCS
- volumetric correlation
- height sensitivity

following the common procedure described below.

Let $\left(\{Y, Y_{std}\}_{N_B}, (Z, Z_{std})\right)$ be a tuple of (data to combine, combined data). The pairs are in

$$\left(\{\mathrm{lat}_{\mathrm{interp}}, \mathrm{SSH}_{\mathrm{std\ interp}}\}_{N_B}, (\mathrm{lat}, \mathrm{SSH}_{\mathrm{std}})\right)$$
$$\left(\{\mathrm{cos\_lon}_{\mathrm{interp}}, \mathrm{SSH}_{\mathrm{std\ interp}}\}_{N_B}, (\mathrm{cos\_lon}, \mathrm{SSH}_{\mathrm{std}})\right)$$
$$\left(\{\mathrm{sin\_lon}_{\mathrm{interp}}, \mathrm{SSH}_{\mathrm{std\ interp}}\}_{N_B}, (\mathrm{sin\_lon}, \mathrm{SSH}_{\mathrm{std}})\right)$$
$$\left(\{\mathrm{SSH}_{\mathrm{interp}}, \mathrm{SSH}_{\mathrm{std\ interp}}\}_{N_B}, (\mathrm{SSH}, \mathrm{SSH}_{\mathrm{std}})\right)$$
$$\left(\{\mathrm{incidence}_{\mathrm{interp}}, 1\}_{N_B}, (\mathrm{incidence}, 1/\sqrt{N_B})\right)$$
$$\left(\{\mathrm{dhdphi}_{\mathrm{interp}}, \mathrm{SSH}_{\mathrm{std\ interp}}\}_{N_B}, (\mathrm{dhdphi}, \mathrm{SSH}_{\mathrm{std}})\right)$$
$$\left(\{\mathrm{NRCS}_{\mathrm{interp}}, \mathrm{NRCS}_{\mathrm{std\ interp}}\}_{N_B}, (\mathrm{NRCS}, \mathrm{NRCS}_{\mathrm{std}})\right)$$
$$\left(\{\mathrm{VolCor}_{\mathrm{interp}}, \mathrm{VolCor}_{\mathrm{std\ interp}}\}_{N_B}, (\mathrm{VolCor}, \mathrm{VolCor}_{\mathrm{std}})\right)$$

Assuming that for each beam k, Y_k is Gaussian distributed and unbiased and that the Y_k are uncorrelated, the Maximum Likelihood Estimator (MLE) for Z is given, for all pixels (i) and lines (j), by:

$$Z[i,j] = \frac{\sum_{k\in K} Y[i,j,k]\,/(Y_{\mathrm{std}}[i,j,k])^2}{\sum_{k\in K} 1/(Y_{std}[i,j,k])^2}$$

where $K \equiv K[i,j]$ is the list of beams whose quality flag is not NOT_USEABLE.

The variance of $\mathrm{Z}[i,j]$ is

$$\langle |Z[i,j]|^2 \rangle = \left(\sum_{k\in K} \frac{1}{(Y_{std}[i,j,k])^2}\right)^{-2} \sum_{k,k'\in K,K} \frac{\langle Y[i,j,k]\, Y^*[i,j,k']\rangle}{(\mathrm{Y_{std}}[i,j,k])^2 (\mathrm{Y_{std}}[i,j,k'])^2}$$

Because the Y_k are supposed to be uncorrelated;

$$\langle Z^2[i,j] \rangle = \left(\sum_{k \in K} \frac{1}{(Y_{std}[i,j,k])^2} \right)^{-2} \sum_{k \in K} \frac{\langle |Y[i,j,k]|^2 \rangle}{(\mathrm{Y_{std}}[i,j,k])^4}$$
$$= \left(\sum_{k \in K} \frac{1}{(Y_{std}[i,j,k])^2} \right)^{-1}$$

Finally, the standard deviation is

$$Z_{std}[i,j] = \frac{1}{\sqrt{\sum_{k \in K} 1/(Y_{std}[i,j,k])^2}}$$

Note that $\mathrm{SSH_{std}}$ is computed several times but will yield the same value every times.

The combined longitude is obtained with

$$\mathrm{lon} = \arctan\left(\frac{\mathrm{sin\_lon}}{\mathrm{cos\_lon}}\right)$$

The combined quality flag is obtained while performing bitwise_OR operations over the list $K[i,j]$.

3.5.5 Accuracy

To validate the sea surface height and other KaRIn measurements we employ an end-to-end high fidelity distributed target simulation that first simulates raw complex time-sampled radar echoes including models of instrument geometry and noise characteristics, spacecraft attitude and ephemeris, ocean surface waves, tides, winds, sea surface height anomaly, and the mean sea surface; then simulates the onboard processor; and finally runs the entire KaRIn LR ground processing chain. While we have endeavored to make this simulation as realistic as possible, computational resources impose some limits on the fidelity, which we describe below.

The raw radar echo simulation generates “fast time” samples at the temporal resolution of the KaRIn analog-to-digital converter. It simulates radar echoes from an ensemble of point targets over a 26 m by 1 m grid that includes all regions on the ocean surface that contribute significant energy to the radar return as a function of time. This results in simulations with over 1 billion individual point targets for a typical 200 km long, 130 km wide simulation, which is computationally demanding even for available supercomputers. However, the 26 m spacing in along track between point targets is still insufficient to adequately sample the full Doppler spectrum of the antenna pattern, so the simulated errors in phase and thus sea surface height are very highly correlated between the 9 beams in the absence of thermal noise. Sufficiently fine sampling to avoid this limitation is not computationally feasible for large scenes.

The simulated wave fields described here are static. Wave motion is not simulated. Correlation between sigma-0 values and wave crests and troughs due to hydrodynamic modulation are also not simulated. An additional feature of the raw echo simulation is that speckle-related noise is inherent in the simulation. This feature is unavoidable if we want a high fidelity simulation that validates the processor, but it means that there is non-algorithmic random error in the simulation that we cannot turn off and need to appropriately model as part of our validation.

The OBP simulation we use for validation is the same bit-true simulation that is used to validate the OBP firmware during KaRIn hardware testing.

The last part of the end-to-end simulation is the KaRIn ground processing itself, including the upstream processing from the L2_LR_SSH product. Once ground processing is complete, errors in each measured quantity are computed by comparing with the "truth values" of that quantity that were used as inputs to the raw echo simulation.

There are several types of error that are represented in the end-to-end simulation. Only a part of that error is due to the ground processing algorithms or correctable by improvements to those algorithms. Both random and systematic errors are simulated. A major aspect of the ground processing algorithms is to remove residual systematic effects due to imperfect on-board processing that would otherwise result in systematic errors to sea surface height or other KaRIn measurements.

Systematic errors are removed from the interferometric phase as described in [5] and this correction is reported in the left/phase_bias_cor and right/phase_bias_cor variables in the L1B_LR_INTF product. Additional downstream corrections are applied including the static phase screen correction computed during cal/val and applied by the L2 pre calibration processor and the height_cor_xover computed by the XCAL processor and added the the L2 product by the L2 post calibration processor. The phase screen is a static polynominal in absolute phase (approximately equivalent to cross track distance) that is computed independently for each polarization (half-swath). The height_cor_xover value accounts for time-varying quadratic errors as a function of cross track distance due attitude knowledge error among other error sources.

Random errors, other than those caused by the algorithms themselves, are not recoverable in ground processing and thus not counted as algorithm error.

In order to separate unavoidable random noise from random errors introduced by the ground algorithms, we have developed an analytical model of the expected random SSH error from a hypothetical perfect algorithm. The details of the expected perfect algorithm error are provided in [7] [8]. Here we briefly describe the approach and its limitations. The goal of the approach is to estimate the simulated sea surface height errors we would obtain if the algorithms were perfect in the absence of thermal noise. Thermal noise can be ignored as it can be turned off in the simulation. The model accounts for random errors only, not systematic error. The algorithms are deemed to be accurate if the simulated errors match the perfect error without thermal noise or waves in the scene, and the simulated error spectra are much lower than the overall maximum error spectra levied by the science requirements. Expected errors from the simulation are worse than what we expect to see from real SWOT data because, as

described above, the simulated single-beam height errors are highly correlated between beams. Accounting for other effects as well, the reduction in random error from combining beam measurements is therefore approximately a factor of 2 lower than would be expected for real data. There are also approximations in the model that lead to overestimation or underestimation of the error. These include the following listed approximations.

- In the absence of thermal noise, errors are due to geometric decorrelation only. (Underestimation)
- Quantization error is negligible. (Underestimation)
- Errors due to surface gravity waves are negligible. (Underestimation)
- Changes in the correlation between beams due to large pitch control errors are negligible. (Overestimation, the simulated errors of the outer two beams are slightly more uncorrelated with others than the model predicts and thus average down more during beam combine)

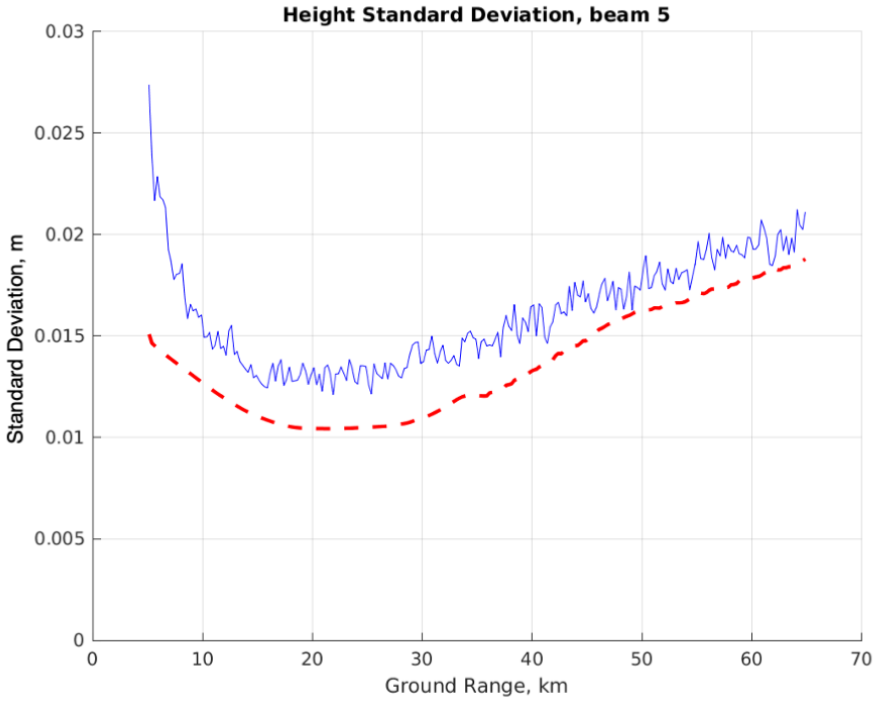

Figure 4: Comparison between simulated and expected perfect algorithm SSH error for center of nine beams for a 2000 km simulation without thermal noise or waves. The x-axis is distance along the ground from the s/c nadir track. The blue line is simulated error. The red dashed line is expected perfect algorithm error.

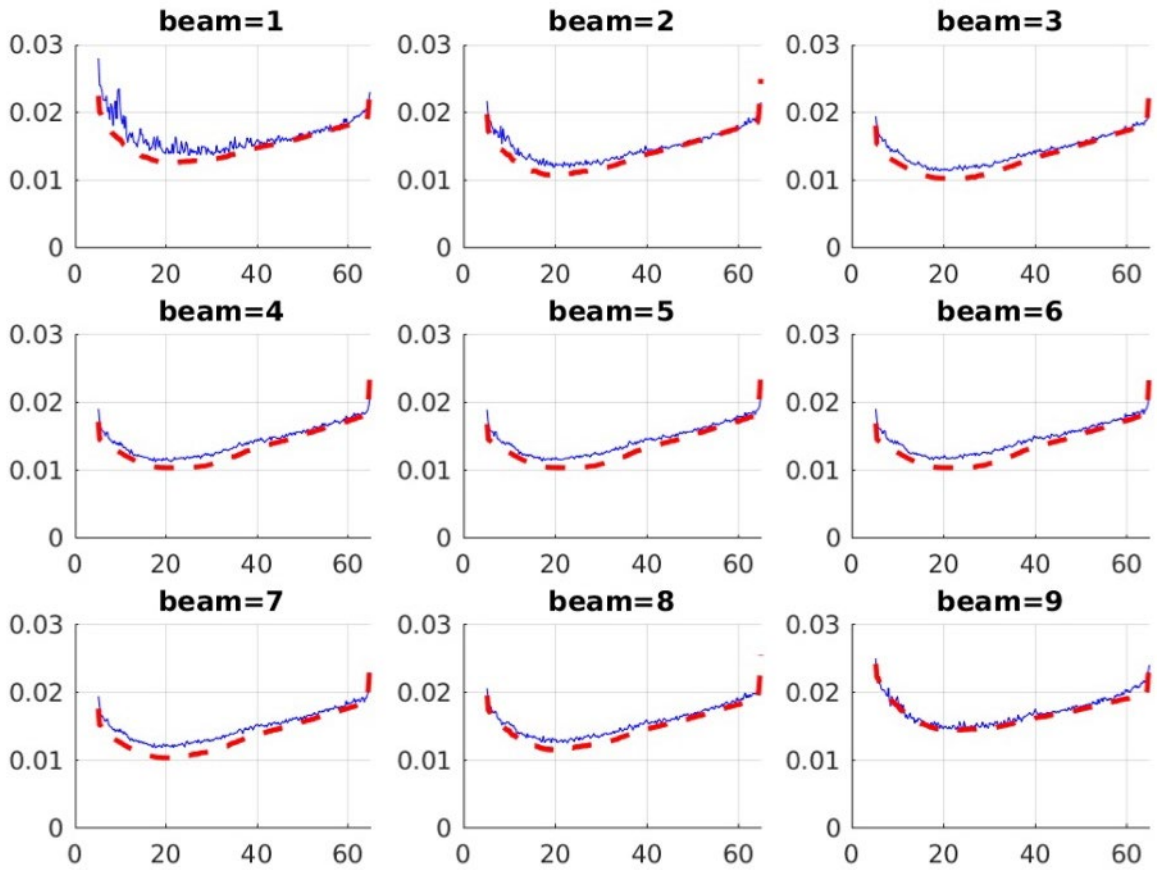

Figure 5: Comparison between simulated and expected perfect algorithm SSH error for all nine beams for a 2000 km simulation without thermal noise or waves. See Figure 4 for axis labels and units. The blue lines are simulated error. The red dashed lines are expected perfect algorithm error.

Figure 4 and Figure 5 illustrate a comparison between the simulated single beam sea surface height error and modeled expected perfect algorithm error. Figure 4 shows the center-beam (beam 5) case and Figure 5 shows all beams. The error metric plotted is the standard deviation of the height error computed over the entire 2000 km length of the simulated ground track for each cross track location. Because these are single-beam height errors, only the approximations in the model that tend to underestimate the perfect algorithm error are present. The overestimation of correlation between beams and thus overestimation of beam-combined error plays no role in single-beam heights. Because all the relevant model approximations are underestimations, the model slightly underestimates the simulated error. The underestimation is 20% at most in the 10 km to 60 m region of the ground ranges for which the science requirements are applicable. The case used in the simulation has no waves or thermal noise.

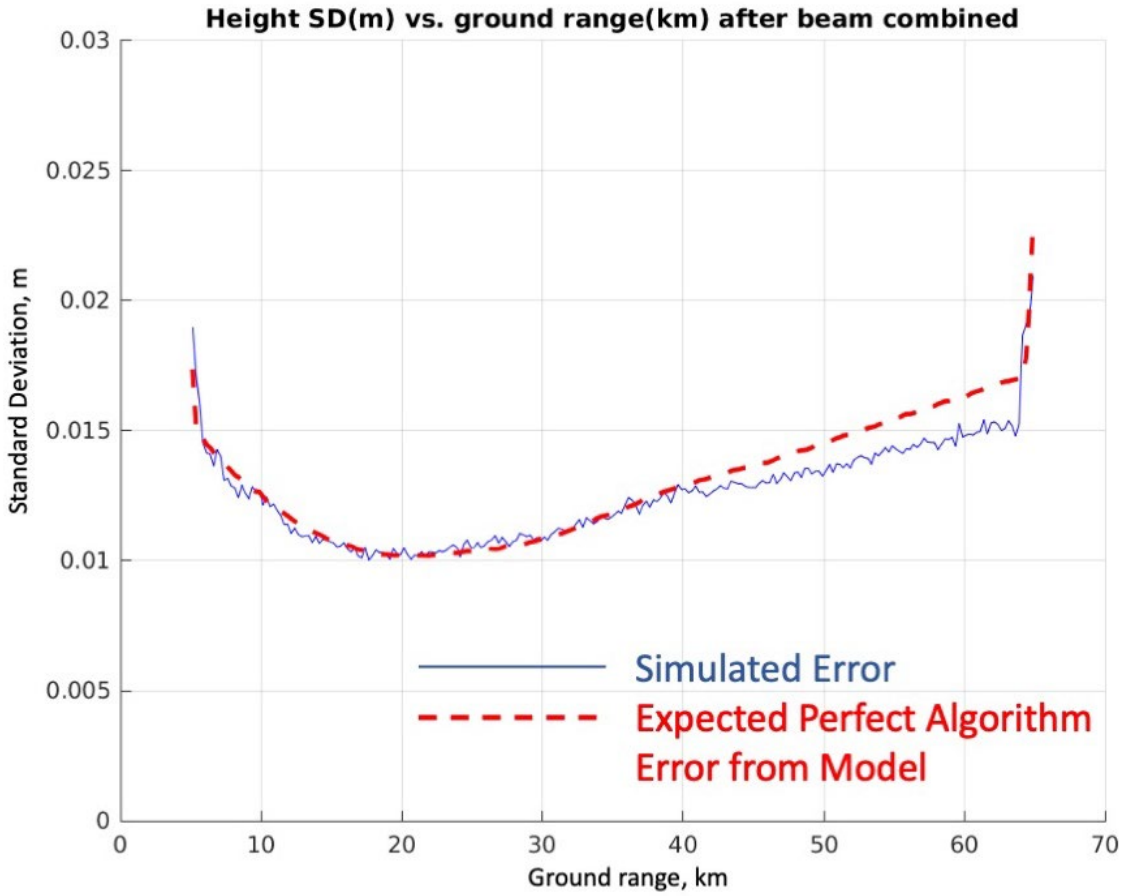

Figure 6: Comparison between beam combined (Unsmoothed) simulated and expected perfect algorithm SSH error for a 2000 km simulation without thermal noise or waves.

Figure 6 shows the same comparison for beam-combined sea surface heights in the L2_LR_SSH Unsmoothed file. Notice that the model no longer underestimates the simulated errors, but instead slightly overestimates them in the far swath. We conclude that the simulated error in the case with no waves or thermal noise is consistent with the expected perfect algorithm error. That is, the ground-processing algorithm adds negligible random error of its own.

Table 2: Simulated Attitude, Antenna Pointing, Altitude, Lever Arms, and Cross Track deviations

scene	RE_02	RE_03	RE_04	RE_05	RE_06	RE_09	RE_10	RE_11	RE_13
cross track deviation (m)	671	-1207	717	1630	489	-303	294	-787	-241
altitude deviation (m)	9	16	-49	-34	-15	-10	42	16	4
sc roll (degrees)	-0.1841	-0.194	0.0177	0.1221	0.4369	-0.0139	-0.3267	0.1127	0.0139
sc pitch (degrees)	-0.0285	0.0277	-0.0293	0.0033	-0.018	0.0162	0.0244	-0.01	0.0033
sc yaw (degrees)	0.0192	-0.1411	-0.0554	0.0894	-0.0708	0.0948	-0.1294	-0.0634	0.0082
baseline roll (mdeg)	0	0	0	-73.261	35.6675	-30.1914	-69.2891	15.4374	5.2434
baseline yaw (mdeg)	0	0	0	12.292	-6.7863	18.5846	-16.1741	13.8842	50.3768
baseline dilation (micron)	0	0	0	1.1469	21.9446	-4.2766	4.5794	18.8336	1.0984
differential roll (degrees)	0	0.1335	-0.057	-0.2251	-0.0847	-0.0074	0.0858	0.0997	-0.0318
differential pitch (degrees)	0	-0.0006	-0.0008	0.022	0.0171	0.0006	-0.0081	-0.0061	0.0101
differential yaw (degrees)	0	-0.0151	0.0649	-0.3076	0.1042	-0.1225	-0.0531	0.0566	0.1013
wave type	swell	Elfouhaily	swell	swell	Elfouhaily	Elfouhaily	from science team	swell	long swell
SWH (m)	4	2	2	2	6	2	1.58	2	1.96
wavelength (m)	224		300	300			?	300	~500
wave direction w.r.t. cross track (degrees)	30	90	0	90	90	0	?	0	90
Extras			Yaw flip redHPA	group delay	add bright points	realistic chirp	Yaw flip	2000-km	Long swell
orbit start latitude (deg)	47.966	18.402	48.459	-70.24	-48.68	11.791	11.561	-36.02	6.5238
orbit start longitude (deg)	84.284	110.76	-161.5	-134.3	-136.4	96.854	-110.3	-99.07	179.89

In Table 2, we provide the control errors in spacecraft and instrument geometry that were used to perform the simulations we discuss in this document. The error quantities were selected randomly from the expected statistical distribution during flight for each quantity. All errors represented in Table 2 are control errors, as errors in ground-reconstructed knowledge are not recoverable by the algorithms and thus are not considered errors in the KaRIn ground processing. Control errors are errors that result from parameters having values that are known but not ideal. For example, if the spacecraft yaw is 0.1 degree instead of the desired 0.0 degree that is a 0.1 degree yaw control error. Knowledge errors are when the reported value of the parameter is incorrect. For example, if the ground reconstructed spacecraft pitch at some point in time was 0.2 degrees but the true spacecraft pitch was actually 0.25 degrees that is a pitch knowledge error of 0.05 degrees.

Errors in the real-time state knowledge available to the OBP are included in the simulation, however. For example, the OBP assumes spacecraft and antenna pointing values are zero, but the error introduced by this imperfect real-time OBP knowledge is compensated by ground algorithms using the more accurate ground-reconstructed attitude.

Table 2 also includes SWH, primary wave propagation direction, and type of wave spectrum for the simulated cases. We ignore the motion of the simulated waves during observations and treat them as if they were stationary. SSH errors due to wave motion have a separate allocation in the error budget [9], and ground processing cannot mitigate these errors after the spatial averaging of the interferograms in the OBP. In addition to variations in control errors and waves, simulations also include other special cases and sensitivity analyses including non-ideal transmit chirp (RE_09), ships in scenes (RE_06), yaw-flipped operation (RE_04 and RE_10), and simulations over land (Lake Tahoe in RE_07). Two simulations were run with wave fields generated by Science Team members (RE_10 and RE_13). See Figure 7 for an example wave field. All simulations were 200 km runs in along track, except RE_11, which was 2000 km. The RE_02, RE_09, and RE_11 cases were run with waves, tides, and SSHA and also with the mean sea surface only (no waves, tides, or SSHA). All simulations were run with and without thermal noise. (The addition of thermal noise is an option that does not require the simulation of new radar echoes.) The surface backscatter was determined by selecting random ECMWF wind fields and estimating the true sigma-0 from those wind fields using a model function developed from GPM data. Locations of ocean simulations within the orbit were randomly determined for each simulation by selecting a uniformly distributed random time within the first science cycle and throwing out times that occurred over land.

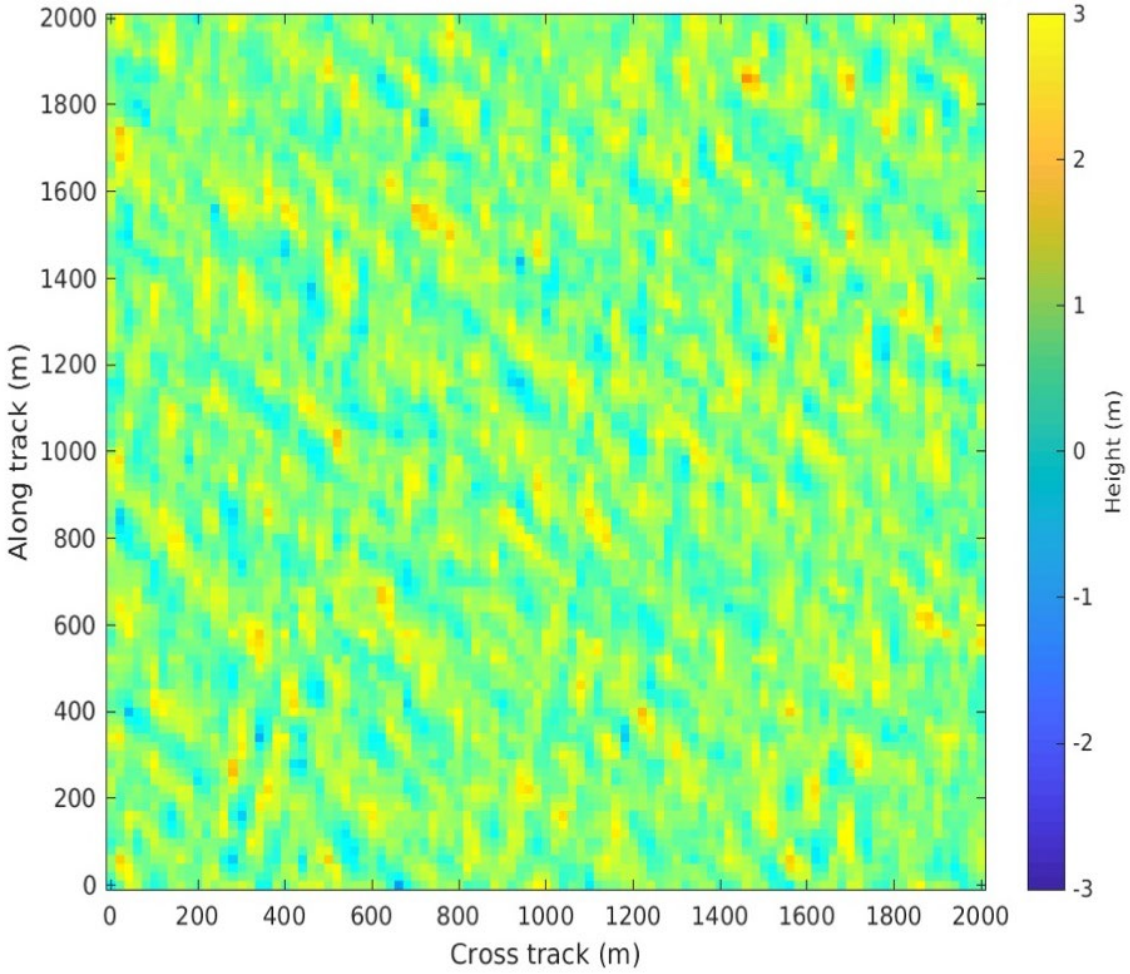

Figure 7: Example 2 km by 2 km region from the RE_10 Wave Field

The science requirement [2] on SSH error is that the along-track SSH error spectrum *E(f)* is bounded by

$$E(f) \leq 2 + 0.00125 f^{-2}\ [cm^2/(cycles/km)], \lambda \in [15{,}1000]\ km$$

E(f) is defined to be a function of the along-track spatial frequency *f* (i.e., *f=1/wavelength=1*/λ). The spatial frequency is the same as the term "wavenumber" used in some oceanographic literature (notwithstanding a possible factor of 2π in some contexts) such that the expected SSH error variance in the wavelength interval [λ_{min}, λ_{max}] is given by the integral of *E(f)* from $f = 1/\lambda_{max}$ to $1/\lambda_{min}$. Here λ refers to spatial (ocean) wavelength rather than electromagnetic (radar carrier) wavelength.

To meet this requirement, the SWOT error budget bounds the ground processing algorithm error portion of the error spectrum by $E_a(f) = 2.2 \times 10^{-6} f^{-2.5}$ $[cm^2/(cycles/km)]$, for λ>47.6 km and $E_a(f) = 0.0342$ $[cm^2/(cycles/km)]$ for $\lambda \leq 47.6$ km. As we shall see, our knowledge of the error that we should expect given perfect algorithms is insufficiently precise for us to determine whether or not the algorithm error meets this budget requirement. Instead we fall back on showing that algorithm error is much less (by a couple orders of magnitude) than the overall accuracy requirement.

As specified in [2], the height errors are first averaged down to 7.5 km resolution in cross track before the along-track spectra are computed for each 7.5 km cross-track bin. We apply a Hamming filter in the cross track direction to the height error data to achieve this. The spectra are not resampled to a uniform grid before spectrum formation. Instead we assume we can treat the slightly irregularly sampled data as if it has the nominal 250 m posting. The error spectra produced in this manner are similar to the error spectra from uniformly sampled 2-km fixed grid data (Section 3.8.5). We thus infer the slightly irregular sampling not significant. Error spectra in the along track direction are computed for the filtered (now 7.5-km cross track resolution) height errors. Finally these spectra are averaged together in the cross track direction and compared to the requirement. When simulated in this manner, there are two components of height error: algorithm error and unavoidable random error as modeled by the perfect algorithm expected error model.

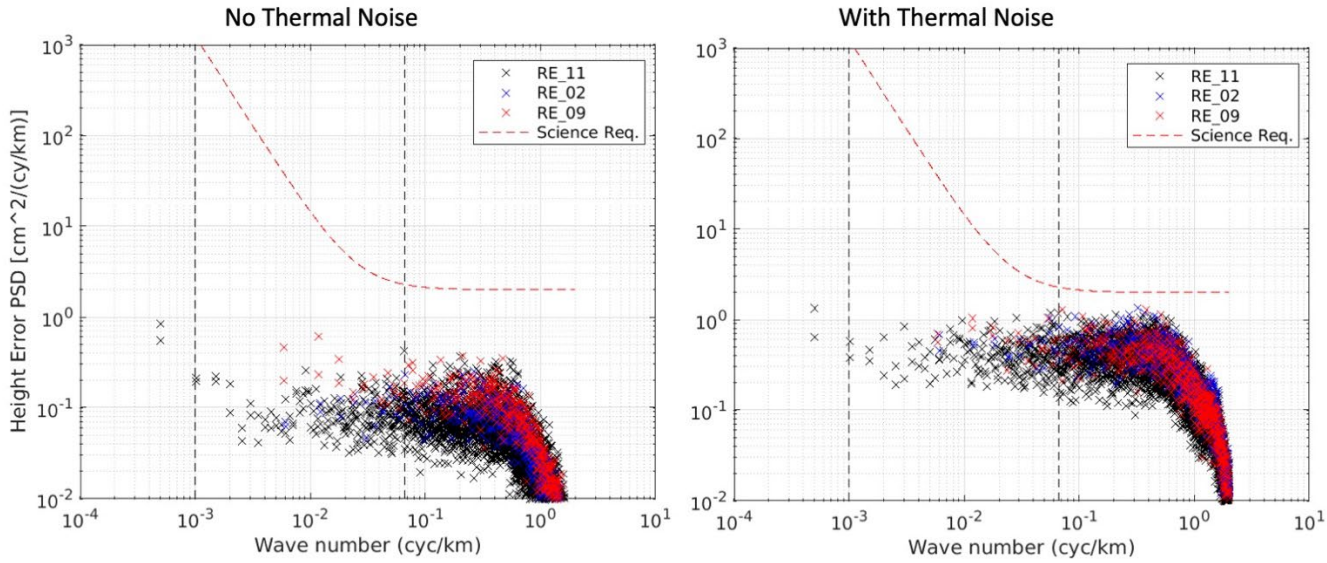

Figure 8: Mean-sea-surface-only Unsmoothed error spectra (left panel: no thermal noise, right panel: with thermal noise).

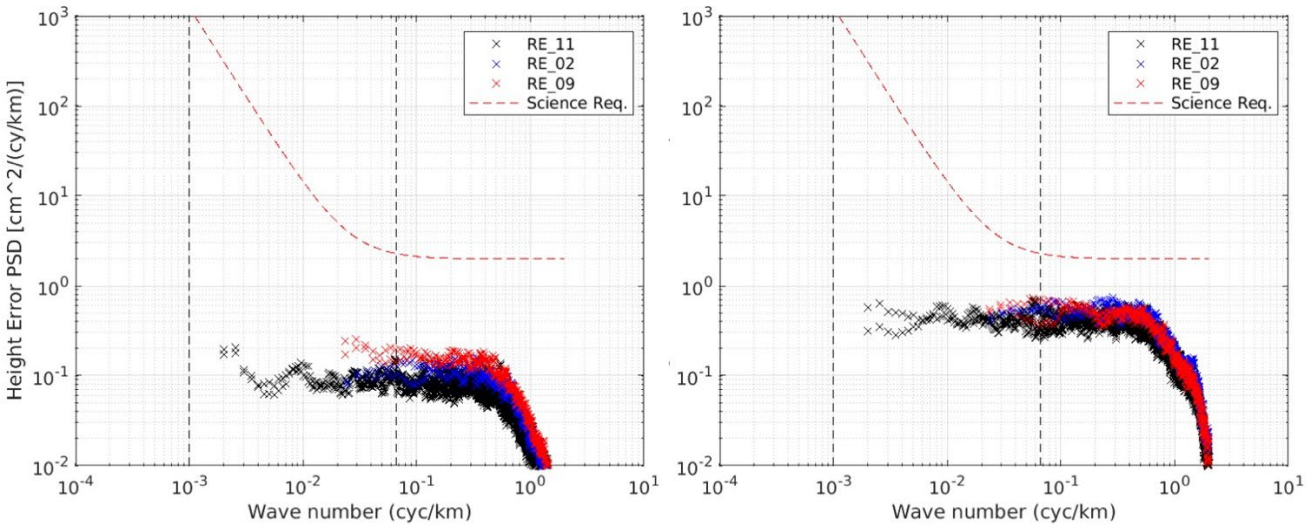

Figure 9: Mean-sea-surface-only Unsmoothed error spectra, with spectra averaged in the frequency domain using an 8 point running average (left panel: no thermal noise, right panel: with thermal noise).

Figure 8 shows the error spectra with and without thermal noise of the Unsmoothed SSH for the three simulations that were run with true surface heights on the mean sea surface with no simulated waves, tides, or SSHA. Figure 9 shows the same error spectra with an 8 point running average applied in the frequency domain to reduce random fluctuations in the spectra that result from the small size of the simulated data sets. Left half swath and right half swath spectra are not averaged together; both sets of spectra are included in the plots as separate data points. Without thermal noise, the simulated error spectra are approximately a factor of 10 below the overall requirement line for the high wave number end of the science requirement range, denoted by the vertical dashed lines. Only the 2000 km case has data at the low wave number end of the range, at which point the simulated error spectra are a factor of 5000 below the science requirement. Based upon the previous comparison between the simulated errors and the perfect algorithm error model, the residual algorithm errors are at most 20% of the simulated error and probably much less than that. This implies that algorithm error is roughly 5 times smaller than the simulated error spectra, and thus less than 2% of the science requirement.

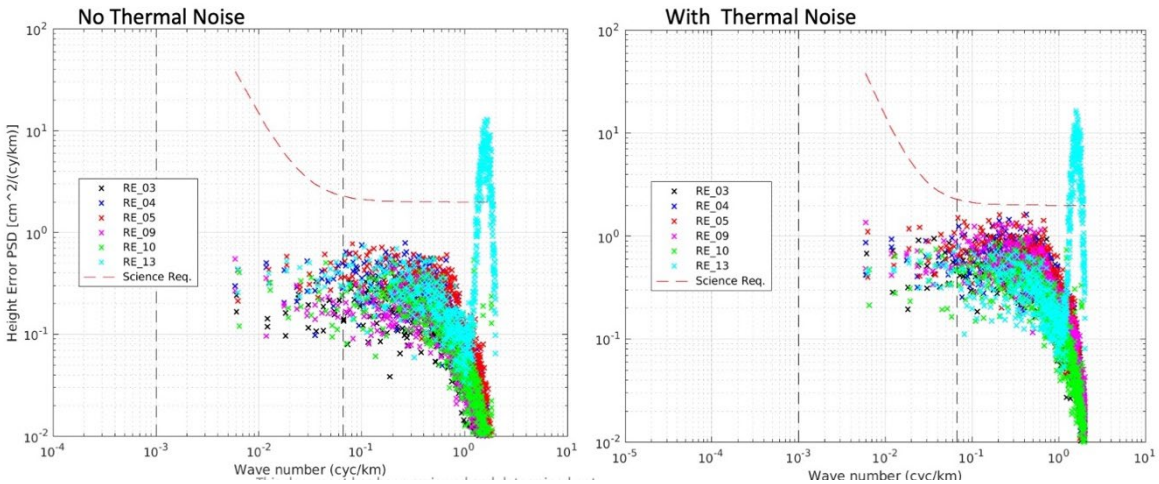

Figure 10: Unsmoothed error spectra from the 200 km long simulations with 2 m SWH (left panel: no thermal noise, right panel: with thermal noise).

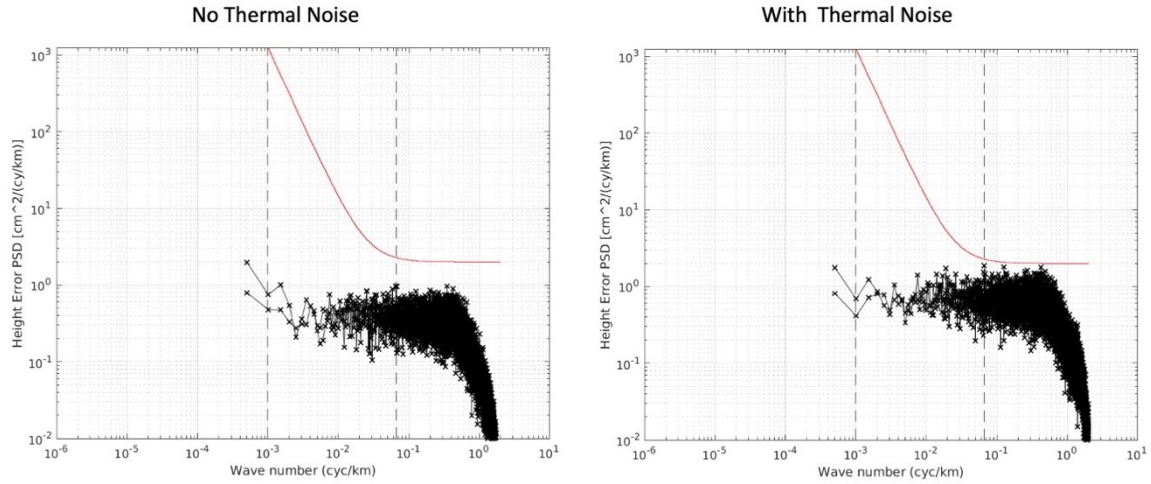

Figure 11: Unsmoothed error spectra from the 2000 km long RE_11 simulation with 2 m SWH (left panel: no thermal noise, right panel: with thermal noise).

Figure 10 and Figure 11 show simulated SSH error spectra for simulations with waves that have 2 m SWH or less, from 200 km and 2000 km long simulations, respectively. For simulations with waves, the sea surface height field that was input to the simulation included high spatial frequency information in those waves, but the 500 m resolution KaRIn measurements do not resolve them. To avoid spectral aliasing when comparing measurements to truth, we smoothed the truth field with a 500 m (2-sigma) Gaussian filter before interpolating the truth field to the measurement locations. The large bump in the spectra for RE_13 for wave numbers to the right of the required range is due to the 500 m along track swell in that simulation. For wave fields with shorter wavelengths, the filtering in the OBP removes the wave contribution to the error spectra. All of the simulations shown have the maximum 2 m SWH for which the science requirements apply, with the exception of RE_10 which has 1.5 m SWH. Without thermal noise, the simulated error spectra are all a factor of 2 below the science requirement at high wave numbers and a factor of 1000 below the error spectra at low wave numbers.

When thermal noise is added the resultant simulated error spectra are below the science requirement. We do not expect algorithm error to differ between MSS only cases and cases with waves except for errors in the sea state bias (SSB) compensation algorithm, which is the only part of the processing that explicitly accounts for waves (see below). We show cases with waves as a sanity check to rule out bugs in the presence of waves, not to quantify algorithm error. As shown above, algorithm errors are much smaller than wave-induced errors.

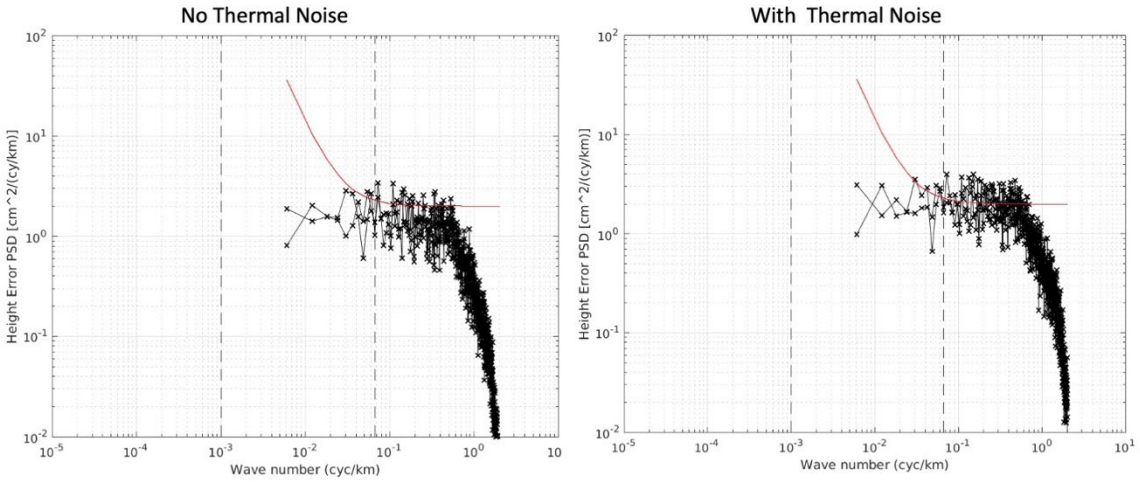

Figure 12: Unsmoothed error spectra from the 200 km long RE_02 simulation with 4 m SWH (left panel: no thermal noise, right panel: with thermal noise).

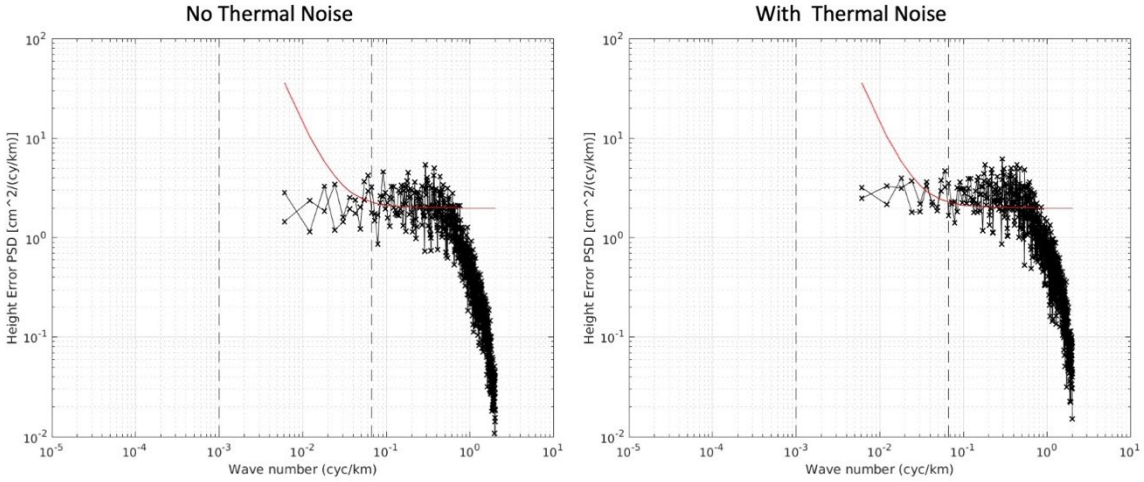

Figure 13: Unsmoothed error spectra from the 200 km long RE_02 simulation with 6 m SWH (left panel: no thermal noise, right panel: with thermal noise).

Figure 12 and Figure 13 show error spectra for simulations with 4 m and 6 m SWH, respectively. These cases are outside of the range of SWH for which the science requirements apply. The performance does not meet the white-noise floor of the science requirements, as expected, but the cases show that the algorithms can handle more stressing cases with reasonable results. Note that the performance does meet the science requirement for lower wave numbers.

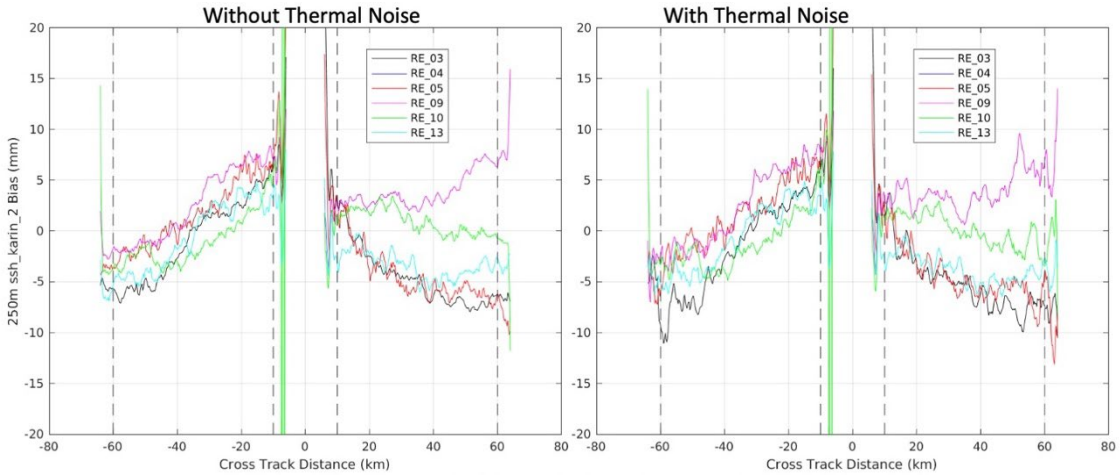

Figure 14: Unsmoothed SSH bias vs. cross track from the 200 km long cases with 2 m SWH, averaged over along track, with an 8-point (2 km) running average in cross track (left panel: no thermal noise, right panel: with thermal noise).

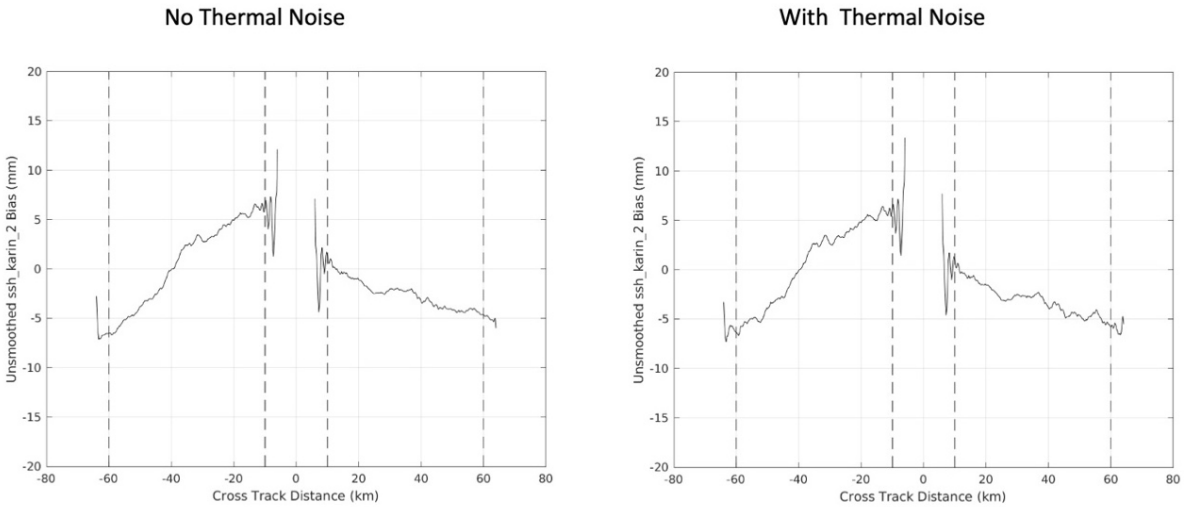

Figure 15: Unsmoothed SSH bias vs. cross track from the 2000 km long RE_11 case with 2 m SWH, averaged over along track, with an 8-point (2 km) running average in cross track (left panel: no thermal noise, right panel: with thermal noise).

Figure 14 depicts along-track averaged Unsmoothed SSH biases (mean errors) as a function of cross track location for the 2 m SWH simulations that are 200 km long. Figure 15 shows the same error metric for the RE_11, 2000 km long simulation. An 8-point (2 km) running average is applied in cross track to reduce random fluctuations due to the limited extent of the simulation. The height biases shown fall within -1 and +1 cm in the required 10 to 60 km ground-range portion of each half-swath. Most of the simulations (RE_11, RE_03, RE_05, and RE_13) have similar cross-track variation in height bias despite differences in mean sea surface, tides, SSHA, spacecraft attitude, antenna pointing, wave fields, and location in orbit. A single phase screen can remove all but a couple millimeters of the biases in these four simulations. RE_10 is yaw flipped, so, although the same phase screen may be sufficient to remove biases, we would not expect the height errors as a function of cross track to look the

same as other cases without that correction. RE_09 has a different, more realistic chirp waveform than other cases; so we might expect the residual error (that may be compensated via phase screen) for this case to be different. RE_04 is not shown on the plot because it has a constant 2 m error due to an outdated method for simulating yaw-flipped raw echo data. The height errors for the simulated cases are within a couple millimeters for all but 3 simulations where they are expected to differ for known reasons. We expect therefore, that a single phase screen will suffice so long as antennas are not moving with respect to the spacecraft frame. Time varying s/c attitude is handled properly but time varying differences in the pointing of the two antennas is not. It is also important to note that the phase screen will be computed independently for both half swaths during cal/val. We expect some asymmetry between right and left half-swaths because the antenna patterns differ between half-swaths due to the different polarizations and thus so do the antenna pattern approximation errors. Dispersive effects in the antenna pattern are approximated as described in [5].

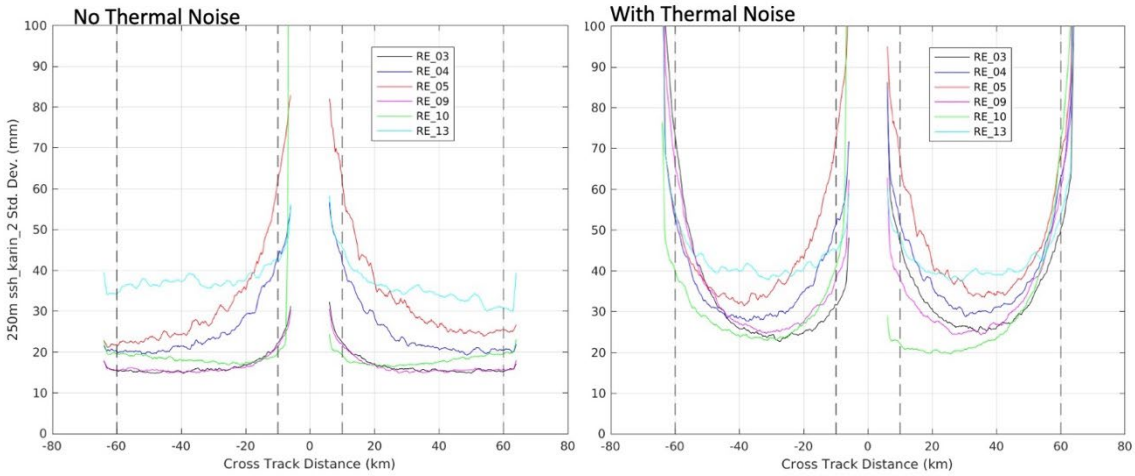

Figure 16: Unsmoothed SSH standard deviation vs. cross track from the 200 km long cases with 2 m SWH, where the standard deviation is computed over along track, and an 8-point (2-km) running average is applied in cross track (left panel: no thermal noise, right panel: with thermal noise).

Figure 16 shows the standard deviation (in the along-track direction) of the SSH error as a function of cross track for all 200 km long cases with 2 m SWH. Thermal noise only significantly affects the standard deviation for cross track locations near the edges of the 10–60 km ground-range region where the science requirements apply. The RE_13 case has much higher standard deviations due to the 500 m swell simulated in that case. As seen in the error spectra above, the additional error in the RE_13 case due to the long-wavelength swell is outside the spatial-frequency regime over which the science requirements apply.

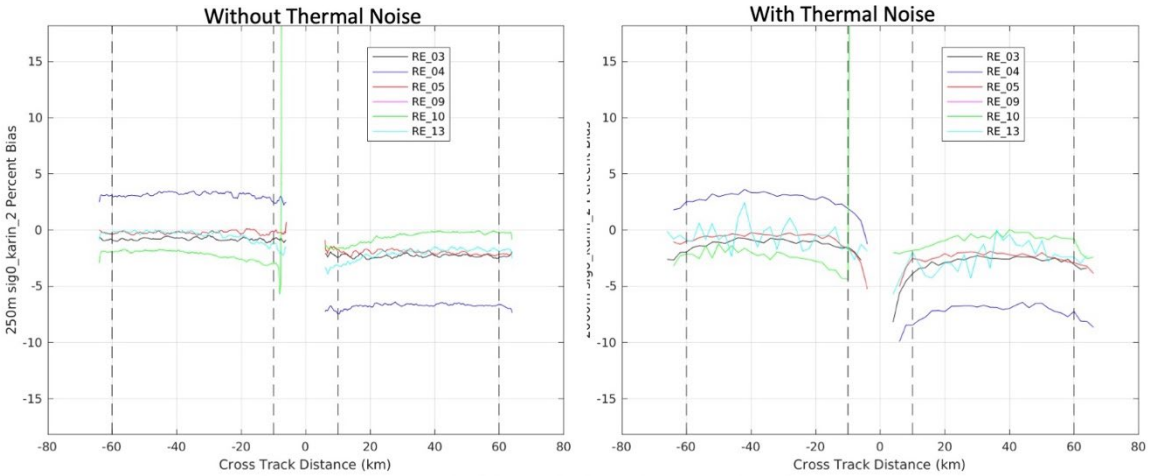

Figure 17: Unsmoothed sigma-0 percent bias vs. cross track from the 200 km long cases with 2 m SWH, averaged over the along-track direction, with an 8-point (2 km) running average in cross track (left panel: no thermal noise, right panel: with thermal noise).

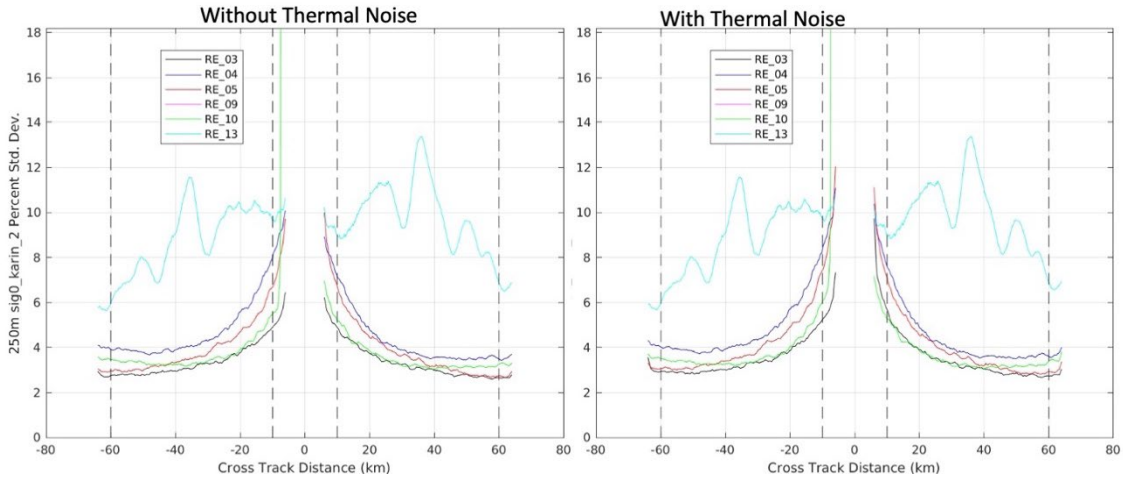

Figure 18: Unsmoothed sigma-0 percent standard deviation vs. cross track from the 200 km long cases with 2 m SWH, where the standard deviation is computed over the along-track direction, and an 8-point (2 km) running average is applied in cross track (left panel: no thermal noise, right panel: with thermal noise).

In addition to validating SSH accuracy, we also validate the Unsmoothed sigma-0 accuracy. Figure 17 depicts the percentage error in linear sigma-0 compared to the true sigma-0 value used in the raw echo simulation. As was done for SSH truth fields, sigma-0 truth fields were smoothed with a 500 m (2-sigma) Gaussian filter to avoid aliasing high spatial frequency information when interpolating the truth to the measurement locations. Biases and standard deviations were computed from sigma-0 as linear scale quantities (not expressed in decibels). Figure 18 shows the percent standard deviation, which is the standard deviation of the sigma-0 error divided by the mean of the true sigma-0, for each cross track location. An 8-point running average in cross track was applied on both percent-bias and percent-standard-deviation

quantities to reduce random fluctuations due to the limited simulation extent. Biases in sigma-0 are less than 10%. Standard deviations are less than 10% and much less than that for most of the swath for all cases except RE_13. The RE_13 simulation was exceptional in that the randomly selected truth wind field was in a low wind region that happened to be less than 1 m/s. The gradient of sigma-0 with respect to incidence angle is very high for very low winds, resulting in larger standard deviations in sigma-0.

In conclusion, error spectra due to algorithm error appear to be less than 2% of the baseline science requirement and less than 0.02% for the low-wavenumber portion of the required wavenumber regime. Simulations with waves rule out large algorithm errors in the presence of waves and suggest the overall science requirements appear to be achievable, although our simulations do not include all possible non-algorithmic sources of error. There are residual cross track SSH biases that are less than 1 cm, but these are likely to be removable using a phase screen, and they do not affect the along-track direction error spectra.

A validation of the accuracy of the 250-m geolocation is TBD.

3.6 InterpolateToFixedGrid

3.6.1 Purpose

Interpolate data from central beam native grid to Fixed grid at 250-m posting

3.6.2 Input Data

Description	Source
time	L1B_LR_INTF::[tvp_right/tvp_left]::time
Fixed grid at 250m posting	*MakeFixedGrid* (this document, 3.1)
Central Beam Native Grid	*InterpolateToCentralBeamGrid* (this document, 3.5)(equivalent of L1B_LR_INTF::[tvp_right/tvp_left]::reference_location, projected)
Combined SSH at 250m posting, 500m resolution	L2A_UNSMOOTHED::[right/left]::ssh_karin_2
Combined SSH uncertainty at 250m posting, 500m resolution	L2A_UNSMOOTHED::[right/left]::ssh_karin_uncert
Combined NRCS at 250m posting, 500m resolution	L2A_UNSMOOTHED::[right/left]::sig0_karin_2
Combined NRCS uncertainty at 250m posting, 500m resolution	L2A_UNSMOOTHED::[right/left]::sig0_karin_uncert
Height Sensitivity at 250m posting, 500m resolution	*CombineBeams* (this document, 3.5)
Combined Volumetric correlation at 250m posting, 500m resolution	*CombineBeams* (this document, 3.5)
Combined Volumetric correlation uncertainty at 250m posting, 500m resolution	*CombineBeams* (this document, 3.5)
Combined incidence angles at 250m posting, 500m resolution	*CombineBeams* (this document, 3.5)

3.6.3 Output Data

Description
time at fixed grid locations
latitude at fixed grid locations
longitude at fixed grid locations
SSH at fixed grid locations, 250m posting, 500m resolution
SSH uncertainty at fixed grid locations, 250m posting, 500m resolution
NRCS at fixed grid locations, 250m posting, 500m resolution
NRCS uncertainty at fixed grid locations, 250m posting, 500m resolution
Volumetric correlation at fixed grid locations, 250m posting, 500m resolution
Volumetric correlation uncertainty at fixed grid locations, 250m posting, 500m resolution
Height Sensitivity at fixed grid locations, 250m posting, 500m resolution
Incidence angles at fixed grid locations, 250m posting, 500m resolution

3.6.4 Mathematical Statement

The source grid (central beam grid) is denoted $\mathrm{lon}_{\mathrm{from}}, \mathrm{lat}_{\mathrm{from}}$ and has the shape $\left(N_X^{pix}, N_X^{lin}\right)$
The target grid (fixed grid) is denoted $\mathrm{lon}_{\mathrm{fixed}}, \mathrm{lat}_{\mathrm{fixed}}$ and has the shape $\left(N_Y^{pix}, N_Y^{lin}\right)$

3.6.4.1 Interpolate center beam times

Let (X, Y) be the pair of (time to interpolate, interpolated time). X and Y have respective sizes $\left(N_X^{lin}\right)$ and $\left(N_Y^{lin}\right)$.

The integer coordinates in the Y grid, $\left(\left\{j_Y \in \left[0, N_Y^{lin} - 1\right]\right\}\right)$, have corresponding real coordinates $(\{j\})$ in X given by the functions $\mathrm{line}_{\mathrm{from}}$ constructed using B.2.

$$j = \mathrm{line}_{\mathrm{from}}[j_Y]$$

We perform a linear interpolation of X at (j). The procedure can be found in C.1.2.

3.6.4.2 Interpolate means

We interpolate
- SSH
- incidences
- NRCS
- Volumetric Correlation
- Height Sensitivity

following the common procedure, described below.

Let (X, Y) be a pair of (data to interpolate, interpolated data). X and Y have respective shapes $\left(N_X^{pix}, N_X^{lin}\right)$ and $\left(N_Y^{pix}, N_Y^{lin}\right)$.

The integer coordinates in the Y grid, $\left(\left\{i_Y \in \left[0, N_Y^{pix} - 1\right]\right\}, \left\{j_Y \in \left[0, N_Y^{lin} - 1\right]\right\}\right)$, have corresponding real coordinates $(\{i\}, \{j\})$ in X given by the functions $\mathrm{pixel}_{\mathrm{from}}, \mathrm{line}_{\mathrm{from}}$ constructed using B.2.

$$i = \text{pixel}_{\text{from}}[i_Y, j_Y]$$
$$j = \text{line}_{\text{from}}[i_Y, j_Y]$$

We perform a 2 dimensional sinc interpolation of X at (i, j). The procedure can be found in C.2.3. As introduced before, sinc interpolation is selected again because it corresponds to ideal filtering (equal gain at all frequency components).

3.6.4.3 Interpolate standard deviations

We interpolate the SSH std, NRCS std and Volumetric Correlation std following the same procedure.

Let (X, Y) be a pair of (data to interpolate, interpolated data). X and Y have respective shapes $\left(N_X^{pix}, N_X^{lin}\right)$ and $\left(N_Y^{pix}, N_Y^{lin}\right)$.

The integer coordinates in the Y grid, $\left(\{i_Y \in [0, N_Y^{pix} - 1]\}, \{j_Y \in [0, N_Y^{lin} - 1]\}\right)$, have corresponding real coordinates $(\{i\}, \{j\})$ in X given by the functions

$$i = \text{pixel}_{\text{from}}[i_Y, j_Y]$$
$$j = \text{line}_{\text{from}}[i_Y, j_Y]$$

We perform a sinc interpolation of $1/X^2$ at (i, j). Then we get the square root of the inverse of the interpolated data to get Y.

3.6.5 Accuracy

We provide validation results for the measurements in the 2 km fixed grid Expert, Basic, and WindWave files in Section 3.8.5 below.

3.7 Generate250-mQualityFlag

3.7.1 Purpose

Generate quality flag for unsmoothed 250m data....

3.7.2 Input Data

Description	Source
SSH at 250m posting, 500m resolution	L2A_UNSMOOTHED::[right/left]::ssh_karin_2
SSH uncertainty at 250m posting, 500m resolution	L2A_UNSMOOTHED::[right/left]::ssh_karin_uncert

3.7.3 Output Data

Description
250m Quality Flag

3.7.4 Mathematical Statement

The details can be found in [1], Appendix B.

3.8 AverageDownTo2km

3.8.1 Purpose

Average down fixed grid quantities to 2-km using Hamming filter and decimate to 2km posting. Generate the 2-km quality flag. Thresholds for flags were assigned based upon simulated data but we expect to refine them postlaunch.

3.8.2 Input Data

Description	Source
time at 250m posting	*InterpolateToFixed* (this document,3.6)
latitude at 250m posting	*InterpolateToFixed* (this document,3.6)
longitude at 250m posting	*InterpolateToFixed* (this document,3.6)
SSH at 250m posting, 500m resolution	*InterpolateToFixed* (this document,3.6)
SSH uncertainty at 250m posting, 500m resolution	*InterpolateToFixed* (this document,3.6)
NRCS at 250m posting, 500m resolution	*InterpolateToFixed* (this document,3.6)
NRCS uncertainty at 250m posting, 500m resolution	*InterpolateToFixed* (this document,3.6)
250m SSH Quality Flag	*InterpolateToFixed* (this document,3.6)
Volumetric correlation at 250m posting, 500m resolution	*InterpolateToFixed* (this document,3.6)
Volumetric correlation uncertainty at 250m posting, 500m resolution	*InterpolateToFixed* (this document,3.6)
Height Sensitivity at 250m posting, 500m resolution	*InterpolateToFixed* (this document,3.6)
Incidence angles at 250m posting, 500m resolution	*InterpolateToFixed* (this document,3.6)
Incidence angles at 250m posting, 500m resolution	*InterpolateToFixed* (this document,3.6)

3.8.3 Output Data

Description	Output data product (if exists) [x] BASIC or EXPERT or WINDWAVE
time at 2km posting	L2B_[x]::time
latitude at 2km posting	L2B_[x]::latitude
longitude at 2km posting	L2B_[x]::longitude
SSH at 2km posting, 2km resolution	
SSH uncertainty at 2km posting, 2km resolution	
NRCS at 2km posting, 2km resolution	
NRCS uncertainty at 2km posting, 2km resolution	
2km SSH Quality Flag	
Volumetric correlation at 2km posting, 2km resolution	
Volumetric correlation uncertainty at 2km posting, 2km resolution	
Height Sensitivity at 2km posting, 2km resolution	
Incidence angles at 2km posting, 2km resolution	

3.8.4 Mathematical Statement

3.8.4.1 Average down time

Let (X, Y) be the pair of (time to average down, averaged-down time) with respective sizes $\left(N_X^{lin}\right)$ and $\left(N_Y^{lin}\right)$.

Given the averaging factor: $f_a = 8$ (2km divided by 250m) and the filter width $w_f = 17$ (which is equivalent to a window length of ~4 km , w_f must be odd), we set

$$j_{start} = \text{num\_overlap\_lines\_one\_end}$$
$$j_{end} = N_X^{lin} - \text{num\_overlap\_lines\_one\_end} - 1$$

The output shape is

$$N_Y^{lin} = \text{int}\left(1 + \frac{j_{end} - j_{start}}{f_a}\right)$$

where int(.) truncates to an integer shape.

The Hamming filter H has a shape $\left(w_f\right)$ and its coefficients are, for $n \in [0, w_f - 1]$,

$$H[n] = \frac{F[n]}{\sum_n F[n]}$$

with

$$F[n] = \left[0.54 - 0.46\cos\left(2\pi\frac{n}{w_f - 1}\right)\right]$$

For $\in [0, N_Y^{lin} - 1]$, the center coordinate for the Hamming filter is

$$j_c = j_{start} + f_a . j_Y$$

for $n \in [0, w_f - 1]$

$$\text{time}_{2\text{km}}[j_Y] = \sum_n H[n].\,\text{time}\left[j_c + n - \frac{w_f - 1}{2}\right]$$

3.8.4.2 Average down

We down average the
- latitude
- cosine of longitude
- sine of longitude
- SSH (mean and std)
- incidences
- height sensitivity
- NRCS (linear scale, mean and std)
- volumetric correlation (mean and std)

following the common procedure, described below.

Let (X, Y) be a pair of (data to average down, averaged-down data) with respective shapes $\left(N_X^{pix}, N_X^{lin}\right)$ and $\left(N_Y^{pix}, N_Y^{lin}\right)$.

Given the averaging factor: $f_a = 8$ (2km divided by 250m) and the filter width $w_f = 17$ (must be odd), we set

$$\begin{aligned} i_{start} &= \frac{w_f - 1}{2} \\ j_{start} &= \text{num\_overlap\_lines\_one\_end} \\ i_{end} &= N_X^{pix} - \frac{w_f - 1}{2} - 1 \\ j_{end} &= N_X^{lin} - \text{num\_overlap\_lines\_one\_end} - 1 \end{aligned}$$

The output shape is

$$N_Y^{pix} = \text{int}\left(1 + \frac{i_{end} - i_{start}}{f_a}\right), \qquad N_Y^{lin} = \text{int}\left(1 + \frac{j_{end} - j_{start}}{f_a}\right)$$

where int(.) strips off the number decimals.

A default configuration sets num_overlap_lines_one_end = 8.

The Hamming filter H has a shape (w_f, w_f) and its coefficients are, for $m \in [0, w_f - 1], n \in [0, w_f - 1]$,

$$H[m, n] = \frac{F[m, n]}{\sum_{m,n} F[m, n]}$$

with

$$F[m, n] = \left[0.54 - 0.46\cos\left(2\pi \frac{m}{w_f - 1}\right)\right]\left[0.54 - 0.46\cos\left(2\pi \frac{n}{w_f - 1}\right)\right]$$

For $i_Y \in [0, N_Y^{pix} - 1], j_Y \in [0, N_Y^{lin} - 1]$,

The sample value and quality flag are initiated

$$X_{2\text{km}}[i_Y, j_Y] = 0$$
$$X_{\text{degraded\_2km}}[i_Y, j_Y] = 0$$
$$\text{num\_pt}_{2\text{km}}[i_Y, j_Y] = 0$$
$$\text{num\_pt\_degraded}_{2\text{km}}[i_Y, j_Y] = 0$$
$$\text{quality\_flag}_{2\text{km}}[i_Y, j_Y] = 0\text{x}0$$
$$\text{quality\_flag\_degraded}_{2\text{km}}[i_Y, j_Y] = 0\text{x}0$$

the center coordinates for the Hamming filter are

$$i_c = i_{start} + f_a . i_Y$$
$$j_c = j_{start} + f_a . j_Y$$

for $m \in [0, w_f - 1], n \in [0, w_f - 1]$

$$\text{qual\_flag} = \text{quality\_flag}\left[i_c + m - \frac{w_f - 1}{2}, j_c + n - \frac{w_f - 1}{2}\right]$$

If (qual_flag bAND QUAL_IND_NOT_USEABLE = 0) & (qual_flag bAND QUAL_IND_DEGRADED = 0):

$$:X_{2\text{km}}[i_Y, j_Y] = X_{2\text{km}}[i_Y, j_Y] + H[m, n] . X\left[i_c + m - \frac{w_f - 1}{2}, j_c + n - \frac{w_f - 1}{2}\right]$$

$$\text{num\_pt}_{2\text{km}}[i_Y, j_Y] = \text{num\_pt}_{2\text{km}}[i_Y, j_Y] + 1$$

$$\text{quality\_flag}_{2\text{km}}[i_Y, j_Y] = \text{quality\_flag}_{2\text{km}}[i_Y, j_Y] \text{ bOR qual\_flag}$$

Elif (qual_flag bAND QUAL_IND_NOT_USEABLE = 0):

$$X_{\text{degraded\_2km}}[i_Y, j_Y] = X_{\text{degraded\_2km}}[i_Y, j_Y] + H[m, n] . X\left[i_c + m - \frac{w_f - 1}{2}, j_c + n - \frac{w_f - 1}{2}\right]$$

$$\text{num\_pt\_degraded}_{2\text{km}}[i_Y, j_Y] = \text{num\_pt\_degraded}_{2\text{km}}[i_Y, j_Y] + 1$$

$$\text{quality\_flag\_degraded}_{2\text{km}}[i_Y, j_Y] = \text{quality\_flag\_degraded}_{2\text{km}}[i_Y, j_Y] \text{ bOR qual\_flag}$$

End for

If ($\text{num\_pt}_{2\text{km}}[i_Y, j_Y] \leq$ thresh_num_good_and_suspect):

$$X_{2\text{km}}[i_Y, j_Y] = X_{\text{degraded\_2km}}[i_Y, j_Y]$$

$$\text{num\_pt}_{2\text{km}}[i_Y, j_Y] = \text{num\_pt\_degraded}_{2\text{km}}[i_Y, j_Y]$$

$$\text{quality\_flag}_{2\text{km}}[i_Y, j_Y] = \text{quality\_flag\_degraded}_{2\text{km}}[i_Y, j_Y]$$

Elif $\text{num\_pt\_degraded}_{2\text{km}}[i_Y, j_Y] = 0$:

$$X_{2\mathrm{km}}[i_Y, j_Y] = \mathrm{FILL\_VALUE}$$

The code below shows that, initially only 250m pixels of GOOD and SUSPECT quality are considering when averaging. If their number is not enough (below a threshold that is by default 50), then also DEGRADED pixels are considered. The quality flag at 2km is a logical OR of the quality values of the pixels used when averaging only.

It should be noted that if all 250-m pixels within the averaging kernel support are BAD quality, the respective 2-km pixel will be not valid (FILL_VALUE). If only one DEGRADED 250-m pixel were available, the respective 2-km pixel would contain a valid value. The variable $\mathrm{num\_pt}_{2\mathrm{km}}$ is of special intereset here, containing for this particular example the value of 1.

Two additional quality flags are build when averaging. When at least one SUSPECT pixel is used in averaging, the flag QUAL_IND_AVG_WINDOW_USED_SUSPECT is activated. Finally, when the number of 250m pixels considered is below the possible maximum value of 17x17, the flag QUAL_IND_NUM_PIXELS_AVG_SUSPECT is activated.

Check quality flag

If $\mathrm{quality\_flag}_{2\mathrm{km}}[i_Y, j_Y]$ AND QUAL_FLAG_NOT_USEABLE:

$$X_{2\mathrm{km}}[i_Y, j_Y] = \mathrm{FILL\_VALUE}$$

3.8.5 Accuracy

In this section, we provide simulation results for the measurements in the 2 km fixed-grid Expert, Basic, and WindWave files. The simulations used to obtain these results are described in in Section 3.5.5 above.

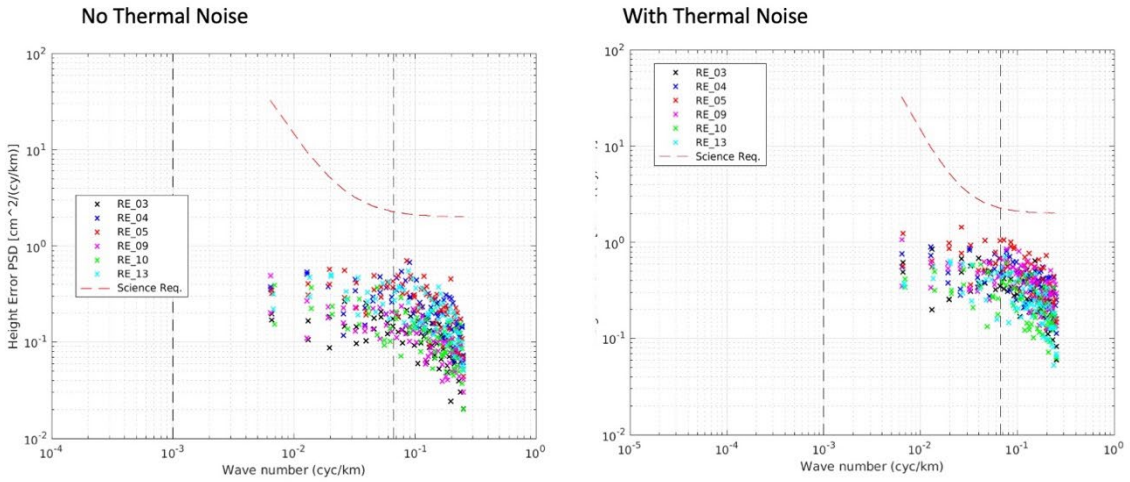

Figure 19: Basic error spectra from 200 km long simulations with 2 m SWH (left panel: no thermal noise, right panel: with thermal noise).

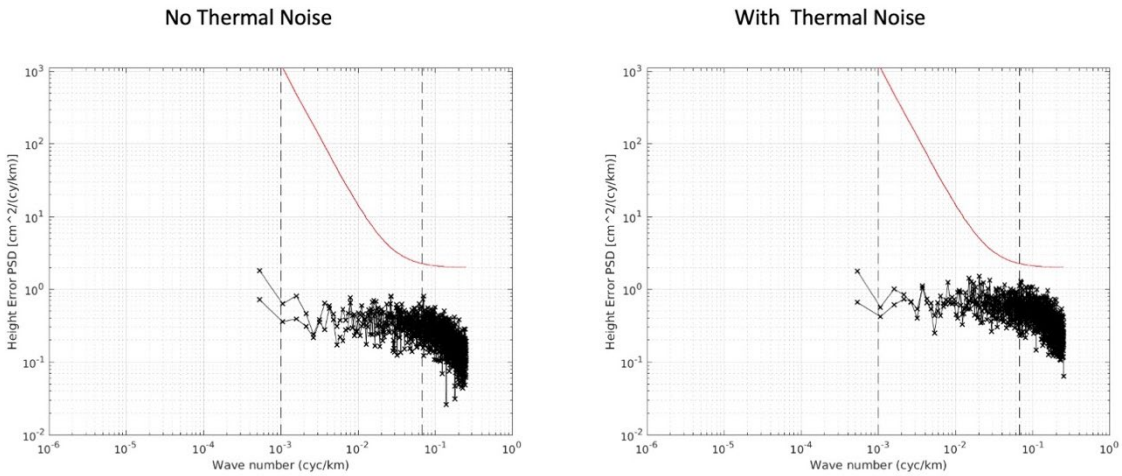

Figure 20: Basic error spectra from the 2000 km long RE_11 simulation with 2 m SWH (left panel: no thermal noise, right panel: with thermal noise).

Figure 19 and Figure 20 show the error spectra for 2 km Basic (fixed-grid) SSH for 2 m SWH cases. When comparing these spectra to the Unsmoothed error spectra in Figure 10 and Figure 11, we see that neither the additional filtering used to average down the Unsmoothed SSH to 2 km nor the interpolation to go from the native grid to the fixed grid cause any noticeable additional energy in the error spectra. To avoid aliasing of high-spatial-frequency variations in the truth field, a 2000 m (2-sigma) Gaussian filter was applied before interpolating the truth to the fixed measurement grid. This filter is wider than the 500 m filter used to smooth the truth for the Unsmoothed measurements because of the coarser sampling grid of the Basic data.

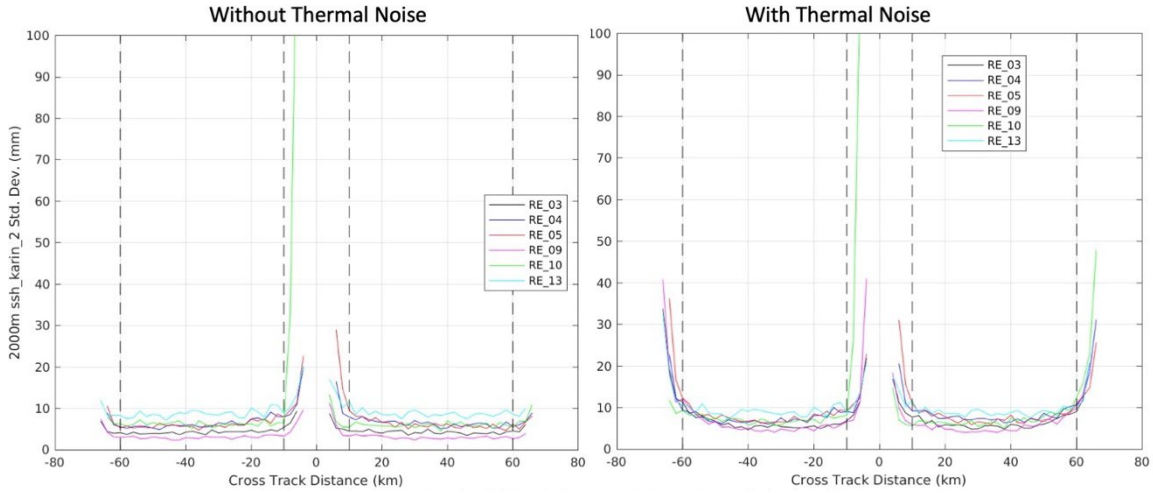

Figure 21: Basic SSH standard deviation vs. cross track from 200-km long cases with 2 m SWH, where the standard deviation is computed over the along-track direction (left panel: no thermal noise, right panel: with thermal noise).

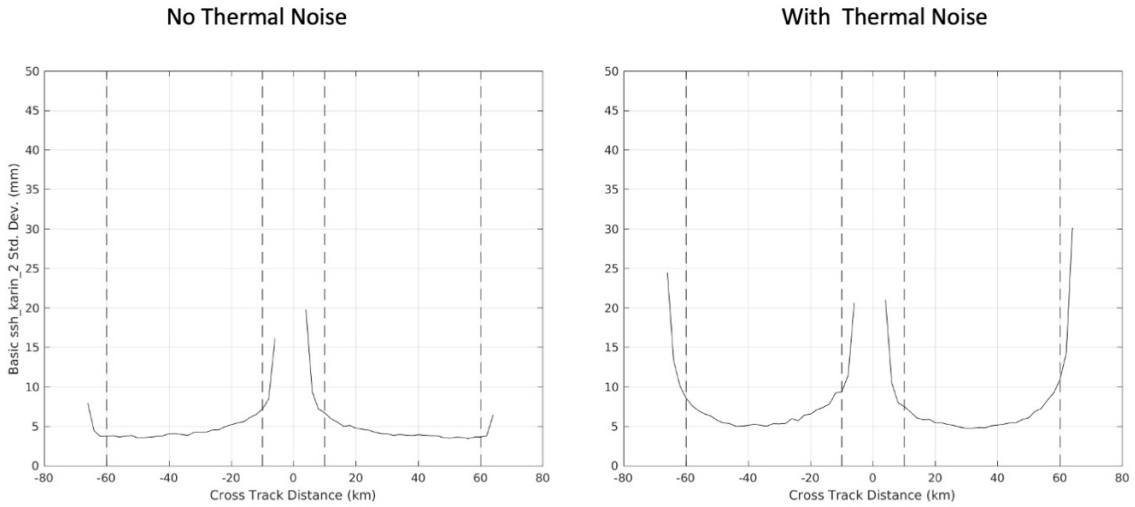

Figure 22: Basic SSH standard deviation vs. cross track from the 2000 km long RE_11 simulation with 2 m SWH, where the standard deviation is computed over the along-track direction (left panel: no thermal noise, right panel: with thermal noise).

Figure 21 and Figure 22 show the standard deviation of the errors in the 2 km Basic SSH. Comparing Figure 21 to Figure 16 shows that the averaging to coarser resolution reduces the standard deviation as one would expect. Biases (not shown) are unchanged between the Unsmoothed and Basic SSH.

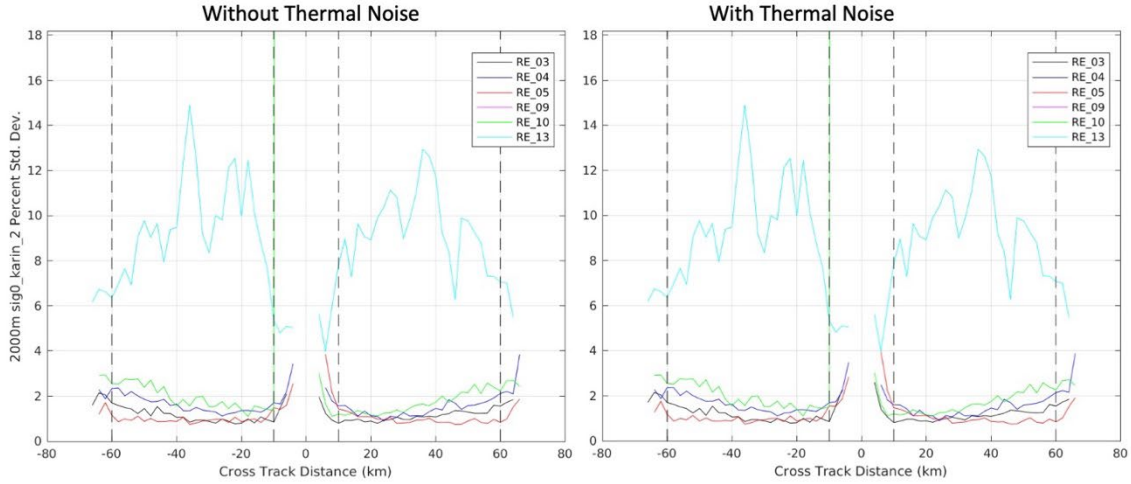

Figure 23: WindWave sigma-0 percent standard deviation vs. cross track from the 200 km long cases with 2 m SWH, where the standard deviation is computed over the along-track direction (left panel: no thermal noise, right panel: with thermal noise).

Figure 23 shows the percent standard deviation in the 2 km WindWave sigma-0 values. All cases except RE_13 show significant reduction in standard deviation due to averaging, as expected. (See Figure 18 for a comparison.) As mentioned earlier, the RE_13 case has larger errors than other cases because it was simulated for an extremely low wind speed regime (< 1 m/s) where the gradient of sigma-0 with respect to incidence angle is very large.

In conclusion, the extra processing steps needed to go from 250 m native-grid, Unsmoothed SSH and sigma0 to 2 km fixed-grid values do not appear to introduce significant additional energy in the error spectra, and they do reduce the standard deviations of both quantities.

3.9 ComputeSignificantWaveHeights

3.9.1 Purpose

Given the volumetric decorrelation of each 2km sample, computes the significant wave heights.

3.9.2 Input Data

Description	Source [x]: EXPERT or WINDWAVE or BASIC
Volumetric decorrelation, at 2km posting, 2km resolution	AverageDownTo2km (this document, 3.8)
Volumetric decorrelation uncertainty, at 2km posting, 2km resolution	AverageDownTo2km (this document, 3.8)
Height Sensitivity at 2km posting, 2km resolution	AverageDownTo2km (this document, 3.8)
time at 2km posting	L2B_[x]::time
latitude at 2km posting	L2B_[x]::latitude
longitude at 2km posting	L2B_[x]::longitude
ECMWF model	auxiliary and ancillary data
Meteo France Wave Model (MF-WAM)	auxiliary and ancillary data

3.9.3 Output Data

Description	Output data product (if exists) [x] EXPERT and WINDWAVE
SWH, at 2km posting, 2km resolution	L2B_[x]::swh_karin
SWH uncertainty, at 2km posting, 2km resolution	L2B_[x]::swh_karin_uncert
ECMWF model for significant wave height	L2B_[x]::swh_model
Mean sea surface wave direction from the Meteo France Wave Model (MF-WAM)	L2B_[x]::mean_wave_direction
Sea surface wind wave mean period from the second moment of the wave model spectral density from the Meteo France Wave Model (MF-WAM)	L2B_[x]::mean_wave_period_t02

3.9.4 Mathematical Statement

The volumetric decorrelation (C_{vol}) can be associated to the Significant Wave Height ([10]) using the equation

$$C_{\mathrm{vol}} = \exp\left(-\frac{1}{2}(\partial_h \varphi)^2 . \left(\frac{\mathrm{SWH}}{4}\right)^2\right)$$

where $\partial_h \varphi = \partial\varphi/\partial h$ is the inverse of the height sensitivity.

The estimation uses a least squares method on the volumetric correlation normalized with the standard deviation of the volumetric correlation. The normalization allows more weight to be given to points with less noise, as the noise density is not constant in the cross-track direction.

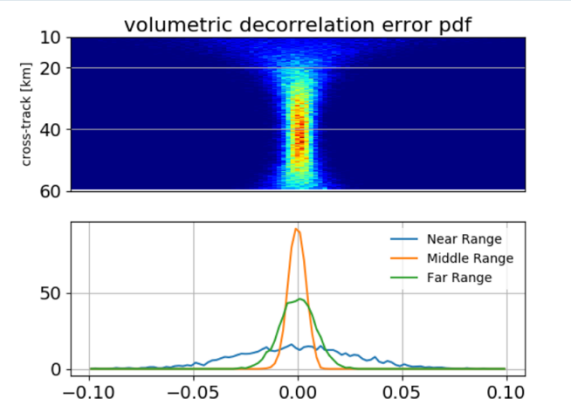

Figure 24: Probability density function for volumetric correlation (SWH=2m)

For all the lines $j \in [0, N^{lin} - 1]$,
For a set of possible values of SWH, $\{\text{swh}\}_\text{n} = \left[0, \frac{20.}{0.01}\right] \times 0.01$, we compute the least-squares cost function

$$\text{cost}[n] = \sum_{i=0}^{N^{pix}-1} \left[\frac{\hat{C}_{\text{vol}}[i,j] - \exp\left(-\frac{1}{2}(\partial_h \varphi[i,j])^2 . \left(\frac{\text{swh}[n]}{4}\right)^2\right)}{\sigma_{vol}[i,j]} \right]^2$$

The estimated SWH is the one that minimizes the cost value

$$\widehat{\text{SWH}}[i,j] = \text{swh}[\text{arg\_min}(\text{cost})]$$

For a set of possible values of SWH standard deviation, $\{\sigma_{\text{swh}}\}_\text{n} = \left[0, \frac{20.}{0.01}\right] \times 0.01$, we compute the function (see Appendix D)

$$f[n] = \left| \sum_{i=0}^{N^{pix}-1} \frac{(\partial_h \varphi[i,j])^2}{\sigma_{vol}^2[i,j]} \frac{1}{\sigma[n,i,j]} \exp\left(-\frac{(\partial_h \varphi[i,j])^2}{16} \widehat{\text{SWH}}^2[i,j] \left[1 + \frac{\sigma_{\text{swh}}^2[n]}{32\sigma^2[n,i,j]}\right]\right) \right|$$

where

$$\sigma[n,i,j] = \sqrt{1 + \frac{\sigma_{\text{swh}}^2[n](\partial_h \varphi[i,j])^2}{16}}$$

The estimated standard deviation of SWH minimizes the function

$$\hat{\sigma}_{\text{swh}}[i,j] = \sigma_{\text{swh}}[\text{arg\_min}(f)]$$

Note that the because $f[n]$ uses a sum over the pixels, only one estimate per line is available. Because the SWH is stored in data products on the same grids than SSH (among others), we restore the pixels

dimension by duplicating the scalar estimate for all the pixels of the line.

Use the GECO library to obtain the gridded values of

- *swh_model*
- *mean_wave_direction*
- *mean_wave_period_t02*

See the GECO documentation [11] for corresponding mathematical statement.

3.9.5 Accuracy

3.9.5.1 Algorithm versus geophysical truth

Using the same wave model as proposed in [12], [13] showed that currents are a cause of small scale gradients of SWH (Figure 25 and associated spectra Figure 26). When ocean currents are not accounted for in the wave model, the SWH spectra follow a k^{-5} or steeper slope (which justify the original assumptions of [9]). However when the interaction between the wave field and ocean currents is accounted for, the SWH PSD slope follows the ocean current slope ($k^{-2.5}$) (and the energy for wavelengths smaller than 50 km can be 3 orders of magnitude greater than what is assumed by [9]).

The SWH retrieval algorithm shows some limitation regarding the spatial variations of the observed SWH field:

- only one scalar SWH value per swath is computed to achieve a reasonable estimator uncertainty at all range position.
- the SWH estimate is primarily representative of early mid-range sea-state conditions (around 20km, from simulation-based studies), since the fitted model is not sensitive in the medium to far range and the estimation uncertainties mostly affect volumetric correlation estimations at near and far range.

Consequently, the small-scale gradients of SWH are not reproduced in the estimated SWH map. The SWH estimates can then be significantly inaccurate under particular geophysical conditions, such as strong current gradients (Figure 25) to cite one example, where the energy for the small wavelengths might be important.. Note that this inaccuracy has an indirect impact on the SSH accuracy through the Sea State Bias correction, (see 3.11.5.1).

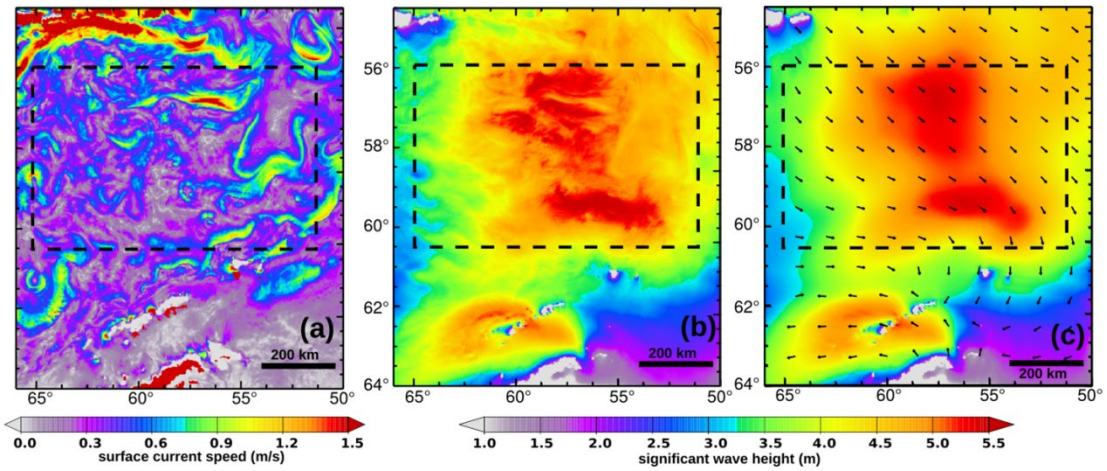

(a) (b) (c)

Figure 25: From [13]. Drake passage. (a) Current from MITgcm. (b) SWHfrom WW3 using current. (c) SWH from WW3: no current.

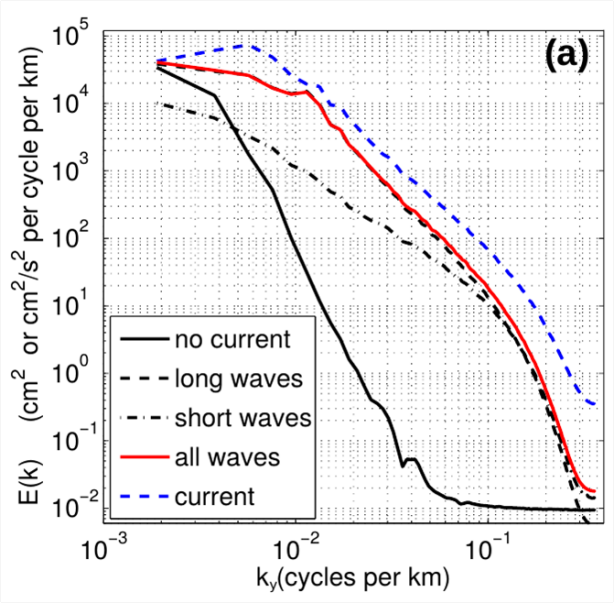

Figure 26: From [13]. The black and red solid lines (cm^2/(cycles/km)) and the dashed blue line (cm^2/s^2/(cycles/km)) are respectively the spectra of **Figure 25**-(c), **Figure 25**-(b) and **Figure 25**-(a). The SWH spectrum with currents follows the current spectrum (in $k^{-2.5}$). Note that at periods $< (g.2\pi.[k_y \times 10^{-3}])^{-1/2} = 6.$ s, the short waves exceed the long waves.

3.9.5.2 Algorithm accuracy

TBD

3.10 ComputeWindSpeed

3.10.1 Purpose

Retrieve wind speeds from sigma-0 values, instrument geometry, and ECMWF model wind directions. This routine is run twice: first using sig0_karin_2, the sigma-0 value computed used model-based atmospheric attenuation correction and then again using sig0_karin which was computed by removing the model-based correction and then applying an atmospheric attenuation correction based from radiometer data. The wind retrieval algorithm is applied independently to each 2-km by 2-km pixel on the fixed grid.

3.10.2 Input Data

Description	Source [x] : EXPERT or WINDWAVE
Incidence angles at 2km posting, 2km resolution	*AverageDownTo2km* (this document, 3.8)
heading angles at 2km posting, 2km resolution	
NRCS estimation $\tilde{\sigma}^0$	L2B_[x]::sig0_karin_2
NRCS uncertainty	L2B_[x]::sig0_karin_uncert
Wind speed from radiometer	L2B_[x]::wind_speed_rad
time at 2km posting	L2B_[x]::time
latitude at 2km posting	L2B_[x]::latitude
longitude at 2km posting	L2B_[x]::longitude
Wind Speed GMF	auxiliary and ancillary data
ECMWF model	auxiliary and ancillary data
Meteo France Wave Model (MF-WAM)	auxiliary and ancillary data

3.10.3 Output Data

Description	Output data product (if exists) [x] : EXPERT and WINDWAVE
Wind Speed at 2km posting, 2km resolution	L2B_[x]::wind_speed_karin_2
Wind Speed at 2km posting, 2km resolution, estimated with models for inputs.	
Wind Speed uncertainty at 2km posting, 2km resolution	L2B_[x]::wind_speed_karin_uncert_2
Easterly (u) component of the ECMWF model wind speed at 10 meters	L2B_[x]::wind_speed_model_u
Northerly (v) component of the ECMWF model wind speed at 10 meters	L2B_[x]::wind_speed_model_v

3.10.4 Mathematical Statement

The wind estimation (with θ and $\tilde{\sigma}^0$ as scalar inputs) from the input GMF, follows the below procedure.

If θ or σ^0 is outside the ranges of the GMF a fill value is returned

Find n_θ, the incidence angle index, i.e., the index where

$$\theta_{\mathrm{GMF}}[n_\theta] < \theta \leq \theta_{\mathrm{GMF}}[n_\theta + 1]$$

construct vector $\{\sigma^0_{\mathrm{interp}}\}_m$ which is a linear interpolation between $\{\sigma^0_{\mathrm{GMF}}[m, n_\theta]\}_m$ and $\{\sigma^0_{\mathrm{GMF}}[m, n_\theta + 1]\}_m$

Set $\Delta_{\sigma 0}$, the sign of the derivative of $\sigma^0_{\mathrm{interp}}$. $\sigma^0_{\mathrm{interp}}$ is checked to be monotonic, otherwise the procedure returns a fill value.

Find m_{ws}, the wind index, i.e. the index where

$$\Delta_{\sigma 0}.\sigma^0_{\mathrm{interp}}[m_{\mathrm{ws}}] < \Delta_{\sigma 0}.\sigma^0 \leq \Delta_{\sigma 0}.\sigma^0_{\mathrm{interp}}[m_{\mathrm{ws}} + 1]$$

Compute the wind speed

$$\mathrm{ws} = \mathrm{ws}_{\mathrm{GMF}}[m_{\mathrm{ws}}] + \left(\sigma^0 - \sigma^0_{\mathrm{interp}}[m_{\mathrm{ws}}]\right) \frac{\mathrm{ws}_{\mathrm{GMF}}[m_{\mathrm{ws}} + 1] - \mathrm{ws}_{\mathrm{GMF}}[m_{\mathrm{ws}}]}{\sigma^0_{\mathrm{interp}}[m_{\mathrm{ws}} + 1] - \sigma^0_{\mathrm{interp}}[m_{\mathrm{ws}}]}$$

For all the lines $j \in [0, N^{lin} - 1]$, For all the pixels $i \in [0, N^{pix} - 1]$,
The above procedure is used to estimate the wind speed $\mathrm{ws}[i,j]$ using $\theta \equiv \tilde{\theta}[i,j]$ and $\sigma^0 \equiv \tilde{\sigma}^0[i,j]$

The standard deviation estimation uses twice the procedure

- to estimate the wind speed $\mathrm{ws}_{\mathrm{std}+}[i,j]$ using $\theta \equiv \tilde{\theta}[i,j]$ and $\sigma^0 \equiv \tilde{\sigma}^0[i,j] + \frac{\tilde{\sigma}^0_{\mathrm{std}}[i,j]}{2}$
- to estimate the wind speed $\mathrm{ws}_{\mathrm{std}-}[i,j]$ using $\theta \equiv \tilde{\theta}[i,j]$ and $\sigma^0 \equiv \tilde{\sigma}^0[i,j] - \frac{\tilde{\sigma}^0_{\mathrm{std}}[i,j]}{2}$

Then

$$\mathrm{ws}_{\mathrm{std}}[i,j] = \mathrm{ws}_{\mathrm{std}+}[i,j] - \mathrm{ws}_{\mathrm{std}-}[i,j]$$

3.10.5 Accuracy

3.10.5.1 Algorithm versus geophysical truth

In addition to wind variations, several other phenomena can modulate the ocean surface roughness and thus the NRCS. If their effects are not considered in the data interpretation, erroneous wind speeds may be obtained. In contrast to a scatterometer, a radar system can resolve most of the phenomena, and their characteristic signatures can be identified and considered in the data interpretation. The most relevant phenomena are characterized as follows:

- Oceanic fronts can become visible in radar images as bright lines with an NRCS increase of several dB within a width of a few hundred meters and /or as boundaries between areas with different mean NRCS values, looking very much like atmospheric fronts. The appearance of Radar signatures of oceanic fronts depends on the strength of the current convergence and current shear and on the angle between the orientation of the front and the radar look direction. Different NRCS values on both sides of the front can result from

wave refraction at the front, different compositions of the water masses separated by the front (surface films, salinity...), or from different atmospheric stratifications due to different water temperatures and corresponding different air-sea temperature differences. Some of these effects are discussed by [14].

- Oceanic internal waves can give rise to pronounced wave-like signatures such as the ones in Figure 27 (a) with wavelengths on the order of kilometers and crest lengths of tens to hundreds of kilometers. The strength of the positive and negative modulation of the NRCS depends on the strength of the surface current gradients as well as on the wind speed and direction and on the radar look direction. Wind speed and direction estimates can be affected quite strongly if signatures of internal waves in an image are not considered adequately. However, a detection of the characteristic wave patterns is relatively easy. Furthermore, internal waves are usually generated at certain locations and certain tidal phases, and they have typical propagation speeds. Thus, their occurrences in space and time can be predicted to some extent. For a discussion on properties of SAR signatures of oceanic internal waves under different conditions, see [15].
- Underwater bathymetric features in shallow waters with strong tidal currents, such as occurs in the North Sea, can cause strong NRCS variations via a modulation of the tidal flow and a surface roughness modulation by wave-current interaction. The spatial scales of the signatures are on the order of tens of meters to kilometers; the strength of the modulation can be on the order of a few dB. An example is shown in Figure 27 (b). Since the bathymetry is usually quasi-stationary and the tidal currents are predictable, it is relatively easy to detect signatures of bathymetric features in SAR imagery and eliminate them for wind retrieval purposes.
- Natural and man-made surface films and oil spills cause a strong damping of the ocean surface roughness and appear as dark areas in SAR images (low NRCS). While man-made oil spills are usually isolated features whose SAR signatures can be detected quite easily, natural surface films can cover large areas of the water surface quite homogeneously and make them look like areas of very low wind speed. An example is shown in Figure 27 (c). To distinguish between effects of surface films and low wind speeds, one can try to look for characteristic patterns (e.g., ship wakes or eddy patterns in surface films) or use plausibility criteria based on the dimensions and shapes of dark areas or the probability of film coverage and low wind speeds in the region. In this context one should know occurrences of low wind speeds and natural surface films are not independent of each other, since the formation of surface films will only take place in relatively calm conditions.
- Rain over the ocean can affect SAR images in multiple ways: while the downdraft winds often associated with rain cells will cause an increase of the NRCS [16] which is roughly consistent with wind scatterometer models, the rain itself modulates the surface wave spectrum in complex ways, leading to energy increases and decreases in different wavelength regimes. Furthermore, a damping of the microwave signal by rain in the air can occur. Altogether, this can result in quite different radar signatures at different radar frequencies and polarizations, as discussed, for example, by [17] Figure 27 (d) shows an example from ERS SAR.]
- Ships or fabricated structures at sea

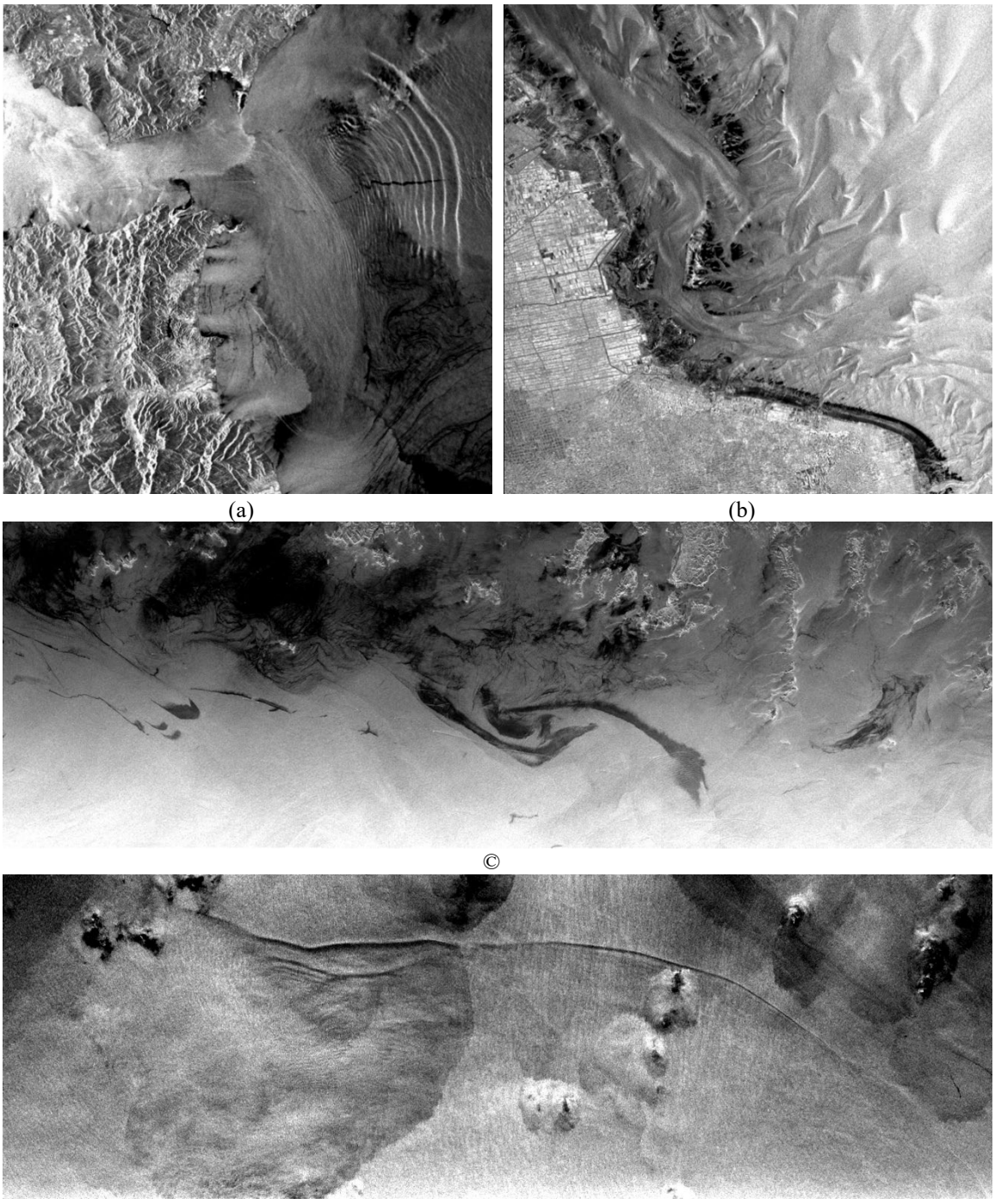

(a) (b)

©

(d)

Figure 27: Examples of ERS SAR images showing pronounced signatures of features which are not related to wind phenomena: (a) oceanic internal waves, oil spill, and natural surface films at the Strait of Gibraltar, Mediterranean Sea; (b) underwater bottom topography in Chinese coastal waters; (c) natural surface films and oil spills in Chinese coastal waters; (d) rain cells, fronts, and oceanic internal waves in the South China Sea. Swath width is 100 km; scene lengths are 100 km (a,b) and 300 km (c,d).

3.10.5.2 Algorithm accuracy

TBD

3.11 ComputeSeaStateBiasCorrection

3.11.1 Purpose

Compute sea state bias (SSB) correction from wind speed, SWH and optionally the mean wave period.

3.11.2 Input Data

Description	Source [x]: WINDWAVE or EXPERT
SSH at 2km posting, 2km resolution	*AverageDownTo2km* (this document, 3.8)
SWH from KaRin, at 2km posting, 2km resolution	L2B_[x]::swh_karin
quality flag for SWH from KaRIn.	L2B_[x]::swh_karin_qual
SWH from model, at 2km posting, 2km resolution	L2B_[x]::swh_model
wind speed from KaRIn	L2B_[x]::wind_speed_karin_2
quality flag for sigma0 from KaRIn	L2B_[x]::sig0_karin_qual
u component of model wind	L2B_[x]::wind_speed_model_u
v component of model wind	L2B_[x]::wind_speed_model_v
SSB correction tables	auxiliary and ancillary data
Mean sea surface wave direction from the Meteo France Wave Model (MF-WAM)	L2B_[x]::mean_wave_direction
Sea surface wind wave mean period from the second moment of the wave model spectral density from the Meteo France Wave Model (MF-WAM)	L2B_[x]::mean_wave_period_t02

3.11.3 Output Data

Description	Output data product (if exists)
SWH used in sea state bias correction	L2B_EXPERT::swh_ssb_cor_source_2
Wind used in sea state bias correction	L2B_EXPERT::wind_speed_ssb_cor_source_2
Sea state bias correction	L2B_EXPERT::sea_state_bias_cor_2
Fully corrected sea surface height measured by KaRIn.	L2B_EXPERT::ssh_karin_2 L2B_BASIC::ssh_karin_2

3.11.4 Mathematical Statement

For each sample

1. Get the SWH at the sample location
   - If the quality flag of SWH from KaRin is good; select the SWH from KaRIn.
   - If not; select the SWH from model [MF-WAM].
   - Store the selected value
2. Get the wind speed (U) at the sample location
   - If the quality flag of Sig0 from KaRin is good; select the wind speed from KaRIn.
   - If not; compute the wind speed from model

$$U = \sqrt{\text{wind\_speed\_model\_u}^2 + \text{wind\_speed\_model\_c}^2}$$

3. Perform a bilinear interpolation in the SSB correction table (see Appendix F)

$$\text{SSB\_cor}[i,j] = \text{table}(\text{SWH}[i,j], U[i,j])$$

   Store the interpolated value.
4. Compute the fully corrected sea surface height

$$\text{ssh\_karin\_2}[i,j] = \text{SSH}[i,j] + \text{SSB\_cor}[i,j]$$

   Store the value.

3.11.5 Accuracy

3.11.5.1 Algorithm versus geophysical truth

The potential inaccuracies in the SWH estimates propagate in the SSB. We foresee two main limitations of the SSB correction. First, assuming that the SWH parameter used for SSB estimation is equivalent to the one derived from the Jason-class altimeter (see section 3.9.5.1), [18] shows that , the SSB solution is unable to correct wavelengths smaller than 40-80 km (global average). This was due to the noise of altimetry-derived SWH. The second limitation is the use of nadir or near-nadir SWH inputs, which does not perfectly correct the far-range SSH. This is due to the mis-location between the sub-satellite point and far-range KaRIN pixels, which can be as large as 50 to 60 km (nadir to far-range pixels): in other words, a simple SSB algorithm using nadir or near-range SWH may not properly correct wave-induced effects for scales smaller than 40 to 80 km. Only the larger scales of the SSB would be corrected, especially in the outer edges of the swath.

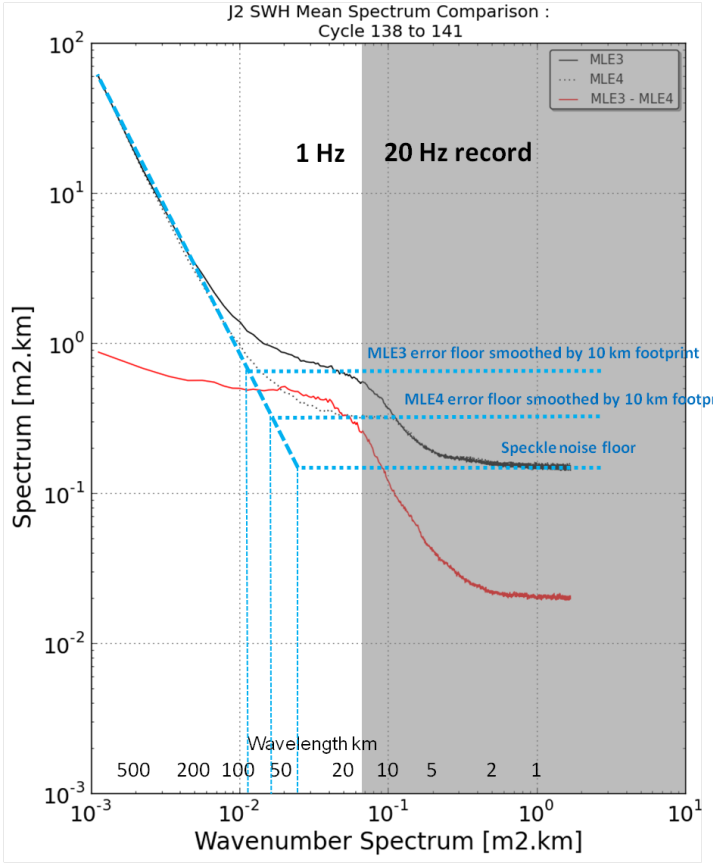

Figure 28: Global mean PSD of the SWH from Jason-2 estimated with MLE3 and MLE4 retrackers (from [18]). The blue lines illustrate the small-scales noise floor: speckle noise, MLE3 retracker estimation noise, and MLE4 retracker estimation noise. On average SWH observability (SNR=1) is limited to scales larger than 40 to 80 km.

3.11.5.2 Algorithm accuracy

The nominal SSB correction does not consider the cross-track position of the sample. The loss in accuracy implied by this hypothesis is currently under examination in the on-going activities on the sources of SSB. The SSB algorithm makes uses of an empirically generated table that requires tuning after launch. It accounts for coupling between sigma-0 and SSH that are not part of our raw echo simulations. For this reason, estimates of SSB error are TBD.

3.12 ComputeGeophysicalCorrections

3.12.1 Purpose

Compute tidal and other geophysical correction from models.

3.12.2 Input Data

Description	Source
time at 2km posting	L2B_EXPERT::time
latitude at 2km posting	L2B_EXPERT::latitude
longitude at 2km posting	L2B_EXPERT::longitude

3.12.3 Output Data

Description	Output data product (if exists)
Applied amplitude correction in Sig0 estimation in *ComputeSigma0* at fixed grid samples	
Applied delays correction in *SimulatePhaseBias* at fixed grid samples	
Mean Sea Surface from model 1 at fixed grid samples [CNES/CLS] Mean Sea Surface from model 2 at fixed grid samples [DTU]	L2B_EXPERT::mean_sea_surface_cnescls L2B_EXPERT::mean_sea_surface_dtu
Mean Sea Surface from model 1 uncertainty at fixed grid samples [CNES/CLS] Mean Sea Surface from model 2 uncertainty at fixed grid samples [DTU]	L2B_EXPERT::mean_sea_surface_cnescls_uncert L2B_EXPERT::mean_sea_surface_dtu_uncert
Solid Earth tide height at fixed grid samples [Cartwright et al]	L2B_EXPERT::solid_earth_tide
Geocentric load tide height from model 1 at fixed grid samples [LEGOS/CNES] Geocentric load tide height from model 2 at fixed grid samples [GSFC]	L2B_EXPERT::load_tide_fes L2B_EXPERT::load_tide_got
Ocean tide height from model 1 at fixed grid samples [LEGOS/CNES] Ocean tide height from model 2 at fixed grid samples [GSFC] (includes sum of ocean and load tide)	L2B_EXPERT::ocean_tide_fes L2B_EXPERT::ocean_tide_got
Model for sea surface height displacement from the equilibrium long-period ocean tides at fixed grid samples	L2B_EXPERT::ocean_tide_eq
Non-equilibrium long-period ocean tide height. [LEGOS/CNES]	L2B_EXPERT::ocean_tide_non_eq
Geocentric pole tide height (includes the sum of body, ocean, and load pole tide) at fixed grid samples [Desai et al]	L2B_EXPERT::pole_tide
Dynamic atmospheric correction at fixed grid samples [LEGOS/CNES/CLS]	L2B_EXPERT::dac
Coherent internal tide at fixed grid samples [Zaron] Coherent internal tide (alternative model) at fixed grid samples	L2B_EXPERT::internal_tide_hret L2B_EXPERT::internal_tide_sol2
Model for mean dynamic topography above the geoid at fixed grid samples [CNES/CLS]	L2B_EXPERT::mean_dynamic_topography
Accuracy or uncertainty of the mean dynamic topography at fixed grid samples [CNES/CLS]	L2B_EXPERT::mean_dynamic_topography_uncert

Ocean depth or land elevation above reference ellipsoid. Ocean depth (bathymetry) at fixed grid samples [ESA]	L2B_EXPERT::depth_or_elevation
Model of the static inverse barometer effect on SSH at fixed grid samples	L2B_EXPERT::inv_bar_cor
Equivalent vertical correction due to dry troposphere delay [ECMWF].	L2B_EXPERT::model_dry_tropo_cor
Equivalent vertical correction due to wet troposphere delay from weather model data [ECMWF]	L2B_EXPERT::model_wet_tropo_cor
Equivalent vertical correction due to ionosphere delay. [JPL]	L2B_EXPERT::iono_cor_gim_ka
Rain rate from weather model. [ECMWF]	L2B_EXPERT::rain_rate
Concentration of sea ice from model. [EUMETSAT]	L2B_EXPERT::ice_conc
Dynamic ice flag [EUMETSAT]	L2B_EXPERT::dynamic_ice_flag
7-state surface type classification [MODIS/ GlobCover]	L2B_EXPERT::ancillary_surface_classification_flag

3.12.4 Mathematical Statement

The mathematical statements can be found in the GECO documentation [11]

3.12.5 Accuracy

TBD

3.13 ComputeSeaSurfaceHeightAnomaly

3.13.1 Purpose

Apply correction to SSH to compute SSH anomaly.

3.13.2 Input Data

Description	Source
SSB corrected Sea Surface Height	L2B_BASIC::ssh_karin_2
Sea Surface Height uncertainty	L2B_BASIC::ssh_karin_uncert
Mean Sea Surface from model 1	L2B_EXPERT::mean_sea_surface_sol1
Solid Earth tide height	L2B_EXPERT::solid_earth_tide
Ocean tide height from model 1	L2B_EXPERT::ocean_tide_sol1
Geocentric pole tide height	L2B_EXPERT::pole_tide
Dynamic athmospheric correction	L2B_EXPERT::dac

3.13.3 Output Data

Description	Output data product (if exists) [x]: SSH or EXPERT
Sea Surface Height Anomaly	L2B_[x]::ssha_karin_2
Sea Surface Height Anomaly quality flag	L2B_[x]::ssha_karin_qual_2

3.13.4 Mathematical Statement

The SSHA is obtained by using models to subtract the contribution of the mean sea surface, tides (solid Earth, ocean, load, and pole tides), the high frequency response to atmospheric forcing from the SSH measurement. The Sea Surface Height anomaly is computed using the equation below

$$\text{ssha\_karin\_2} = \text{ssh\_karin\_2} - \text{mean\_sea\_surface\_sol1} - \text{solid\_earth\_tide} - \text{ocean\_tide\_sol1} - \text{pole\_tide} - \text{dac}$$

3.13.5 Accuracy

N/A

3.14 ComputeAndApplyRadiometerCorrections

3.14.1 Purpose

Compute additional version of SSH and SSH anomaly where the media delays corrections from a weather model applied during L1B processing are replaced with radiometer media delays.

3.14.2 Input Data

Description	Source
SSH at 2km posting, 2km resolution	L2B_BASICL2B_EXPERT:::ssh_karin_2
NRCS at 2km posting, 2km resolution	L2B_EXPERT::sig0_karin_2
Applied amplitude correction in Sig0 estimation in *ComputeSigma0* at 2km posting, 2km resolution	L2B_EXPERT::sig0_cor_atmos_model
Applied wet troposphere delays correction in *SimulatePhaseBias* at 2km posting, 2km resolution	L2B_EXPERT::model_wet_trop_cor
SSB corrections at 2km posting, 2km resolution	L2B_EXPERT::sea_state_bias_cor_2
latitude at 2km posting	L2B_EXPERT::latitude
longitude at 2km posting	L2B_EXPERT::longitude
Equivalent vertical wet tropospheric path delay correction from radiometer measurements (rad_wet_tropo_cor)	Radiometer
Amplitude correction in Sig0 from radiometer measurements (sig0_cor_atmos_rad)	Radiometer

3.14.3 Output Data

Description	Output data product (if exists)
Corrected SSH at 2km posting, 2km resolution	L2B_EXPERT:::ssh_karin L2B_BASIC:::ssh_karin
Corrected wind speed at 2km posting, 2km resolution	L2B_EXPERT:::wind_speed_karin
Corrected NRCS at 2km posting, 2km resolution	L2B_EXPERT:::sig0_karin
Corrected SSB corrections at 2km posting, 2km resolution	L2B_EXPERT:::sea_state_bias_cor
Corrected SSHA at 2km posting, 2km resolution	L2B_EXPERT:::ssha_karin L2B_BASIC:::ssha_karin

3.14.4 Mathematical Statement

1. Get sig0_karin using

$$\text{sig0\_karin} = \text{sig0\_karin\_2} \times \text{sig0\_cor\_atmos\_rad} \,/\, \text{sig0\_cor\_atmos\_model}$$

2. Recompute the wind speed using sig0_karin instead of sig0_karin_2 in 3.10 to get wind_speed_karin.

3. Recompute the sea state bias using wind_speed_karin instead of wind_speed_karin_2 in 3.11 to get sea_state_bias_cor

4. Get ssh_karin using

$$\begin{aligned}\text{ssh\_karin} = \text{ssh\_karin\_2} + \text{model\_wet\_tropo\_cor} - \text{rad\_wet\_tropo\_cor} \\ + \text{sea\_state\_bias\_cor\_2} - \text{sea\_state\_bias\_cor}\end{aligned}$$

Recompute the sea surface height anomaly ssh_karin instead of ssh_karin_2 in 3.13 to get ssha_karin_2.

3.14.5 Accuracy

A conservative approach would translate the media-delay into slant-range corrections thus leading to a reprocessing from the *PhaseToHeight* step. Considering that (model_wet_tropo_cor – rad_wet_tropo_cor) are small quantities, the media delay correction can be applied directly to the heights at the cost of very low error. The error is less than 1% of the (model_wet_tropo_cor – rad_wet_tropo_cor) value. Figure 29 shows An error in the SSH of 1mm for a "10 cm model change" (i.e. (model_wet_tropo_cor – rad_wet_tropo_cor) = 10cm).

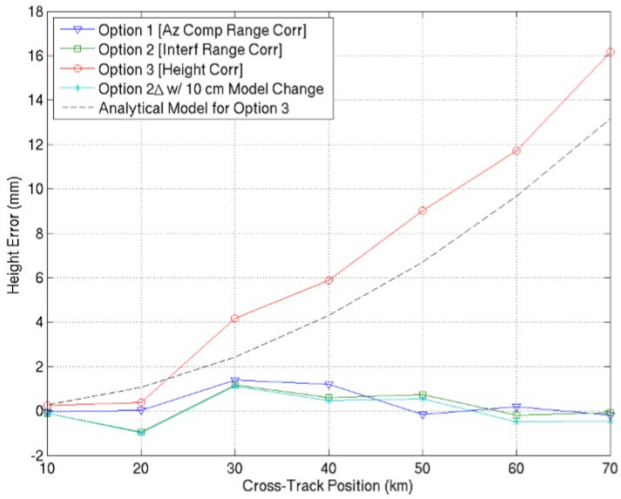

Figure 29: Plot of simulated height error vs. cross-track position for different correction approaches : this ATBD implements Option 2Δ.

3.15 ComputeCrossCalibrationCorrection

3.15.1 Purpose

Convert Xover info into the proper format and representation to provide a correction to minimize systematic errors (timing, range bias, residual roll, phase error, baseline length error) using empirical methods.

3.15.2 Input Data

Description	Source
Distance from center of swath	L2B_EXPERT::cross_track_distance

3.15.3 Output Data

Description
Height correction *height_cor_xover* to be added to *ssh_karin, ssh_karin_2, ssha_karin*, and *ssha_karin_2. The step of actually adding the height_cor_xover value to those quantities is left for the user of the data to perform.*

3.15.4 Mathematical Statement

The mathematical statements can be found in [19].

3.15.5 Accuracy

N/A

4 References

[1] B. Stiles and N. Steunou, "Level 2 KaRIn Low Rate Sea Surface Height Product," D-56407, Jet Propulsion Laboratory, Pasadena, 2023.

[2] "SWOT Science Requirements Document," D-61923, Jet Propulsion Laboratory, Pasadena, 2018.

[3] C. Chen, "Auxiliary Data Description - Reference Orbit Track," D-105500, Jet Propulsion Laboratory, Pasadena, 2022.

[4] C. Chen, "SWOT Science Data Product Granule Boundary and Sampling Definition," D-102104, Jet Propulsion Laboratory, Pasadena, 2022.

[5] B. W. Stiles, "SWOT Level 1B KaRIn Low Rate Interferogram Algorithm Theoretical Basis Document," D-105501, Jet Propulsion Laboratory, Pasadena, 2023.

[6] P. A. Rosen, S. Hensley, I. R. Joughin, F. K. Li, S. N. Madsen, E. Rodriguez and R. M. Goldstein, "Synthetic aperture radar interferometry - invited paper," *Proceedings of the IEEE,* vol. 88, no. 3, p. 333–382, 2000.

[7] A. Bohe, "A complete theoretical derivation of the level of random heigh noise in interferometric unfocued SAR swath altimetry.," *IEEE Transactions on Geoscience and Remote Sensing,* doi:10.1109/TGRS.2023.3290850.

[8] C. W. Chen, "A Spectral Model for Multilook InSAR Phase Noise Due to Geometric Decorrelation," *IEEE Transactions on Geoscience and Remote Sensing,* vol. 61, pp. 1-11, doi:10.1109/TGRS.2023.3272296, 2023.

[9] D. Esteban-Fernandez, "SWOT Mission Performance and Error Budget," D-79084, Jet Propulsion Laboratory, Pasadena, 2017.

[10] E. Peral, E. Rodriguez and D. Esteban-Fernández, " Impact of Surface Waves on SWOT's Projected Ocean Accuracy.," *Remote Sensing.,* vol. 7, pp. 14509-14529, 2015.

[11] G. Bracher, "Functions definition and specification of the Geophysical/Environmental Correction and Orbitography Module," CLS-GECO-1-09, CNES/CLS, Toulouse, 2023.

[12] F. Ardhuin, A. Roland, F. Dumas, A.-C. Bennis, A. Sentchev, P. Forget, J. Wolf, F. Girard, P. Osuna and M. Benoit., "Numerical Wave Modeling in Conditions with Strong Currents: Dissipation, Refraction, and Relative Wind," *Journal Of Geophysical Oceanography,* vol. 42, no. 12, p. 2101, 2012.

[13] F. Ardhuin, S. T. Gille, D. Menemenlis, C. B. Rocha, N. Rascle, B. Chapron, J. Gula and J. Molemaker, "Small-scale open ocean currents have large effects on wind wave heights," *J. Geophys. Res. Oceans,* vol. 122, p. 4500– 4517, 2017.

[14] S. Ufermann and R. Romeiser, "A new interpretation of multifrequency/multipolarization radar signatures of the Gulf Stream front," *J. Geophys. Res.,* vol. 104, pp. 25,697-25,706, 1999.

[15] P. Brandt, R. Romeiser and A. Rubino, "On the determination of characteristics of the interior ocean dynamics from radar signatures of internal solitary wave," *J. Geophys. Res.,* vol. 104, p. 1999, 30,039-30,045.

[16] W. Alpers, B. Zhang, A. Mouche, K. Zeng and K. P. Chan, "Rain footprints on C-band synthetic aperture radar images of the ocean - Revisited," *Remote Sensing of Environment,* vol. 187, pp. 169-185, 2016.

[17] C. Melsheimer, W. Alpers and M. Gade, "Investigation of multifrequency / multipolarization radar signatures of rain cells derived from SIR-C/X-SAR data," *J. Geophys. Res.,* vol. 103, pp. 18,867-18,884, 1998.

[18] G. Dibarboure, F. Boy, J. D. Desjonqueres, S. Labroue, Y. Lasne, N. Picot, J. C. Poisson and P. .Thibaut, "Investigating Short-Wavelength Correlated Errors on Low-Resolution Mode Altimetry.," *Journal of Atmospheric and Ocean Technology ,* vol. 31, no. 6, p. 1337–62, 2014.

[19] C. Garcia, "SWOT KaRIn Crossover Calibration Product Description," SWOT-TN-CDM-0679-CNES, CNES, Toulouse, 2022.

[20] Y. Quilfen, B. Chapron, T. Elfouhaily, K. Katsaros and J. Tournadre, "Observation of tropical cyclones by high-resolution scatterometry," *J. Geophys. Res,* vol. 103, pp. 7767-7786, 1998.

[21] A. Bentamy, P. Queffeulou, Y. Quilfen and K. Katsaros, "Ocean surface wind fields estimated from satellite active and passive microwave instruments," *IEEE Trans. Geosci. Remote Sensing,* vol. 37, pp. 2469-2486, 1999.

[22] P. Gaspar, S. Labroue, F. Ogor, G. Lafitte, L. Marchal and M. Rafanel, "Improving non-parametric estimates of the sea state bias in radar altimetry measurements of sea level," *J. Atmos. Oceanic Technol,* vol. 19, p. 1690-1707, 2002.

[23] D. Vandemark, N. Tran, B. B. D. B. Chapron and P. Gaspar, "Direct estimation of sea state impacts on radar altimeter sea level measurements," *Geophys. Res. Lett,* vol. 29, no. 24, p. 2148, 2002.

Appendix A. **Acronyms**

AD	Applicable Document
AMR	Advanced Microwave Radiometer
API	Application Interface
ATBD	Algorithm Theoretical Basis Document
CNES	Centre National d'Études Spatiales
ECEF	Earth Centered, Earth Fixed
ECMWF	European Centre for Medium-Range Weather Forecasts
GMF	Geophysical Model Function
GPM	Global Precipitation Measurement
HPA	High-Power Amplifier
JPL	Jet Propulsion Laboratory
KMSF	KaRIn Metering Structure Frame
MLE	Maximum Likelihood Estimator
MSS	Mean Sea Surface
NASA	National Aeronautics and Space Administration
NRCS	Normalized Radar Cross Section
OBP	On-Board Processor
PGE	Product Generation Executable
PTR	Point Target Response
RD	Reference Document
s/c	spacecraft
SAS	Science Algorithm Software
SDS	Science Data System
std	standard deviation
SSB	Sea State Bias
SSH	Sea Surface Heights
SSHA	Sea Surface Height Anomaly
SWH	Surface Wave Heights
SWOT	Surface Water Ocean Topography
TBC	To Be Confirmed
TBD	To Be Determined

Appendix B. **Grids**

B.1. Grid Types

All the grids used in L2_LR_SSH are contextualized in an overview of the processing:

1. For each Doppler beam formed by the OBP, the sample locations in the L1B_LR_INTF product are the intersections of the beam vectors with a reference surface used during the L1B_LR processing [5, 5] (defined in *ConstructRefSurf*, used in *SimulatePhaseBias*). In this context, the beam vector is defined such that it represents the weighted average response to the reference surface given the antenna pattern and the point-target response. These sample locations form the **beams native grids**, which have a spatial posting of approximately 250 m in both the cross-track and along-track directions
2. *PhaseToHeights*: the KaRIn differential interferometric phase measurements are converted into absolute 3D[3] positions, by adding the relative position shift computed from the phase to the **beams native grids locations.** On the ellipsoid surface, the absolute positions form an irregular grid of estimated locations ((lon, lat), for each beam) where the estimated heights (SSH) are located.
3. *InterpolateToCentralBeamGrid*: the KaRIn measurements (both the estimated locations and the estimated heights) from beams other than the central beam are interpolated to the **central beam** (#5) **native grid**.
4. *CombineBeams*: Once the measurements from the different beams are presented on a common grid (the central beam native grid), the KaRIn measurements (both the estimated locations and the estimated heights) from the different beams are combined together via weighted averaging at each sample location. These beam-combined measurements on the **central beam native grid** are provided in the unsmoothed file data product.
5. In order to reduce noise and to facilitate the interpretation of the data, the unsmoothed data are further
    a. *InterpolateToFixedGrid*: resampled to a **250 m** geographically **fixed grid**.
    b. *AverageDownTo2km*: spatially smoothed to a **2 km** geographically **fixed grid**.

    MakeFixedGrid: The fixed grid is swath aligned, with respect to the reference nadir track. The along-track locations are reference nadir track locations, spaced at 125 m along the ellipsoid. The cross-track sample locations are then tied to the along-track sample locations at nadir and defined on the ellipsoid such that their projections onto an approximating sphere are evenly spaced at 125 m.
    The **250 m fixed grid** uses one point over two of the 125 m fixed grid and the **2 km fixed grid** uses over one point over sixteen of the 125 m fixed grid.

The ‘Illustration of sampling grids’ figure of [1] is reproduced hereafter.

[3] We use the term « 3D position” to refer to locations expressed in (x,y,z) ECEF coordinates

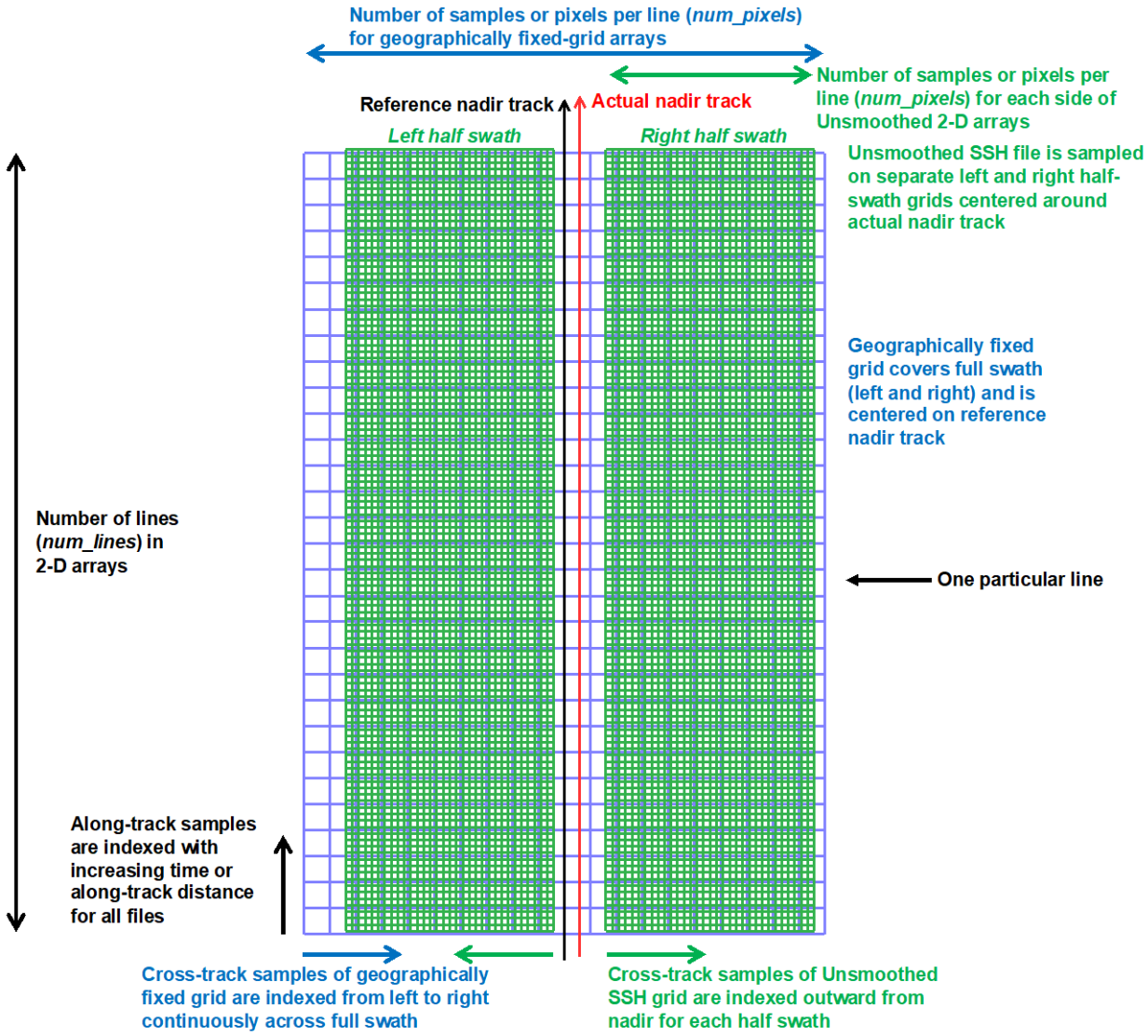

Figure 30. Illustration of sampling grids

B.2. Interpolation Grids

Given an irregular source grid, $\text{grid}_{\text{from}} \equiv (\text{lat}_{\text{from}}, \text{lon}_{\text{from}})$, and an irregular target grid, $\text{grid}_{\text{to}} \equiv (\text{lat}_{\text{to}}, \text{lon}_{\text{to}})$. The source and target grids have respective shapes (N_X^{pix}, N_X^{lin}) and (N_Y^{pix}, N_Y^{lin}).

We want the interpolation grids $\text{pixels}_{\text{from}}$ and $\text{lines}_{\text{from}}$ (of shape (N_Y^{pix}, N_Y^{lin})) such that

$$\text{lat}_{\text{to}}[i_Y, j_Y] = \text{bilinear}(\text{pixels}_{\text{from}}[i_Y, j_Y], \text{lines}_{\text{from}}[i_Y, j_Y], \text{lat}_{\text{from}})$$
$$\text{lon}_{\text{to}}[i_Y, j_Y] = \text{bilinear}(\text{pixels}_{\text{from}}[i_Y, j_Y], \text{lines}_{\text{from}}[i_Y, j_Y], \text{lon}_{\text{from}})$$

For all pixels of the target grid $i_Y \in [0, N_Y^{pix} - 1], j_Y \in [0, N_Y^{line} - 1]$, $\text{pixels}_{\text{from}}[i_Y, j_Y] = i$ and $\text{lines}_{\text{from}}[i_Y, j_Y] = j$ are found through an iterative process.

The tolerance ε is set to $1.e^{-10}$ radians which translates in a horizontal distance inferior to 1mm.

Initialization of the iterative process:

The real coordinates are first set in the middle of the source grid

$$i = \frac{N_X^{pix}}{2}, \quad j = \frac{N_X^{lin}}{2}$$

The distances to the target point are then

$$\Delta_{lon} = \text{lon}_{\text{to}}[i_Y, j_Y] - \text{bilinear}(i, j, \text{lon}_{\text{from}})$$
$$\Delta_{lat} = \text{lat}_{\text{to}}[i_Y, j_Y] - \text{bilinear}(i, j, \text{lat}_{\text{from}})$$

and we constrain Δ_{lon} in $[-\pi, \pi[$

The iterative process repeats while ($|\Delta_{\text{lat}}| > \varepsilon$ or $|\Delta_{\text{lon}}| > \varepsilon$)

We progress toward the target point $(\text{lat}_{\text{to}}[i_Y, j_Y], \text{lon}_{\text{to}}[i_Y, j_Y])$ with

$$i = i + \Delta_i$$
$$j = j + \Delta_j$$

where (Δ_i, Δ_j) are the distances to the target point in number of columns and rows, respectively. These are real numbers and are computed using the distances $(\Delta_{lon}, \Delta_{lat})$ and the grid spacing at the target sample closest to the current location; we recall that the target grid might be irregular and then the spacing is not constant inside the grid. The procedure for computing (Δ_i, Δ_j) is explained below

The spacing at the closest sample of coordinates (i_X, j_X) with $(i_X = \text{round}(i), j_X = \text{round}(j))$ is set with
the estimated horizontal spacing

$$d_{lon}^i = \text{lon}_{\text{from}}[i_X + 1, j_X] - \text{lon}_{\text{from}}[i_X, j_X]$$
$$d_{lat}^i = \text{lat}_{\text{from}}[i_X + 1, j_X] - \text{lat}_{\text{from}}[i_X, j_X]$$

and the estimated horizontal spacing

$$d_{lon}^j = \text{lon}_{\text{from}}[i_X, j_X + 1] - \text{lon}_{\text{from}}[i_X, j_X]$$
$$d_{lat}^j = \text{lat}_{\text{from}}[i_X, j_X + 1] - \text{lat}_{\text{from}}[i_X, j_X]$$

From

$$d_{lon}^i \, \Delta_i + d_{lon}^j \, \Delta_j = \Delta_{lon}$$
$$d_{lat}^i \, \Delta_i + d_{lat}^j \, \Delta_j = \Delta_{lat}$$

we can set

$$i = i + \Delta_i = i + \frac{\Delta_{lon}\, d^j_{lat} - \Delta_{lat}\, d^j_{lon}}{d^i_{lon}\, d^j_{lat} - d^i_{lat}\, d^j_{lon}}$$

$$j = j + \Delta_j = j + \frac{\Delta_{lat} - \Delta_i\, d^i_{lat}}{d^j_{lat}}$$

The new distances are

$$\Delta_{lat} = \mathrm{lat_{to}}[i_Y, j_Y] - \mathrm{bilinear}(i, j, \mathrm{lat_{from}})$$
$$\Delta_{lon} = \mathrm{lon_{to}}[i_Y, j_Y] - \mathrm{bilinear}(i, j, \mathrm{lon_{from}})$$

and we constrain Δ_{lon} in $[-\pi, \pi)$

When the iterative process ends
we set

$$\mathrm{pixels_{from}}[i_Y, j_Y] = i$$
$$\mathrm{lines_{from}}[i_Y, j_Y] = j$$

and compute $\mathrm{lat_{to}}[i_Y, j_Y]$ and $\mathrm{lon_{to}}[i_Y, j_Y]$ using a bilinear interpolation as stated at the beginning of this section.

Note that the iterative process breaks anytime if $i \notin [0, N_X^{pix} - 1]$ or $j \notin [0, N_X^{lin} - 1]$ or the maximum number of iterations is reached. If so, we set

$$\mathrm{lat_{to}}[i_Y, j_Y] = -1$$
$$\mathrm{lon_{to}}[i_Y, j_Y] = -1$$

Appendix C. Interpolations

C.1. linear interpolation

Given X, the 1D data to interpolate and Y, the 1D interpolated data of respective sizes (N_X^{lin}) and (N_Y^{lin}).

The integer coordinates in the Y grid

$$(\{j_Y \in [0, N_Y^{lin} - 1]\})$$

have corresponding real coordinates $(\{j\})$ in X given by the interpolation grids (see B.2)

$$j = \text{lines}_{\text{from}}[j_Y]$$

C.1.1. Parametrization

No parametrization is needed

C.1.2. Interpolate at (i, j)

We check whether enough samples around j exist to perform the interpolation. If not, the interpolated value is set to NaN

$$\text{int}(j) \notin [0, N_X^{lin} - 2] \rightarrow Y[j_Y] = \text{NaN}$$

where int(.) strips off the number decimals.

If enough samples exist

$$j_0 \stackrel{\text{def}}{=} \text{int}(j)$$
$$j_1 \stackrel{\text{def}}{=} \text{int}(j) + 1$$

$$Y[j_Y] = (j_1 - j)X[j_0] + (j - j_0)X[j_j]$$

C.2. Sinc_lineD interpolation

Given X, the 2D data to interpolate and Y, the 2D interpolated data of respective shapes (N_X^{pix}, N_X^{lin}) and (N_Y^{pix}, N_Y^{lin}).

The integer coordinates in the Y grid

$$(\{i_Y \in [0, N_Y^{pix} - 1]\}, \{j_Y \in [0, N_Y^{lin} - 1]\})$$

have corresponding real coordinates $(\{i\}, \{j\})$ in X given by the interpolation grids (see B.2)

$$i = \text{pixels}_{\text{from}}[i_Y, j_Y]$$
$$j = \text{lines}_{\text{from}}[i_Y, j_Y]$$

C.2.1. Parametrization

For both the line and pixel directions

- SINC_BETA: β^{pix}, β^{lin} , (real ∈]0.,1.])
- SINC_DEC_FACTOR: d_f^{pix}, d_f^{lin} decimation factor (integer ≥ 1)
- SINC_REL_LENGTH: $L_{rel}^{pix}, L_{rel}^{lin}$ relative filter length (integer ≥ 1)

  For the weighting function
  - SINC_ENABLE_WEIGHTING
  - SINC_PEDESTAL: w_f^{pix}, w_f^{lin} pedestal height for weighting function (real ∈]0.,1.])

A Default configuration sets, for both pixel and line directions

SINC_BETA = 1.0
SINC_DEC_FACTOR = 1024
SINC_REL_LENGTH = 8
SINC_ENABLE_WEIGHTING = False

C.2.2. Construct tables

For both directions, $p \in \{pix, lin\}$

The interpolator length is set with

$$L^p = \text{int}\left(\frac{L_{rel}^p}{\beta^p} + 0.5\right)$$

where int(.) strips off the number decimals.

The total number of weighted sinc interpolator values N^p is set with

$$N^p = L^p \times d_f^p$$

The table of weighted sinc interpolator values prior to rearrangement

for $i \in [0, N^p - 1]$

$$\text{table}_{\text{scratch}}[i] = \text{sinc}\left(\left(i - \frac{N^p - 1}{2}\right)\frac{\beta^p}{d_f^p}\right)$$

if SINC_ENABLE_WEIGHTING

$$\text{table}_{\text{scratch}}[i] = \text{table}_{\text{scratch}}[i].\left[\frac{1 + w_f^p}{2} + \frac{1 - w_f^p}{2}\cos\left(\frac{2\pi}{N^p - 1}\left(i - \frac{N^p - 1}{2}\right)\right)\right]$$

We rearrange the coefficients in memory so that the values needed for a particular interpolation are contiguous.
for $j \in [0, d_f - 1]$, for $i \in [0, L-1]$

$$\text{table}^p[i + j.L] = \text{table}_{\text{scratch}}[j + i.d_f]$$

C.2.3. Interpolate at (i, j)

L^{pix} and L^{lin} are length of the filter kernel in number of pixels and lines, respectively.
We first check whether enough data samples around i and j exist to perform the interpolation. If not, the interpolated value is set to NaN

$$\text{int}\left(i + \frac{L^{pix}}{2}\right) \notin [\, L^{pix} - 1, N_X^{pix} - 1] \rightarrow Y[i_Y, j_Y] = \text{NaN}$$
$$\text{int}\left(j + \frac{L^{lin}}{2}\right) \notin [\, L^{lin} - 1, N_X^{lin} - 1] \rightarrow Y[i_Y, j_Y] = \text{NaN}$$

If the enough samples exist, each of the pixels that will be used in the pixel direction interpolation is in the list $\{k + \min_i\}$ where

$$k \in [0, L^{pix}]$$
$$\min_i = \text{int}\left(i + \frac{L^{pix}}{2}\right) - (L^{pix} - 1)$$

, we perform the interpolation in the lines direction.

$$m_0 = \text{int}\left(j + \frac{L^{lin}}{2}\right)$$
$$r_{frac} = j + \frac{L^{lin}}{2} - m_0$$
$$\text{offset}^{lin} = \text{int}(d_f^{lin}.r_{frac}).L^{lin}$$

$$\text{buf}[k] = \frac{\sum_{m=0}^{L^{lin}-1} \text{table}^{lin}[m + \text{offset}^{lin}].X[\min_i + k, m_0 - m]}{\sum_{m=0}^{L^{lin}-1} \text{table}^{lin}[m + \text{offset}^{lin}]}$$

> For the interpolation of flags, the previous equation is replaced with
>
> $$\text{buf}[k] = \bigvee_{m=0}^{L^{lin}-1} X[\min_i + k, m_0 - m]$$
>
> where ∨ is the Or Bitwise operator

Once the interpolation in the lines direction has been performed for all the pixels $\{k + \min_i\}$ we perform the interpolation in the pixels direction

$$n_0 = \text{int}\left((i - \min_i) + \frac{L^{pix}}{2}\right)$$

Note that because $\min_i = \text{int}\left(i + \frac{L^{pix}}{2}\right) - \left(L^{pix} - 1\right); n_0 = \left(L^{pix} - 1\right)$

$$r_{frac} = (i - \min_i) + \frac{L^{pix}}{2} - n_0$$

$$\text{offset}^{pix} = \text{int}\left(d_f^{pix} . r_{frac}\right) . L^{pix}$$

$$Y[i_Y, j_Y] = \frac{\sum_{n=0}^{L^{pix}-1} \text{table}^{pix}\left[n + \text{offset}^{pix}\right] . \text{buf}[n_0 - n]}{\sum_{n=0}^{L^{pix}-1} \text{table}^{pix}[n + \text{offset}^{pix}]}$$

For the interpolation of flags, the previous equation is replaced with

$$Y[i_Y, j_Y = \bigvee_{n=0}^{L^{pix}-1} \text{buf}[n_0 - n]$$

where ∨ is the Or Bitwise operator

Appendix D. SWH estimates standard deviation

The SWH estimator can be analytically set with the equation (see section 3.9.4)

$$\left.\frac{\partial \mathrm{cost}}{\partial \mathrm{swh}}\right|_{\widehat{\mathrm{SWH}}} = 0$$

with

$$\frac{\partial \mathrm{cost}}{\partial \mathrm{swh}} = \sum_{i=0}^{N^{pix}-1} \frac{\mathrm{swh}}{8\sigma_{vol}^2[i]} (\partial_h \varphi[i])^2 \exp\left(-\frac{1}{32}(\partial_h \varphi[i])^2 \mathrm{swh}^2\right)\left(\hat{C}_{\mathrm{vol}}[i] - \exp\left(-\frac{1}{32}(\partial_h \varphi[i])^2 \mathrm{swh}^2\right)\right)$$

The dependence in the line index, is omitted

We write the estimates as the sum of their means and a random variable

$$\hat{C}_{\mathrm{vol}}[i] = \langle \hat{C}_{\mathrm{vol}}[i] \rangle + X_i$$
$$\widehat{\mathrm{SWH}} = \langle \widehat{\mathrm{SWH}} \rangle + Y$$

We assume that the true significant wave height, SWH, is constant and that the estimator is unbiased $\langle \widehat{\mathrm{SWH}} \rangle = \mathrm{SWH}$.

$$\sum_{i=0}^{N^{pix}-1} \frac{(\partial_h \varphi[i])^2}{\sigma_{vol}^2[i]} \exp\left(-\frac{(\partial_h \varphi[i])^2}{32}(\mathrm{SWH}+Y)^2\right)\left(\exp\left(-\frac{(\partial_h \varphi[i])^2}{32}\mathrm{SWH}^2\right) + X_i - \exp\left(-\frac{(\partial_h \varphi[i])^2}{32}(\mathrm{SWH}+Y)^2\right)\right) = 0$$

The mean value of the sum is set using the law of the unconscious statistician. We make the hypothesis that Y and X_j are uncorrelated, and normally distributed with respective standard deviation σ_Y, σ_{X_J}. Then

$$\sum_{i=0}^{N^{pix}-1} \frac{(\partial_h \varphi[i])^2}{\sigma_{vol}^2[i]} \int \exp\left(-\frac{(\partial_h \varphi[i])^2}{32}(\mathrm{SWH}+Y)^2\right)\left(\exp\left(-\frac{(\partial_h \varphi[i])^2}{32}\mathrm{SWH}^2\right) + X_i - \exp\left(-\frac{(\partial_h \varphi[i])^2}{32}(\mathrm{SWH}+Y)^2\right)\right) \mathrm{pdf}(X_i)\,\mathrm{pdf}(Y)\,.\,\mathrm{d}X_i.\mathrm{d}Y = 0$$

Finally

$$\sum_{i=0}^{N^{pix}-1} \frac{(\partial_h \varphi[i])^2}{\sigma_{vol}^2[i]} \frac{1}{\sqrt{1+\frac{\sigma_Y^2(\partial_h \varphi[i])^2}{16}}} \exp\left(-\frac{(\partial_h \varphi[i])^2}{16}\mathrm{SWH}^2\left[1+\frac{\sigma_Y^2}{32\left(1+\frac{\sigma_Y^2(\partial_h \varphi[i])^2}{16}\right)}\right]\right) = 0$$

Appendix E. **Wind Estimates input model**

Option 1. Building GMF.

The GMF can be built on existing datasets, e.g., from the GPM mission. The figure below shows the Ka and Ku-band backscatter with respect to the incidence angle and at different wind conditions

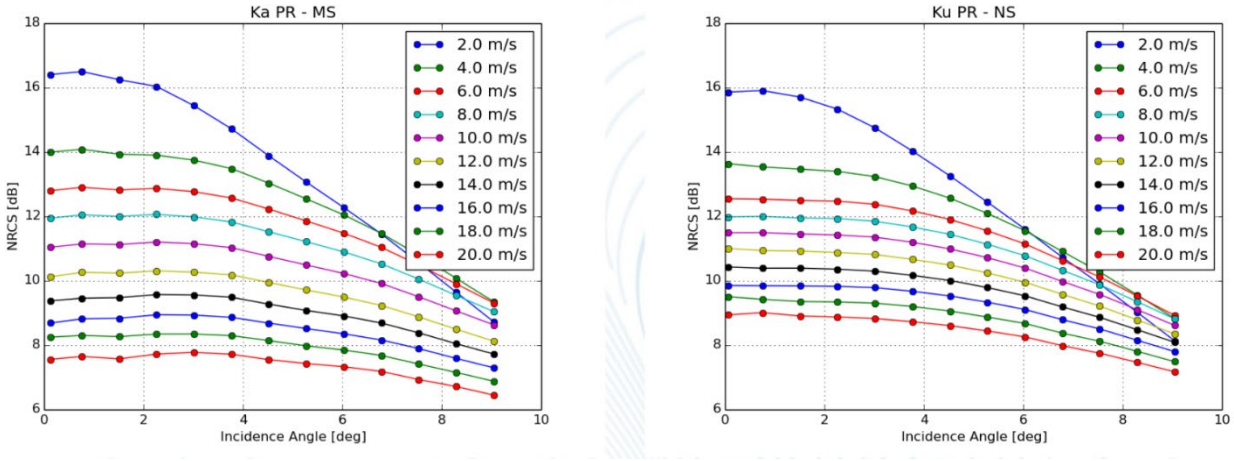

Figure 31: Ka and Ku backscatter given by GPM mission with respect to the incidence angle.

As illustrated in *Figure **32*** and *Figure **33***, significant wave height, wave steepness and, to a lesser extent, wind direction with respect to the radar look angle impact Ku-band backscatter. First results tend to show that these parameters also play an important role for in Ka-band backscatter at low incidence angles. Indeed, similar behaviors are found. The impact of significant wave height decreases when incidence angle and/or wind speed increases**.**

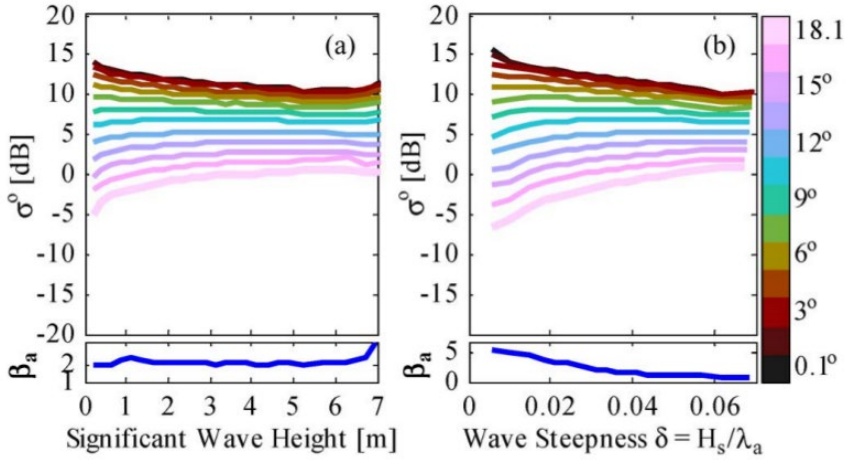

Figure 32: Ku backscatter. Mean values of binned $\tilde{\boldsymbol{\sigma}}^{\mathbf{0}}$ measured by Tropical Rainfall

Measuring Mission precipitation Radar as functions of (a) significant wave height (**SWH**) *and (b) wave steepness (**δ**) for different incidence angles. The subfigures show the average β over the same (a)* **SWH** *or (b)* ***δ****. Extracted from [R3].*

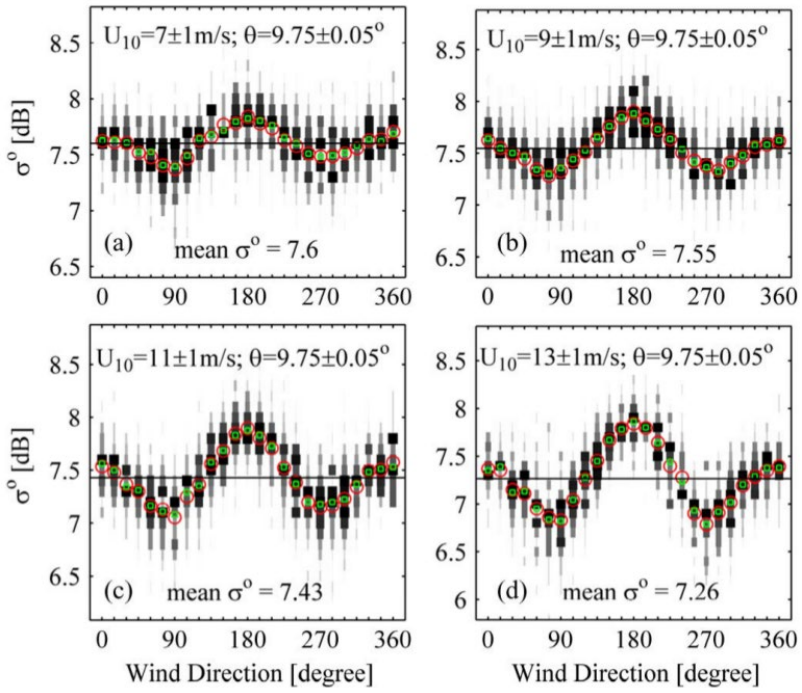

Figure 33: Box plot of $\tilde{\boldsymbol{\sigma}}^{\mathbf{0}}$ *measured by Tropical Rainfall Measuring Mission precipitation Radar in each 15° azimuthal interval. Widths and gray levels of boxes show the distribution of data. Mean and median are shown as red circles and green squares, respectively. Extracted from [R3].*

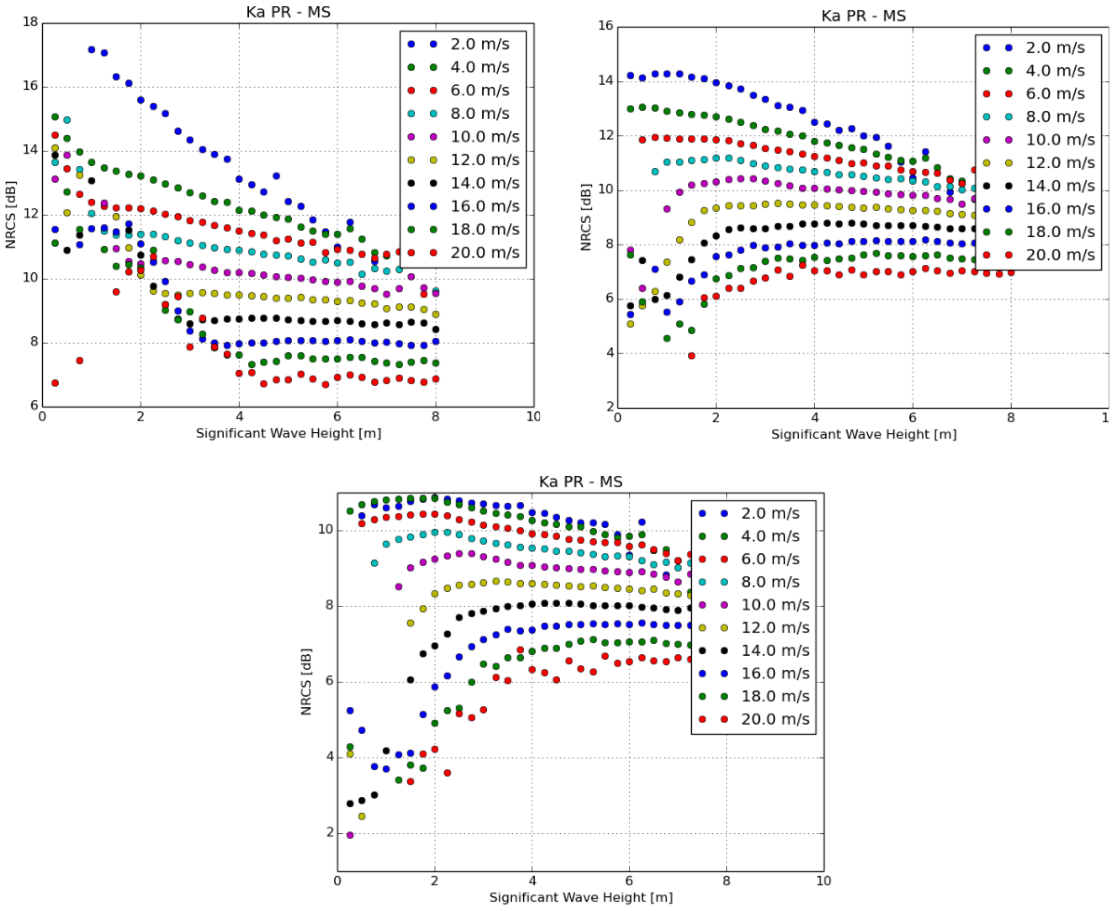

Figure 34: Ka backscatter measurements given by GPM instrument as a function of significant wave height (from WW3) for incidence angles of 0.75, 3.77 and 6.78°. Graphs provided as a courtesy of Alexis Mouche, from IFREMER.

Option 2.

In the Bayesian wind inversion, all the possible wind directions need to be considered to find the most likely wind vector solution. This precludes the indirect zero-crossing inversion. One needs to elaborate an inverse KaMOD providing the wind speed vector $\mathbf{u}$ as an analytic function of the vector $(\tilde{\sigma}^0, \theta, \text{SWH}, \ldots)$:

$$\mathbf{u} = \text{KaMOD}^{-1}(\theta, \mathbf{a}; \tilde{\sigma}^0)$$

The derivation of such function is feasible using neural network approach. As an example, such implementation has been studied, defined and realized for a number of CMOD scattering models (CMOD-IFR2 [20] and CMOD2-I3 [21]).

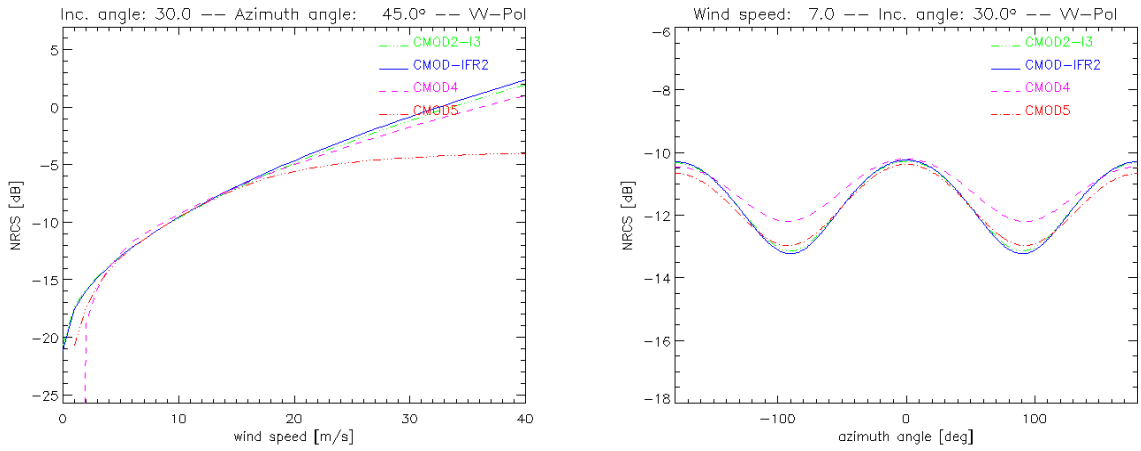

(a) (b)

Figure 35: Examples of CMOD functions giving NCRS values in dB. (a) NRCS vs. wind speed in m/s at an incidence angle of 30° and for wind blowing towards the instruments with an angle of 45° with respect to the radial direction. (b) NRCS vs. azimuth wind direction at an incidence angle of 30° and for wind speed of 7 m/s

Appendix F. SSB Correction table

The Sea State Bias (SSB) correction table is computed empirically with the non-parametric estimation technique based on kernel smoothing described in [22]. The solutions are derived from 10-day SSH differences (i.e. collinear analysis of repeat cycles of data from crossover differences). The non-parametric solution consists in a 2D grid (black curves in Figure 36). Each grid point has associated a local kernel (red ellipses in Figure 36, right) which size depends on the data density. The respective SSB value is determined by resolving a system of equations based on the data that lies within the kernel

Figure 36 shows two examples of SSB correction computation. The SSB correction value for a wind speed of 12m/s and a SWH of 7m is computed using all the data acquired at wind speed and SWH conditions that belong to an ellipse of axes (3m/s, 1,35m), centered at (12m/s, 7m). The ellipse kernel used to compute the correction at (8m/s, 2m) is smaller than the one used for the correction at (12m/s, 7m); this is because the data density is higher in the region near (8m/s, 2m). The left plot of Figure 36 shows the particular case of the kernels near (0m/s, 0m) where an ellipse shaped kernel cannot be defined.

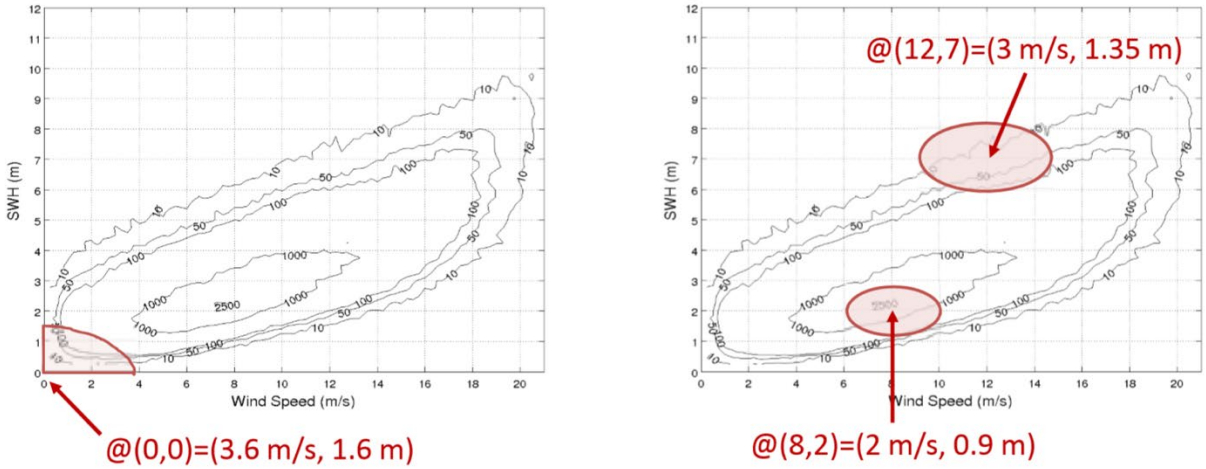

Figure 36: In black: SSB corrections table obtained by the non-parametric solution.
In red: the local kernels used for corrections estimation.

The use of the mean wave period (Tm, from WaveWatch3 products for example) as an extra parameter in the SSB correction tables should better model the SSB behavior, with an improved description of the sea state. Commonly 3D models are derived with the direct method, [23].

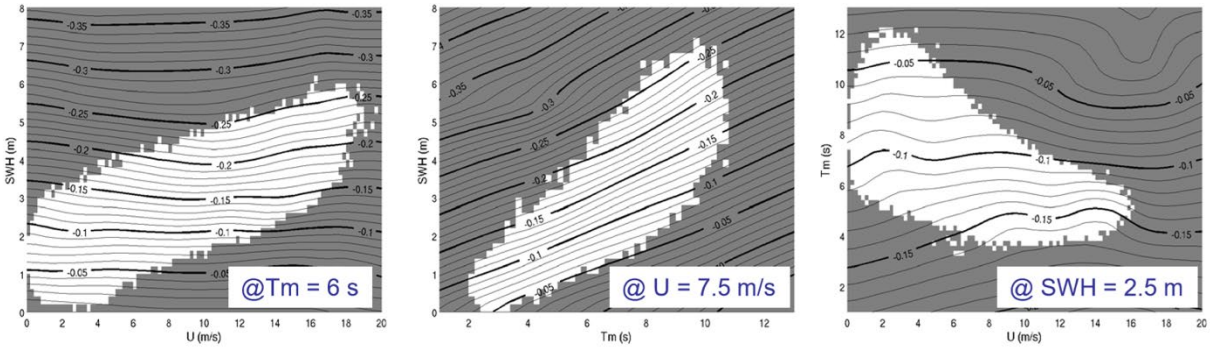

Figure 37 Jason-3 3D SSB model (SWH, U, Tm)